ORNL/TM-2014/288

FY 2014 Status Report: Quantification of CIRFT System Biases and Uncertainties When Testing High-Burnup Spent Nuclear Fuel

Fuel Cycle Research & Development

Prepared for
US Department of Energy
Used Fuel Disposition Campaign
J.-A. Wang and H. Jiang
B. B. Bevard and J. M. Scaglione
Oak Ridge National Laboratory

September 12, 2014
FCRD-UFD-2014-000604

Oak Ridge National Laboratory is a multi-program laboratory managed and operated by UT-Battelle, LLC for the U.S. Department of Energy under contract DE-AC05-00OR22725.

ORNL/TM-2014/288

Materials Science and Technology Division
Oak Ridge National Laboratory

FY 2014 Status Report: Quantification of CIRFT System Biases and Uncertainties When Testing High-Burnup Spent Nuclear Fuel

Jy-An John Wang and Hao Jiang

Program Managers
Bruce Bevard and John Scaglione

Date Published: September 2014

Prepared by
OAK RIDGE NATIONAL LABORATORY
Oak Ridge, Tennessee 37831-6283
managed by
UT-BATTELLE, LLC
for the
U.S. DEPARTMENT OF ENERGY
under contract DE-AC05-00OR22725

This page intentionally left blank.

SUMMARY

The Oak Ridge National Laboratory (ORNL) has developed the cyclic integrated reversible-bending fatigue tester (CIRFT) approach to successfully demonstrate the controllable fatigue fracture on high burnup (HBU) spent nuclear fuel (SNF) in a normal vibration mode. CIRFT enables examination of the underlying mechanisms of SNF system dynamic performance. The major findings of CIRFT on the HBU SNF are as follows:

- SNF system interface bonding plays an important role in SNF vibration performance.
- Fuel structure contributes to SNF system stiffness.
- There are significant variations in stress and curvature of SNF systems during vibration cycles resulting from segment pellets and clad interactions.
- SNF failure initiates at the pellet-pellet interface region and appears to be spontaneous.

Due to the inhomogeneous composite structure of the SNF system, finite element analyses (FEAs) are needed to translate the global moment-curvature measurement into local stress-strain profiles for further investigation. Furthermore, the detailed mechanisms of the pellet-pellet and pellet-clad interactions and the stress concentration effects at the pellet-pellet interface cannot be readily obtained from a CIRFT system measurement. Therefore, detailed FEAs will be necessary to obtain further interpretation of the global test response.

The FEA protocols established for this project provide powerful tools to quantify the CIRFT system biases and the associated uncertainties on the HBU SNF under CIRFT.

The FEA simulation results were validated and benchmarked using data from CIRFT of H. B. Robinson (HBR) fuel rods. This report provides analysis and conclusions concerning the pellet-pellet and pellet-clad interactions of SNF vibration performance, including (1) the distribution of moment-carrying capacity between pellets and clad and (2) the impact of the interface material on the flexural rigidity of the fuel rod system. The immediate consequences of interface debonding are a shift in the load-carrying capacity from the fuel pellets to the clad, as well as a reduction in the composite rod system flexural rigidity. Furthermore, the curvature and associated flexural rigidity estimates based on tests conducted on the CIRFT system are very different from the localized clad data at the pellet-pellet interface region as estimated by FEA, where the local tensile clad curvature is ~3–4 times that of the global curvature at the tension side of the clad. Investigation of the clad local stress also revealed that the neutral axis of the fuel composite system shifts with the interface debonding state. Based on the flexural strain adjusted by accounting for the neutral axis shift, the modified local stress shows good agreement with the local stress-strain obtained from FEA results.

This page intentionally left blank.

CONTENTS

1. INTRODUCTION 1
1.1 Background 1
1.2 Scope of Current Research 1

2. INTERFACE BONDING EFFICIENCY ANALYSIS OF FUEL ROD WITH HBR PELLETS 3
2.1 Good Interface Bonding and No HBR Fuel Rod System Fracture 3
2.1.1 Epoxy Used as Interfacial Material 6
2.1.2 Interfacial Material with 10 × Young's Modulus Material 9
2.2 Debonding at Pellet-Pellet Interfaces and Bonding at Pellet-Clad Interfaces 14
2.2.1 Debonded Pellet-Pellet Interfaces with Empty Gaps 15
2.2.2 Debonded Pellet-Pellet Interfaces without Gaps 23
2.3 Debonded Pellet-Clad and Pellet-Pellet Interfaces 31
2.3.1 Debonded Pellet-Clad Interfaces and Debonded Pellet-Pellet Interfaces with Empty Gaps 31
2.3.2 Debonded Pellet-Clad Interfaces and Debonded Pellet-Pellet Interfaces without Gaps 38
2.4 Clad Curvature Estimation 45
2.4.1 Epoxy Used as Interfacial Material 47
2.4.2 Interfacial Material with a 10 × Young's Modulus 49
2.5 Clad Stress Investigation and Comparison 51
2.5.1 Clad Stress Estimation from Conventional Approach Based on Curvature and Flexural Strain 51
2.5.2 Clad Stress Comparison between Different Interface Bonding Conditions 54

3. CONCLUSION 57

4. REFERENCES 61

This page intentionally left blank.

FIGURES

Figure 1. Geometry of horizontal U-frame bending fatigue testing system with a coplanar rod configuration. 4
Figure 2. Image of 1 inch HBR rod segment from a hot-cell testing sample. 4
Figure 3. FEA model of HBR pellet. 4
Figure 4. Geometry of clad-epoxy-pellet two inch section model with eight HBR pellets. 5
Figure 5. Detail area from Figure 4 for the perfect bond cases. 5
Figure 6. Normal stress distribution and curvature results for clad-epoxy-pellet section model of HBR pellets with perfect bonding using epoxy. 8
Figure 7. Shear stress distribution at the clad for the clad-epoxy-pellet section model of pellets with perfect bonding using epoxy. 9
Figure 8. Normal stress distribution and curvature results for the clad-epoxy-pellet section model of HBR pellets with perfect bonding using a cohesive bonding material with a 10 × Young's modulus material. 10
Figure 9. Shear stress distribution at the clad of the clad-epoxy-pellet section model of HBR pellets with perfect bonding using a cohesive bonding material with a 10 × Young's modulus material. 12
Figure 10. ORNL hot-cell CIRFT data, flexural rigidity, and curvature [3]. 13
Figure 11. Transportation-induced reversal bending stress fields in an SNF system. 15
Figure 12. Detail from Figure 4 for the case of empty gaps at debonded pellet-pellet interfaces. 16
Figure 13. Normal stress distribution and curvature results for the clad-epoxy-pellet section model of HBR pellets with debonded pellet-pellet interfaces with gaps, and bonded pellet-clad interfaces using epoxy. 17
Figure 14. Shear stress distribution at the clad of the clad-epoxy-pellet section model of HBR pellets with debonded pellet-pellet interfaces with gaps and bonded pellet-clad interfaces using epoxy. 19
Figure 15. Normal stress distribution and curvature results for clad-epoxy-pellet section model of HBR pellets with debonded pellet-pellet interfaces with gaps, and bonded pellet-clad interfaces using a 10 × Young's modulus material. 21
Figure 16. Shear stress distribution at the clad of clad-epoxy-pellet section model of HBR pellets with debonded pellet-pellet interfaces with gaps, and bonded pellet-clad interfaces using a 10 × Young's modulus material. 23
Figure 17. Detail from Figure 4 for the case of no gaps at debonded pellet-pellet interfaces. 24
Figure 18. Normal stress distribution and curvature results for clad-epoxy-pellet section model of HBR pellets with debonded pellet-pellet interfaces without gaps, and bonded pellet-clad interfaces using epoxy. 25
Figure 19. Shear stress distribution at the clad of the clad-epoxy-pellet section model of HBR pellets with debonded pellet-pellet interfaces without gaps, and bonded pellet-clad interfaces using epoxy. 27

Figure 20. Normal stress distribution and curvature results for clad-epoxy-pellet section model of HBR pellets with debonded pellet-pellet interfaces without gaps, and bonded pellet-clad interfaces using a 10 × Young's modulus material. 28

Figure 21. Shear stress distribution results at the clad of the clad-epoxy-pellet section model of HBR pellets with debonded pellet-pellet interfaces without gaps, and bonded pellet-clad interfaces using a 10 × Young's modulus material. 30

Figure 22. Detail area from Figure 4 for the cases of empty gaps at debonded pellet-pellet interfaces, and a thin layer filled at the debonded pellet-clad interfaces..... 32

Figure 23. Normal stress distribution and curvature results for clad-epoxy-pellet section model of HBR pellets with empty gaps at debonded pellet-pellet interfaces, and an epoxy layer at debonded pellet-clad interfaces. 33

Figure 24. Shear stress distribution at the clad of the clad-epoxy-pellet section model of HBR pellets with empty gaps at debonded pellet-pellet interfaces, and an epoxy layer at debonded pellet-clad interfaces. 35

Figure 25. Normal stress distribution and curvature results for clad-epoxy-pellet section model of HBR pellets with empty gaps at debonded pellet-pellet interfaces, and a layer with a 10 × Young's modulus material at debonded pellet-clad interfaces. 36

Figure 26. Shear stress distribution at the clad of clad-epoxy-pellet section model of HBR pellets with empty gaps at debonded pellet-pellet interfaces, and a layer of 10 × Young's modulus material at debonded pellet-clad interfaces. 37

Figure 27. Detail area from Figure 4 for the case with no gaps at debonded pellet-pellet interfaces and a thin layer at debonded pellet-clad interfaces. 38

Figure 28. Normal stress distribution and curvature results for the clad-epoxy-pellet section model of HBR pellets without gaps at debonded pellet-pellet interfaces, and with an epoxy layer at debonded pellet-clad interfaces..... 39

Figure 29. Shear stress distribution and curvature results for the clad-epoxy-pellet section model of HBR pellets without gaps at debonded pellet-pellet interfaces, and with an epoxy layer at debonded pellet-clad interfaces. 41

Figure 30. Normal stress distribution and curvature results for the clad-epoxy-pellet section model of HBR pellets without gaps at debonded pellet-pellet interfaces, and with a layer of 10 × Young's modulus material at debonded pellet-clad interfaces. 42

Figure 31. Normal stress distribution and curvature of clad-epoxy-pellet section model of HBR pellets without gaps at debonded pellet-pellet interfaces, and with a layer of 10 × Young's modulus material at debonded pellet-clad interfaces. 44

Figure 32. CIRFT system with horizontal U-frame test setup integrated to Bose dual LM2 TB. 45

Figure 33. Sketch for curvature calculation. 46

Figure 34. Curvature estimations from the deflection data at the tension side of the clad for case using epoxy as the interfacial material. 47

Figure 35. Curvature estimations from the deflection data at the compression side of the clad for the case using epoxy as the interface material. 48

Figure 36. Curvature estimations from the deflection data at the tension side of the clad for the case using the 10 × Young's modulus material. 49

Figure 37. Curvature estimations from the deflection data at the compression side of the clad for the 10 × Young's modulus material. 50
Figure 38. Flexural strain evaluation of a uniform rod. 51
Figure 39. Clad neutral axis at geometric center line for perfect interface bonding. 52
Figure 40. Clad neutral axis shifts from geometric center line for pellet-pellet interface debond and pellet-clad interface bond case. 53

This page intentionally left blank.

TABLES

Table 1. Mechanical properties of the fuel rod 3
Table 2. The curvature, flexural rigidity, and bending moment comparison for the perfect interface bonding simulation 12
Table 3. Comparison of curvature, flexural rigidity, and bending moment for the bonded pellet-clad and debonded pellet-pellet cases 30
Table 4. The curvature, flexural rigidity and bending moment comparison for debonded pellet-clad and pellet-pellet interfaces 44
Table 5. Estimated curvature and flexural rigidity comparison from the tension side of the clad for case using epoxy as the interfacial material 48
Table 6. Estimated curvature and flexural rigidity comparison from the compression side of the clad for the case using epoxy as the interface material 49
Table 7. Estimated curvature and flexural rigidity comparison from the tension side of the clad for the interface material with a 10 × Young's modulus 50
Table 8. Estimated curvature and flexural rigidity comparison from the compression side of the clad for the interface material with a 10 × Young's modulus 51
Table 9. Estimated normal stress compared with FEA stress profile 53
Table 10. Clad normal stress comparison at tension side for different interface bonding conditions 54
Table 11. Clad normal stress comparison at compression side for different interface bonding conditions 55
Table 12. Clad shear stress comparison at tension side for different interface bonding conditions. 55
Table 13. Clad shear stress comparison at compression side for different interface bonding conditions 56
Table 14. The flexural rigidity comparison between the different bonding and debonding cases 59

This page intentionally left blank.

ACRONYMS

CIRFT	cyclic integrated reversible-bending fatigue tester
DOE	Department of Energy
FEA	finite element analysis
HBR	H.B. Robinson
HBU	high burnup
ID	inner diameter
LVDT	linear variable differential transformers
OD	outer diameter
ORNL	Oak Ridge National Laboratory
RD&D	research, development, and deployment
SNF	spent nuclear fuel

This page intentionally left blank.

USED FUEL DISPOSITION CAMPAIGN

FY 2014 STATUS REPORT: QUANTIFICATION OF CIRFT SYSTEM BIASES AND UNCERTAINTIES WHEN TESTING HIGH-BURNUP SPENT NUCLEAR FUEL

1. INTRODUCTION

1.1 Background

The research detailed in this report was conducted to support the Department of Energy (DOE) Used Fuel Disposition Campaign modeling, simulation, and experimental integration research, development, and deployment (RD&D) plan for spent nuclear fuel (SNF) integrity and structural performance under normal conditions of transportation [1].

The Oak Ridge National Laboratory (ORNL) has developed the cyclic integrated reversible-bending fatigue tester (CIRFT) approach to successfully demonstrate the controllable fatigue fracture on high burnup (HBU) SNF in a normal vibration mode. CIRFT enables examination of the underlying mechanisms of SNF system dynamic performance. The major findings of CIRFT on the HBU SNF are as follows:

- SNF system interface bonding plays an important role in SNF vibration performance.
- Fuel structure contributes to the SNF system stiffness.
- There are significant variations in stress and curvature of SNF systems during vibration cycles resulting from segment pellets and clad interaction.
- SNF failure initiates at the pellet-pellet interface region and appears to be spontaneous.

Due to the inhomogeneous composite structure of the SNF system, finite element analyses (FEA) are needed to translate the global moment-curvature measurement into local stress-strain profiles for further investigation. Furthermore, the detailed mechanisms of the pellet-pellet and pellet-clad interactions and the stress concentration effects at the pellet-pellet interface cannot be readily obtained from a CIRFT system measurement. Therefore, detailed FEA will be necessary to obtain further interpretation of the global test response.

The FEA protocols developed for this project provide powerful tools to quantify the CIRFT system biases and the associated uncertainties on the HBU SNF under CIRFT.

This project report also provides the FEA methodology used to evaluate the effects of pellet-pellet and pellet-clad interactions. The methodology is a road map for further protocol development with respect to the effective lifetime prediction of the SNF system under normal transportation vibration.

This study provides detailed explanations of the effects of pellet-pellet and pellet-clad interactions—including pellet fracture and pellet-clad bonding efficiency—on the clad performance reliability. The FEA simulation results were also calibrated and benchmarked with fatigue aging data [2] obtained from ORNL reversal bending fatigue testing.

1.2 Scope of Current Research

The objective of this research is to use the FEA protocols to translate the global response of CIRFT examination to the local stress-strain level and to quantify the CIRFT system biases and associated

uncertainties on the HBU SNF under CIRFT.

The FEA simulation results were validated and calibrated by ORNL reversal bending fatigue testing of the HBR fuel rod.

The FEA models were developed using ABAQUS. They consist of a two inch gauge section covering the Zr-4 clad and HBR pellets and interfacial layers that provide chemical cohesive bonding or mechanical radial compressive residual stresses from pellet-clad contact pressure. To estimate fuel rod system responses, including the stress profile and the associated curvature κ, bending moments (*M*) were applied to both ends of the fuel rod. Based on the FEA results, the flexural rigidity (*EI*) of the simulation cases was estimated as EI = M/κ. The detailed discussion of the simulation cases is divided into three sections:

- a section model with good interface bonding and without pellet fracture,
- a section model with good bonding at pellet-clad interfaces and debonding at pellet-pellet interfaces, and
- a section model with debonding at both pellet-clad and pellet-pellet interfaces.

Each section includes a comparison and discussion of the simulation results for (1) an interfacial material using epoxy and (2) an interfacial material with a Young's modulus 10 times that of epoxy (abbreviated hereinafter as "10 × Young's modulus material"). The curvature of a fuel rod system estimated from global and local deflection data for the clad was studied in detail based on the tension and the compression sides of the clad. The fuel composite system neutral axis shift was investigated. Based on the estimated curvature and flexural strain adjusted with the neutral axis shift, the normal stress has been estimated and compared with FEA results for nonuniform distributed stresses. FEA results for normal stress and shear stress for different interface bonding conditions also are compared and discussed.

2. INTERFACE BONDING EFFICIENCY ANALYSIS OF FUEL ROD WITH HBR PELLETS

Following the method described in Refs. 2, 3, and 4, ABAQUS was used for a structural analysis and interfacial bonding evaluation of fuel rods with HBR pellets. The rods were tested in a hot-cell environment in the CIRFT developed by ORNL [5–7]. To validate the simulation results, the same fuel rod materials were used in the hot-cell tests and the FEA. The HBR pellet material was UO_2, and the clad material was Zr-4. An epoxy was used as an interface bonding material to simulate fused areas. Table 1 lists the material properties of the fuel rod.

Table 1. Mechanical properties of the fuel rod

Material	Young's modulus (psi)	Poisson's ratio	Yield strength (psi)	Density (lb/in^3)
UO_2[a]	2.92e7	0.32	3.11e5	0.396
Zircaloy-4[a]	1.32e7	0.33	1.31e5	0.237
Epoxy[a]	5.07e5	0.37	10007.6	0.0452

[a] Ref. [7]

2.1 Good Interface Bonding and No HBR Fuel Rod System Fracture

Figure 1 shows the geometry of a U-frame bending fatigue testing system with a coplanar configuration for the fuel rod. The two inch gauge section is highlighted in black. A finite element model was established to represent the two inch gauge section of the test specimen. The model is referred to as the "clad-epoxy-pellet section model."

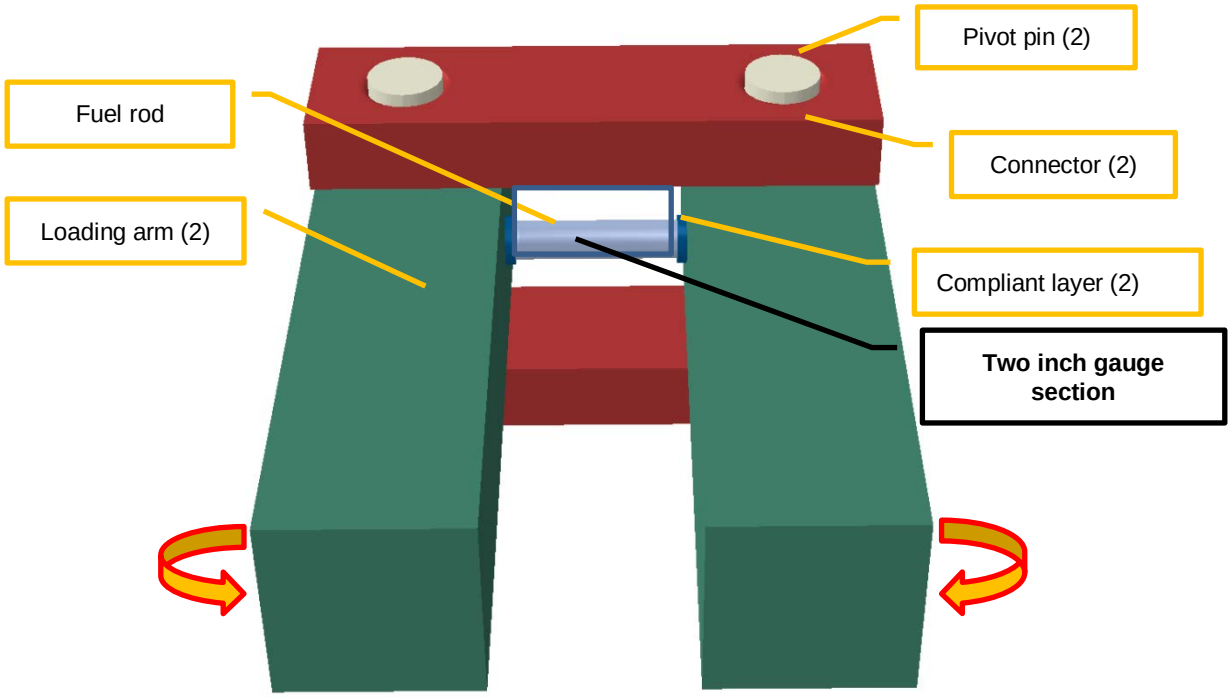

Figure 1. Geometry of horizontal U-frame bending fatigue testing system with a coplanar rod configuration.

Figure 2 shows a one inch HBR rod segment from a hot-cell testing sample. The measured outer diameter (OD) of the clad is 0.425 in. The cladding thickness is 0.031in., so the inner diameter (ID) is 0.364 in. Figure 2 gives a clear view of the HBR pellets. The pellet length is 0.273 in., much less than the 0.6 in. length of the surrogate rod in a previous report [3]. The pellet ends dish in to reduce pellet surface clinging (Figure 2). The pellet OD is 0.354 in. An HBR pellet was modeled by FEA to represent the real

testing sample (Figure 3). Both ends of the pellet were constructed with a dip diameter of 0.25 in. and a depth of 0.0006 in. so that the end surfaces would not touch at the dished-in area.

Figure 2. Image of one inch HBR rod segment from a hot-cell testing sample.

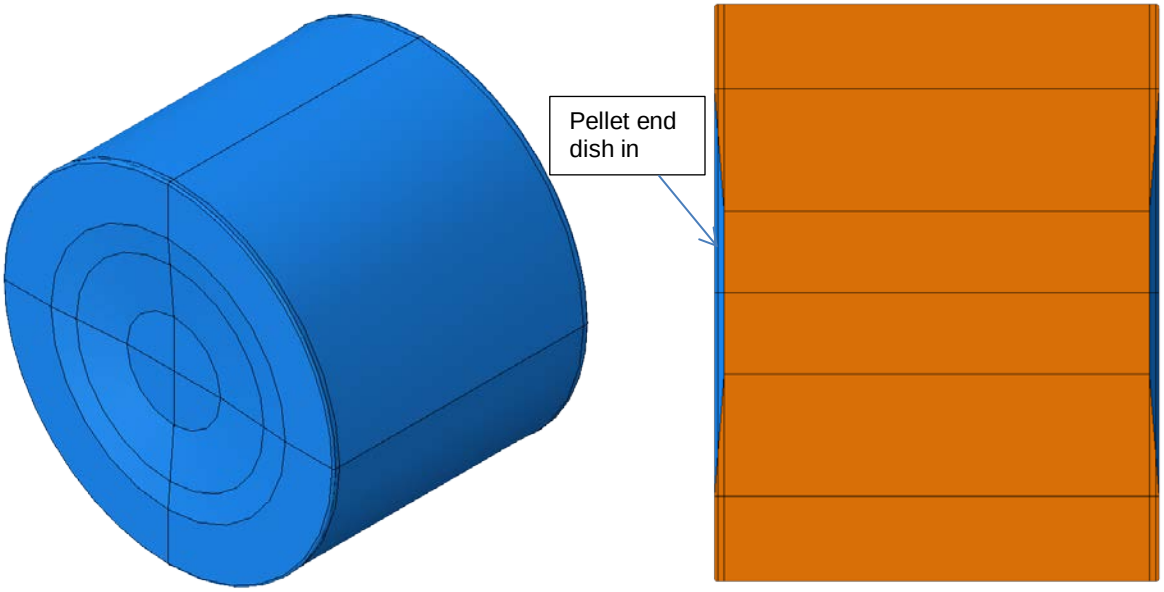

Figure 3. FEA model of HBR pellet.

Figure 4 illustrates the clad-epoxy-pellet section model with HBR pellets. In the two inch gauge section, six full-length and two partial-length pellets were modeled. The epoxy is 0.005 in. thick. To simulate "good interface bonding" at the pellet-pellet interface and an unfractured rod system, the pellet-pellet and pellet-clad interfaces were all tied. Bending moments were applied on both ends of the fuel rod rotating along the *X* axis as shown in Figure 4 (b). To validate the FEA simulation with the hot-cell testing data, the bending moment *Mx* was the same as that used in the tests—6.25 N·m. Both loading surfaces of the HBR fuel rod were constrained with rotation along the *Y* and *Z* axes and translation along the *X* direction. In the following finite element models, the global mesh is 0.02 in., and some local meshes are as small as 0.0025 in. The quasistatic procedure is used in the FEA from ABAQUS.

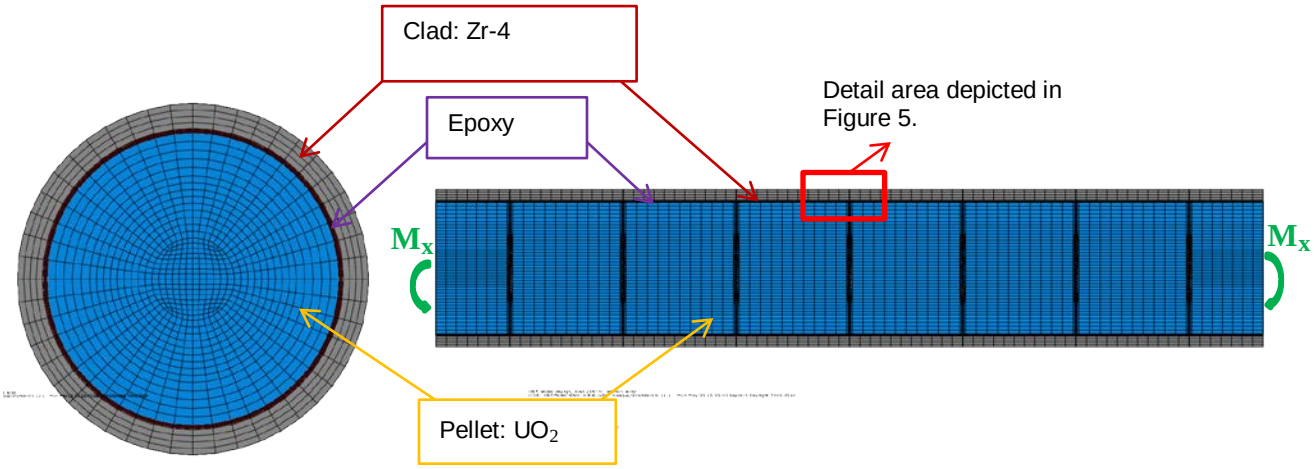

(a) Cross section view (b) Longitudinal section view

Figure 4. Geometry of clad-epoxy-pellet two inch section model with eight HBR pellets.

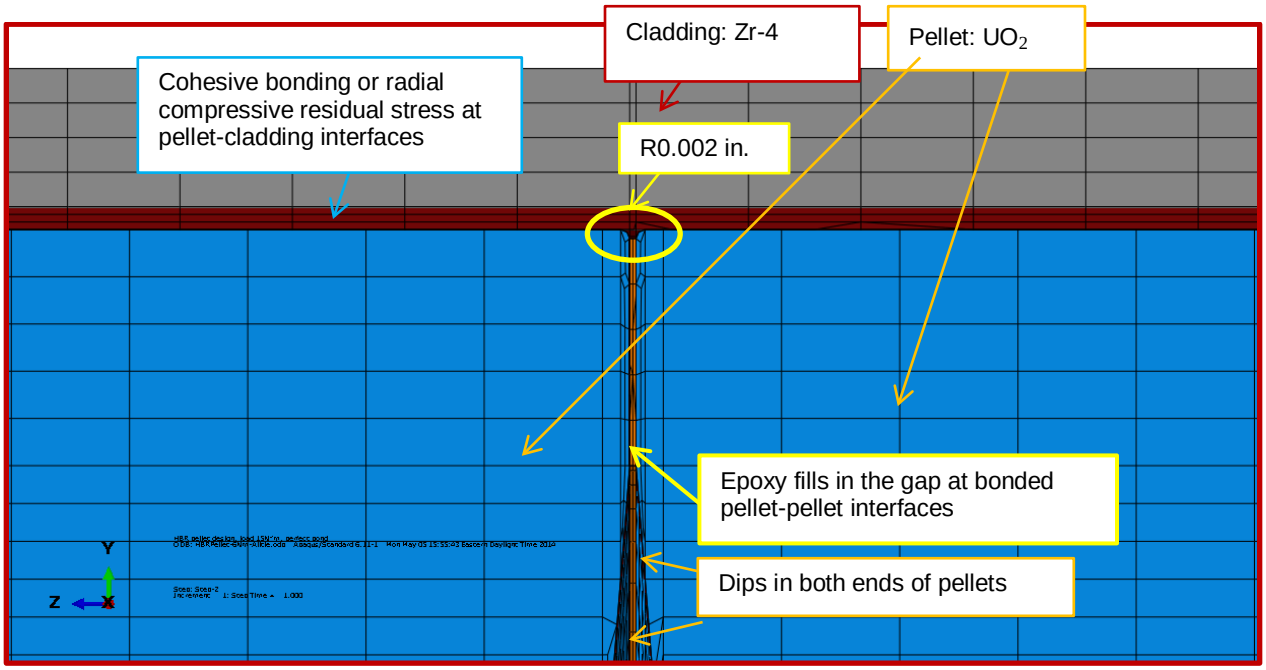

Figure 5. Detail area from Figure 4 for the perfect bond cases.

Figure 5 shows the configuration of the detail area from Figure 4. The pellets were modeled with rounding of 0.002 in. on the end surfaces, and the end surfaces were dished at both ends to avoid pellet clinging. The dished areas of the pellet end surfaces do not come into contact during bending.

2.1.1 Epoxy Used as Interfacial Material

Thin epoxy layers are tied to the surfaces of the pellet-clad interfaces and the pellet-pellet interfaces to simulate cohesive bonding or radial compressive residual stress. The epoxy layers at the pellet-pellet interfaces in the model are 0.0014 inch thick.

The resulting normal stress distribution and the curvature under the bending moment 6.25 N·m are shown in Figure 6. The resultant curvature is 0.082 m^{-1}, which is too small to be noticeable. Based on the stress distribution shown in Figure 6 (a), the maximum stress occurs at the pellets, which indicates that the perfectly bonded HBR pellets carry a larger portion of the moment resistance than the clad. From the detail view shown in Figure 6 (b), the maximum stress is observed at the pellet-pellet interface tie area. The perfect bond assigned at the interface tie area is carrying most of the bending moment resistance. The stress in the clad is under the yield point of 131 ksi. Therefore, the clad has not yielded under the 6.25N·m bending moment, nor has the HBR pellet, which has a much higher yield strength than the clad. This indicates that the HBR fuel rod with a perfect bonding condition will remain within the linear elastic range under the target loading. The resultant σ_{zz} at the pellet-pellet interface in Figure 6 (c) shows the maximum stress concentrated on the limited tie areas. This occurs because the dips in the ends of the pellets cause the contact surfaces to be confined to a limited area.

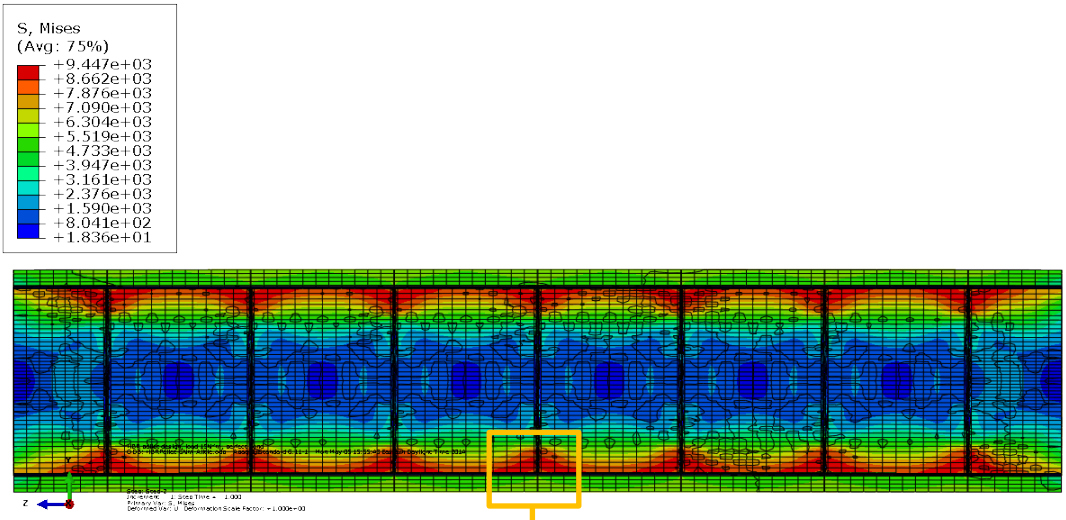

(a) Longitudinal section view of curvature and von Mises stress

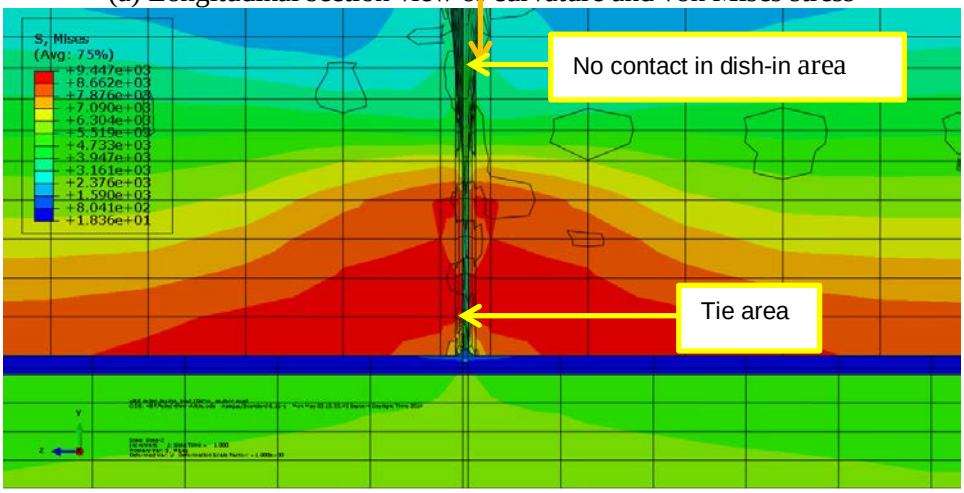

(b) Detail area view

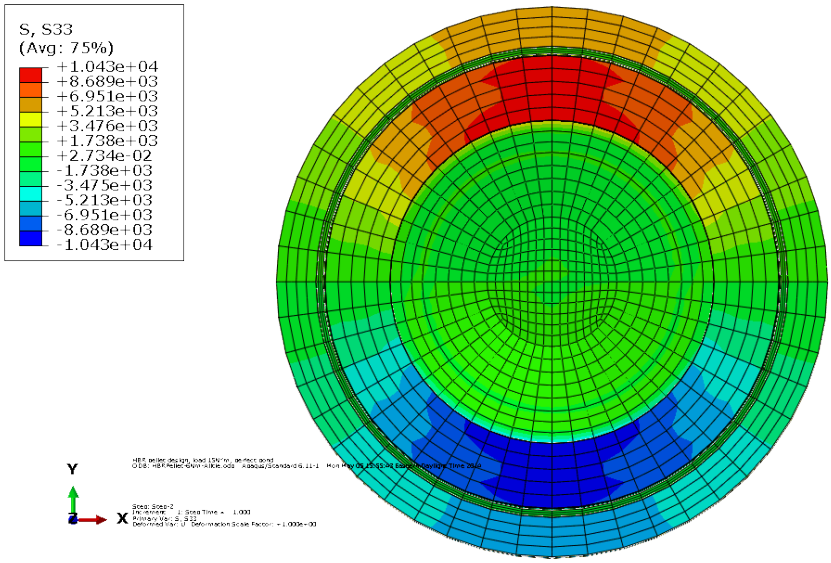

(c) Cross section view of σ_{zz} at a pellet-pellet interface

Figure 6. Normal stress distribution and curvature results for clad-epoxy-pellet section model of HBR pellets with perfect bonding using epoxy.

Figure 7 shows the shear stress distribution under the bending moment of 6.25 N·m at the cladding. Shear stresses at the cladding are minimal. As a result of the perfect bonding, the pellets and the cladding work as a whole. There is no shear stress concentration inside the gauge section. The stress concentration occurs at the boundary as a result of composite material mismatch under flexural deformation.

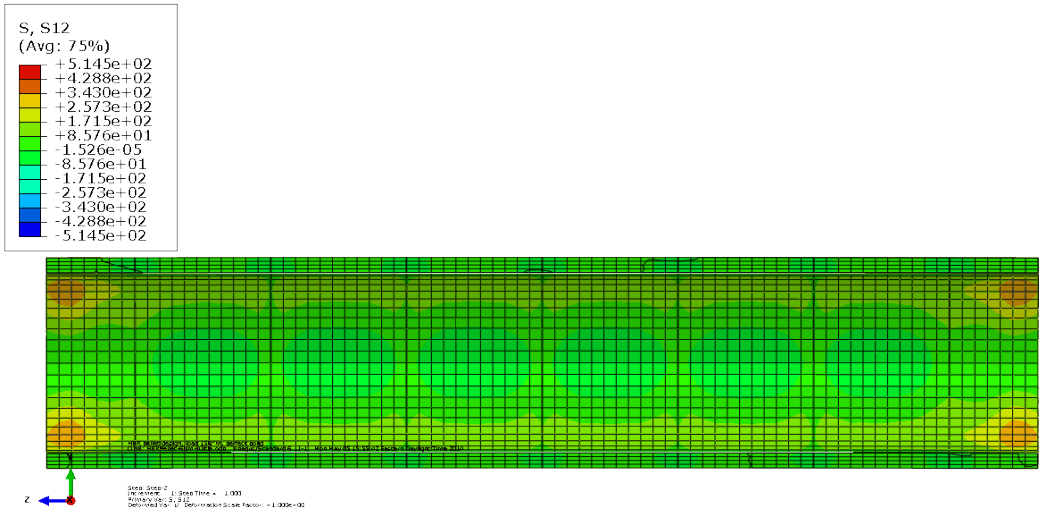

(a) Shear stress σ_{xy}

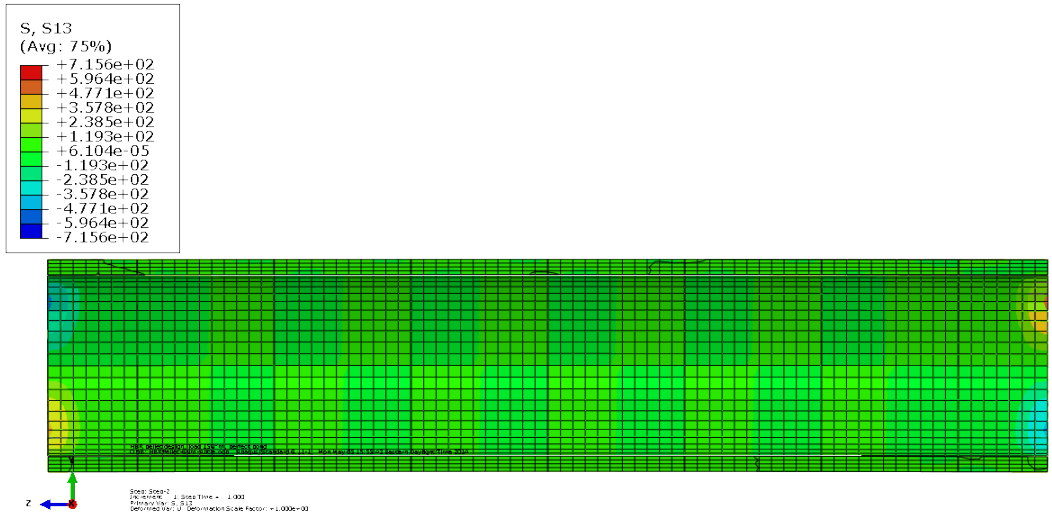

(b) Shear stress σ_{xz}

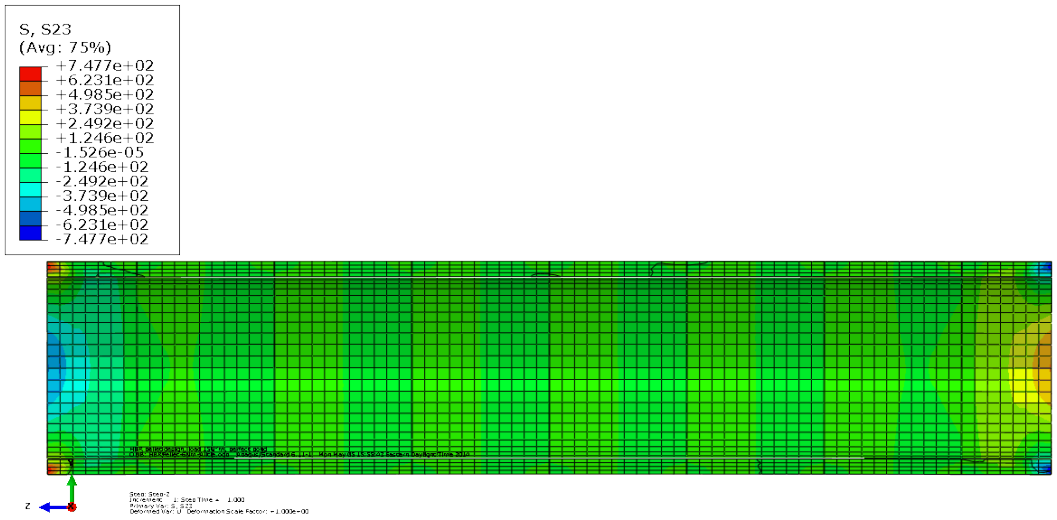

(c) Shear stress σ_{yz}

Figure 7. Shear stress distribution at the clad for the clad-epoxy-pellet section model of pellets with perfect bonding using epoxy.

2.1.2 Interfacial Material with 10 × Young's Modulus Material

To investigate the impact of the cohesive bonding material, the Young's modulus of the bonding material was set at an exaggerated level of 10 times the Young's modulus of the epoxy with the material properties shown in Table 1. The second simulation used the same clad-epoxy-pellet section model shown in Figure 4 and Figure 5. Except for the epoxy, all the materials were the same as those used in the previous simulation. The bonding, loading, and boundary conditions were exactly the same as those applied in the first simulation.

Based on the stress distribution seen in Figure 8, the change in the Young's modulus of the cohesive bonding layer does not change the stress distribution. The maximum stress still occurs at the pellet where pellets tie to each other at the pellet-pellet interfaces. The clad and pellets are all under yield stress. However, the maximum stress in this simulation case is higher than that in the first simulation case for the normal epoxy layer, which means that pellets take over more of the bending moment because of stiffer cohesive bonding. The induced curvature is 0.072 m^{-1}, a 12% decrease over that in the first case.

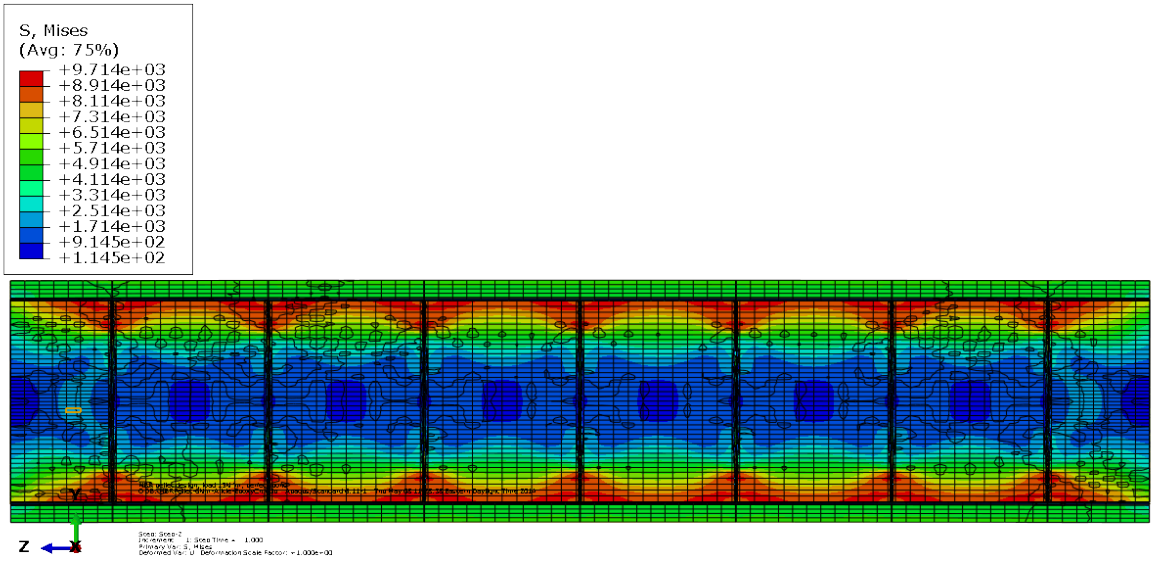

(a) Longitudinal section view of resultant curvature and von Mises stress

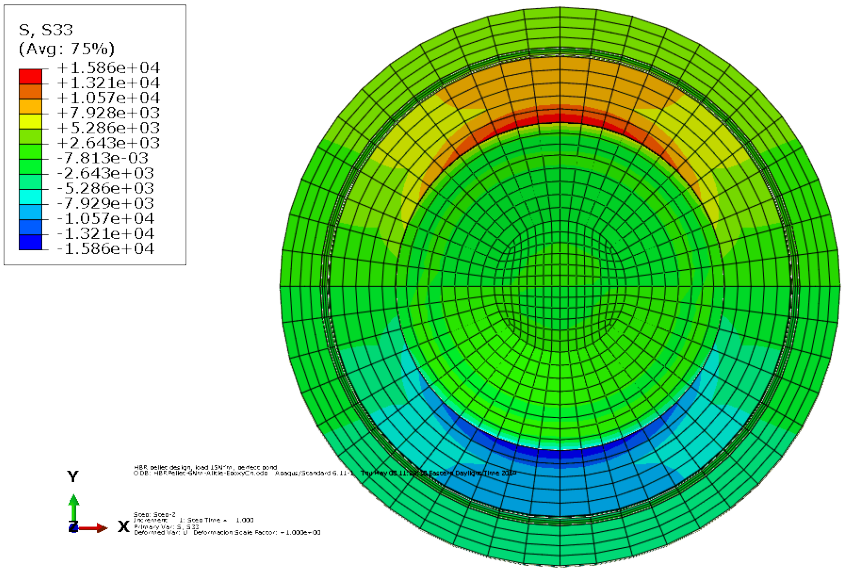

(b) Cross section view of resultant σ_{zz} at a pellet-pellet interface

Figure 8. Normal stress distribution and curvature results for the clad-epoxy-pellet section model of HBR pellets with perfect bonding using a cohesive bonding material with a 10 × Young's modulus material.

The shear stress distribution in Figure 9 is similar to that in the first case. No shear stress concentration occurs inside the cladding. Shear stresses are small. The change in cohesive bonding material has minimal impact on the shear stress.

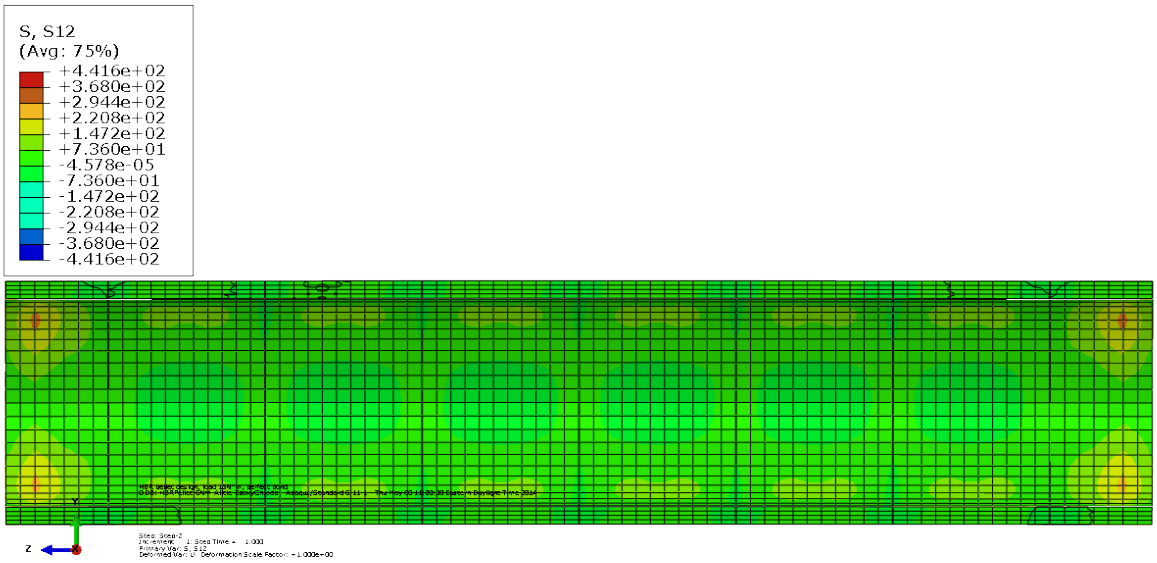

(a) Shear stress σ_{xy}

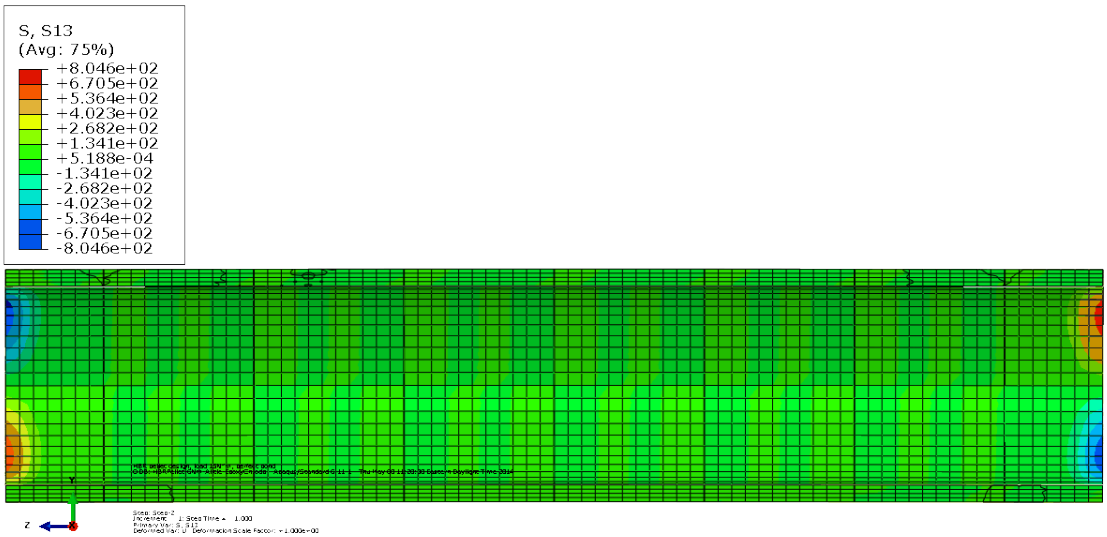

(b) Shear stress σ_{xz}

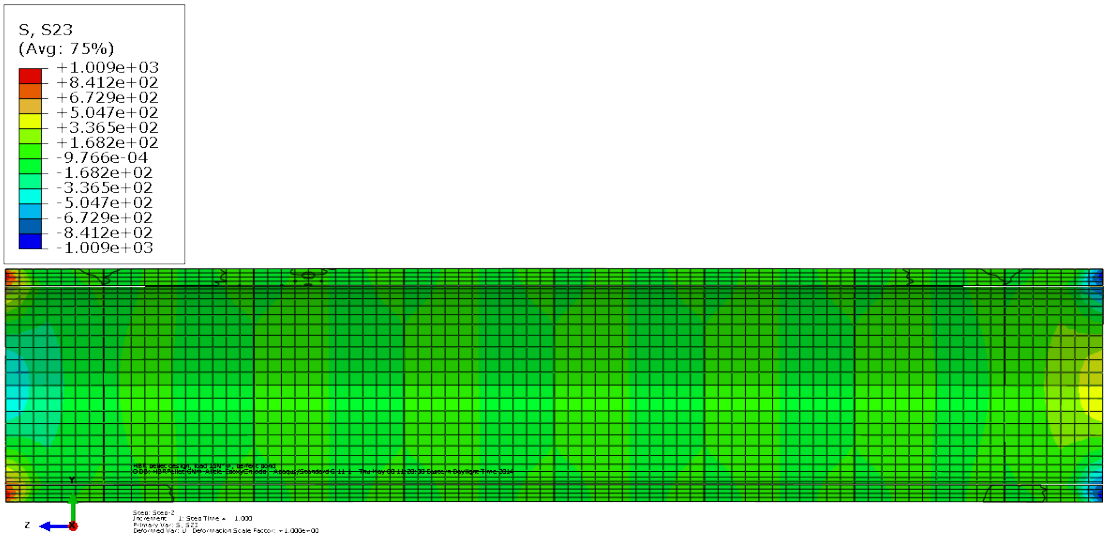

(c) Shear stress σ_{yz}

Figure 9. Shear stress distribution at the clad of the clad-epoxy-pellet section model of HBR pellets with perfect bonding using a cohesive bonding material with a 10 × Young's modulus material.

In this section, two simulation cases for the HBR fuel rod—one with good interface bonding and one without inserted rod fracture—were studied. To simulate good cohesive bonding in the FEA, the pellet--clad interfaces were tied together with a thin epoxy layer, while the Young's modulus of the cohesive bonding material was changed for purposes of the study.

The curvature and flexure rigidity for those cases are summarized in Table 2. A load control procedure was used. The bending moment M was applied to both ends of the fuel rod, and the bending curvature κ was estimated from the FEA results within the gauge section. The flexural rigidity EI (the product of the Young's modulus E and the moment of inertia I) of a fuel rod can be estimated using the applied moment M and the resultant curvature κ, as described in Eq. (1).

$$EI = M/\kappa \tag{1}$$

Based on the resulting σ_{zz}, shown in Figure 6 (c) and Figure 8 (b), the bending moment was calculated for the cladding and pellets, respectively. The total resultant bending moment should be equal to the bending load M_x, 6.25 N·m. Estimated bending moments for the cladding and pellets are also summarized to directly compare the load carrying capacity of the different system components.

Table 2. The curvature, flexural rigidity, and bending moment comparison for the perfect interface bonding simulation

	Curvature κ(1/m)	Flexural rigidity EI (N·m^2)	Clad bending moment M (N·m)	Pellet bending moment M (N·m)
Perfect bond with epoxy	0.082	77	2.45	3.8
Perfect bond with 10 × Young's modulus material	0.072	87	2.06	4.19

Table 2 shows that the flexure rigidity for a perfect bonding condition with epoxy as the cohesive bonding material is 77 N·m^2 for the HBR pellet fuel rod. The flexure rigidity increases by 11.5% to 87 N·m^2 as the Young's modulus of the bonding material increases by 10 times. This is a direct result of the fuel rod becoming stiffer. Based on the load-carrying capacity, the perfectly bonded pellets take over more of the bending moment than the cladding for both cases. As the cohesive bonding becomes stiffer, the clad carries less of the bending load.

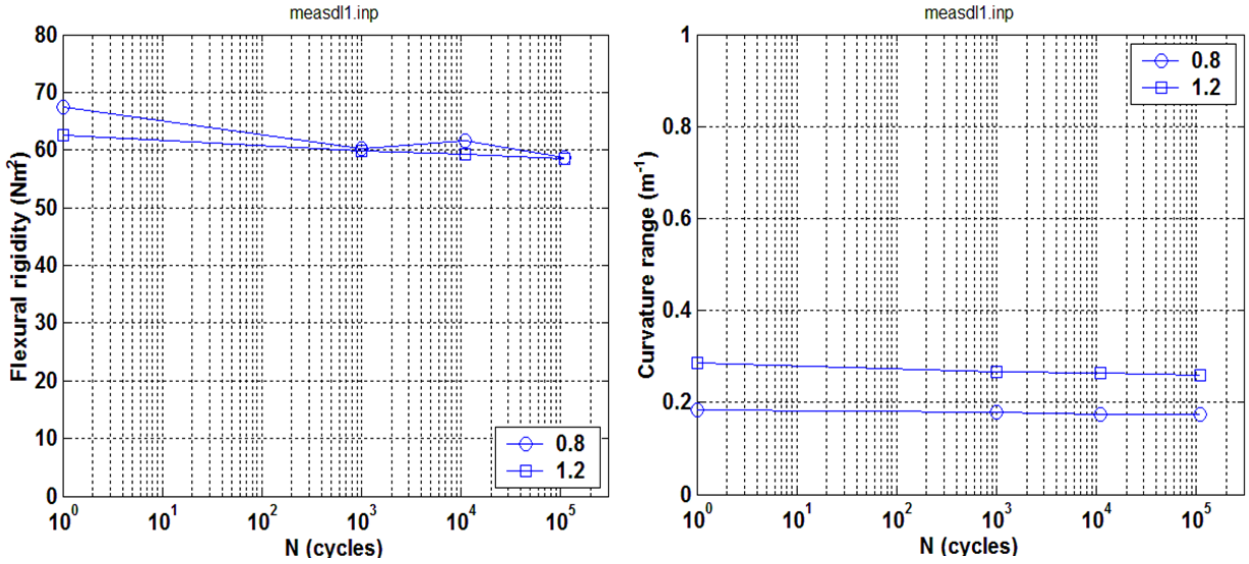

Figure 10. ORNL hot-cell CIRFT data, flexural rigidity, and curvature [3].

The condition of the ORNL HBR fuel rod hot-cell testing specimens resembles that of the clad-epoxy-pellet section model with epoxy-filled gaps at the pellet-pellet interfaces. The HBR fuel specimen was tested under a 6.25 N·m bending moment. Figure 10 shows ORNL hot-cell CIRFT data. The flexural rigidity based on the hot-cell test data was observed to be between 60 and 70 N·m^2, and the curvature was around 0.09 m^{-1}. The initial (first cycle) test data usually have the highest flexural rigidity since the pellet-clad and pellet-pellet interface bonds should maintain the best status before bending fatigue damage. The flexural rigidity in the first test data was a little lower than the FEA estimate, which indicates this testing sample probably has interfacial debonding rather than perfect bonding at the initial test stage.

With good interface bonding and without fuel rod fracture, the fuel rod can carry most of the bending moment under normal transportation vibration. This is a result of the higher Young's modulus of the fuel pellet compared with the clad, along with a much higher yield stress, as shown in Table 1. ORNL fuel data validate that inserted pellets can carry more moment resistance than the clad because of their higher stiffness if the pellet-clad and pellet-pellet interface bonds remain intact. Because of the high flexural strength of the HBR pellets, the fuel rod responds to the bending moment within the linear elastic range. The high flexural rigidity estimated from FEA agrees well with that estimated from bending fatigue testing data. Furthermore, under cyclic loading, it is expected that the interface bond will be progressively degraded as is demonstrated in Figure 10, with decreasing flexural rigidity under increased loading cycles.

2.2 Debonding at Pellet-Pellet Interfaces and Bonding at Pellet-Clad Interfaces

Before high-burnup SNF is transported, there are inherited stress fields in the SNF system. For example, there may be axial tensile stress and tangential tensile stress due to pellet-clad mechanical interaction or oxide volume expansion, radial compressive stress due to hydride compaction, and tangential shear stress due to hydride volume expansion. Vibration during transportation will induce reversal bending in an SNF assembly. Repeated expansion and contraction in both the axial and tangential directions of the SNF rod due to reversal bending flexural deformation, combined with stress concentration, can degrade the interface bonding at the fuel pellet-clad and pellet-pellet interfaces (Figure 11). Although the shear stress is small relative to the normal stress due to bending, that does not mean that it can be neglected. In composite rods or SNF rods in particular, excessive shear due to material mismatch can be a cause of interfacial bonding failure.

At pellet-pellet interfaces, interfacial bonding failure is caused mostly by normal stress due to reversal bending flexural deformation combined with relatively smaller shear stress (see Figure 11). At pellet-clad interfaces, localized high shear stress will also arise to compensate for the material mismatch under flexural deformation. As mentioned earlier, the shear stress is small relative to the normal stress; therefore, it is likely that interfacial bonding failure at pellet-pellet interfaces will begin before debonding occurs at pellet-clad interfaces. In addition, the HBR pellets have dished noncontact areas at both end surfaces, so the bonding area at the pellet-pellet interface is limited to a relatively small area, making it easier for the pellet-pellet interfaces to debond. Observations of an ORNL reversal bending fatigue surrogate stainless steel rod with alumina pellets verified this hypothesis. In this section, the clad-epoxy-pellet section model with eight pellets was used to investigate the HBR fuel rod bending response with perfect bonding at pellet-clad interfaces and debonding at pellet-pellet interfaces. The material properties, geometry, and loading and boundary conditions were the same as those used in the previous FEA simulation.

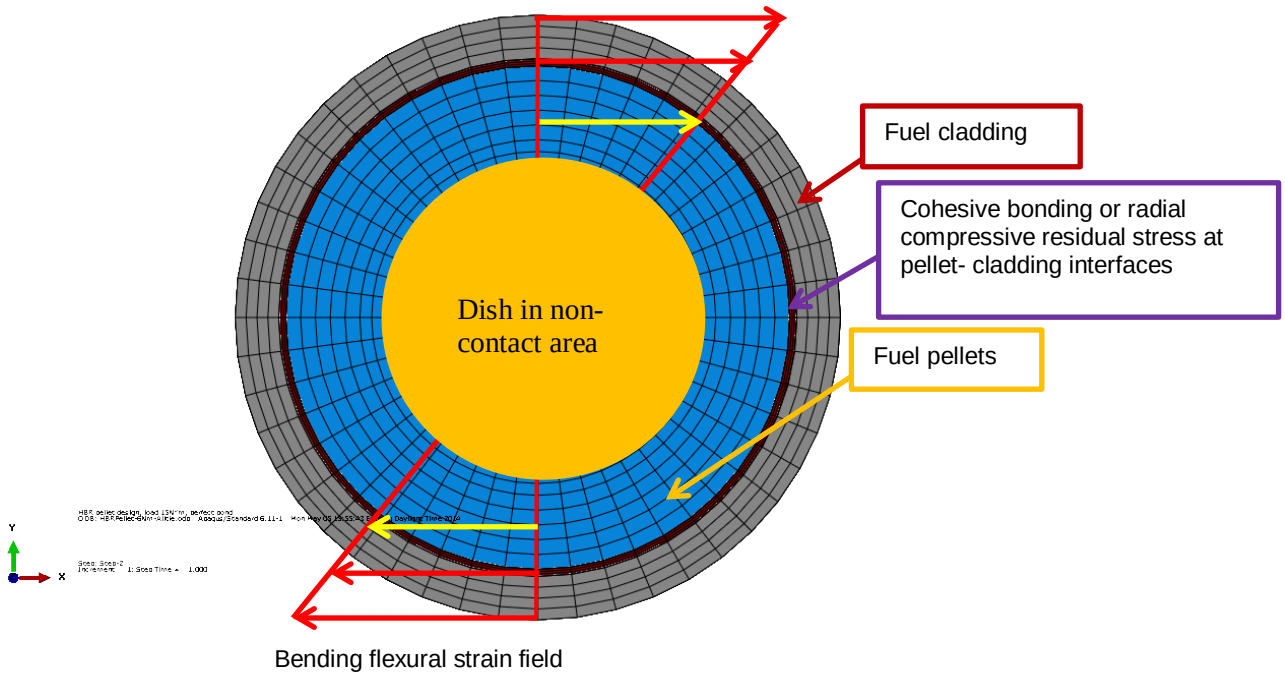

(a)

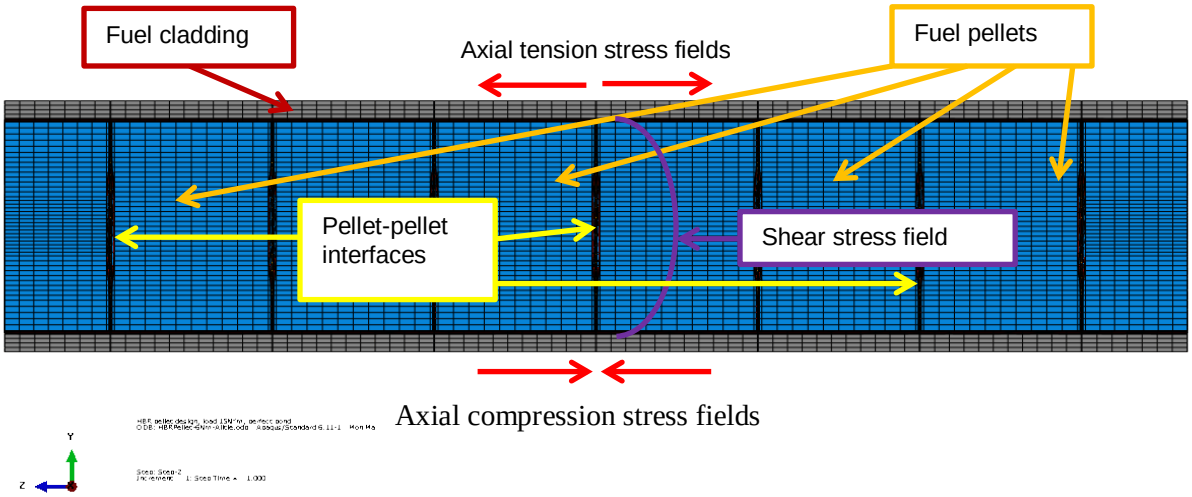

(b)

Figure 11. Transportation-induced reversal bending stress fields in an SNF system.

2.2.1 Debonded Pellet-Pellet Interfaces with Empty Gaps

To simulate a good cohesive bond condition or radial compressive residual stress at pellet-clad interfaces, a thin bonding layer was tied to the surfaces at the pellet-clad interfaces. In this section, the case study was designed to simulate the response with a debonded pellet-pellet interface. There are empty gaps at the pellet-pellet interfaces (Figure 12). During bending flexural deformation, the pellets overcome the gaps and then contact one another at the interfaces. The pellets have dips and end surfaces with a rounding of 0.002 in.

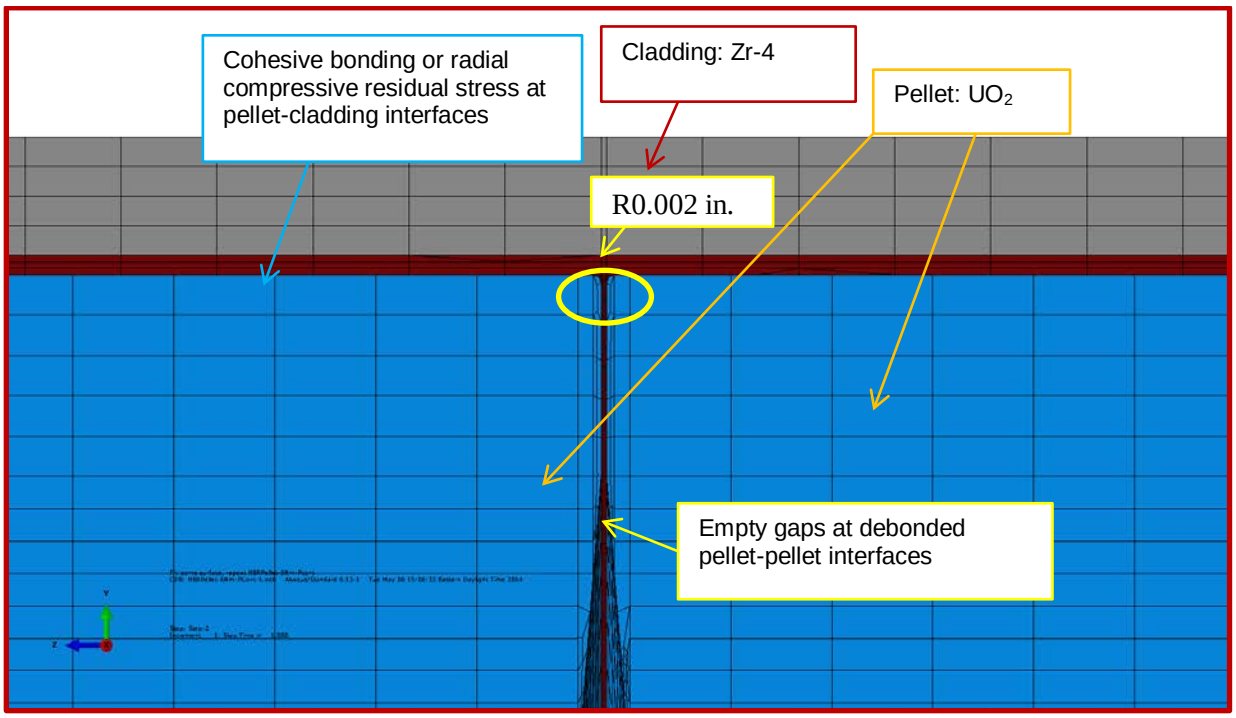

Figure 12. Detail from Figure 4 for the case of empty gaps at debonded pellet-pellet interfaces.

2.2.1.1 Epoxy Used as Interfacial Material

Similar to the perfect bonding case, the first simulation case for pellet-pellet interface debonding with gaps has an epoxy layer tied to the surfaces at the pellet-clad interfaces with the original Young's modulus, as shown in Table 1, to simulate good cohesive bonding at pellet-clad interfaces.

The normal stress and curvature responding to the bending moment are illustrated in Figure 13. Compared with the results shown in Figure 6, there are significant differences in the stress distribution between the pellet-pellet interface bonding case and the pellet-pellet interface debonding case; the pellet-clad interface remains perfectly bonded in both cases. For instance, at the pellet-pellet interface in the debonding case, the maximum stress occurs at the clad and is located at the top and bottom portions of the pellet-pellet interface regions. As a result of the small bending moment, the maximum stress at the clad is 10 times lower than the yield strength of Zr-4, as shown in Table 1, so the Zr-4 clad does not yield. In most of the clad, the stress is much lower than the maximum because the perfect pellet-clad bonding provides good support to the clad. Since there are gaps between pellet-pellet interfaces, the clad deforms continuously until the gaps are reduced by direct contact of the pellet-pellet surfaces. However, no stress concentration is observed at the pellet-pellet contact corners. The resulting σ_{zz} clearly indicates that the clad takes over more of the bending moment resistance than the pellets at the debonded pellet-pellet interfaces.

At the debonded pellet-pellet interfaces, the pellets can transfer load only via hard contact, so the load-carrying capacity shifts significantly from the pellets to the clad. When the Zr-4 clad starts to carry most of the bending moment at the pellet-pellet interface region, the result is maximum stress concentration at the Zr-4 clad. However, in most of the gauge section, the pellets still provide sufficient internal support to the clad because of good cohesive bonding at the pellet-clad interfaces, and they will carry most of the bending load. Therefore, there is much lower stress in most regions of the Zr-4 clad.

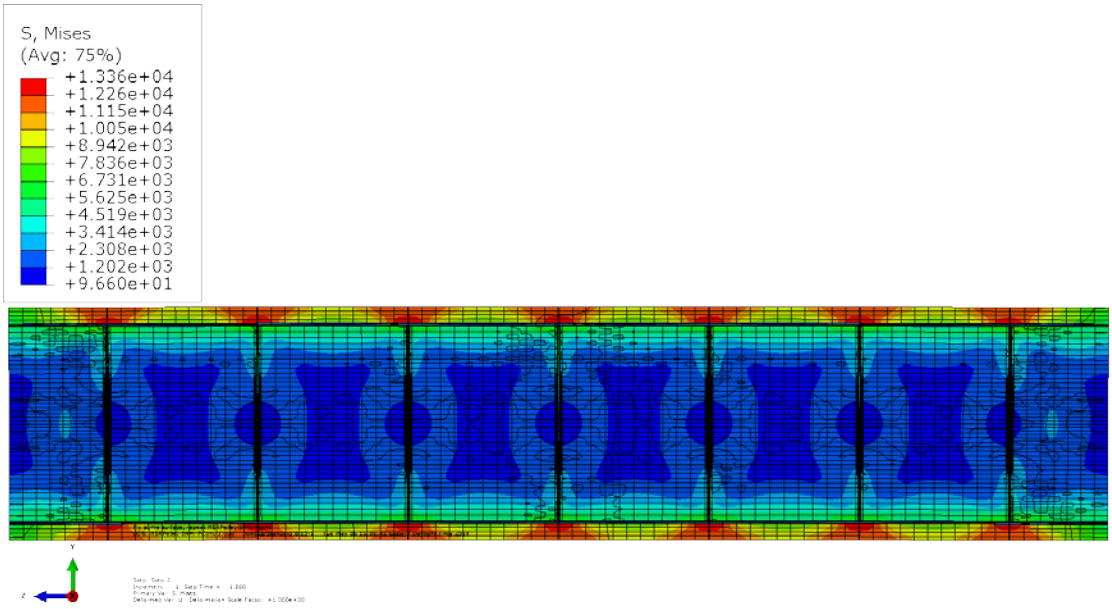

(a) Longitudinal section view of resultant curvature and von Mises stress

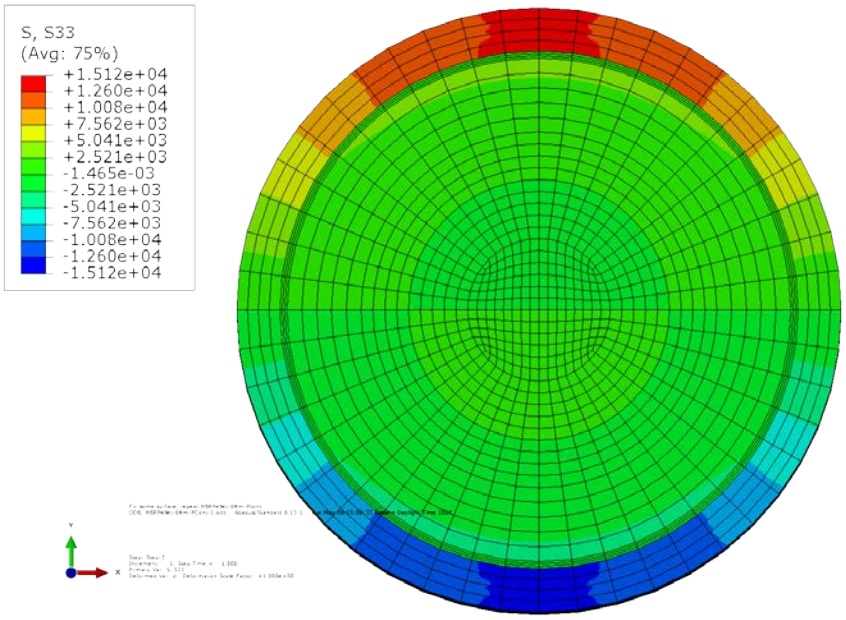

(b) Cross section view of resultant σ_{zz} at a pellet-pellet interface

Figure 13. Normal stress distribution and curvature results for the clad-epoxy-pellet section model of HBR pellets with debonded pellet-pellet interfaces with gaps, and bonded pellet-clad interfaces using epoxy.

In Figure 6, the results of the perfect bond case show that the pellets carry significant bending moment resistance; the maximum stress resides on the pellets, and there is no yielding at either the pellets or the clad. It is also interesting to note that the von Mises stress distribution in debonded pellets appears to be

quite different from the results of the bonded pellet-pellet interface case. For example, in Figure 6, a dog-bone shape appears in a horizontal direction inside an HBR pellet as a result of von Mises stress distribution. However, in Figure 13, the dog-bone shape inside an HBR pellet is vertically oriented. The third discrepancy lies in the induced curvature. In the debonding case, the curvature is 0.16 m^{-1}, double that of the perfect bond case shown in Figure 6.

In Figure 14, the difference from the results in Figure 7 for the perfect bond case is apparent. With the pellet-pellet interfaces debonded, the shear stresses surge near the pellet-pellet interface debonding region inside the cladding. The reason might be an increase in shear stress due to a composite material mismatch at the debonded pellet-pellet interface boundary under bending flexural deformation. With good cohesive bonding at pellet-clad interfaces, the clad transfers some shear load at the debonding region. If there are small gaps at the pellet-pellet interfaces, the shear stress concentration occurs at both the top tension and bottom compression regions of the clad. Maximum stress levels are higher than in perfect bond cases; however, the shear stresses are still one order of magnitude lower than the normal stress in the same simulation case.

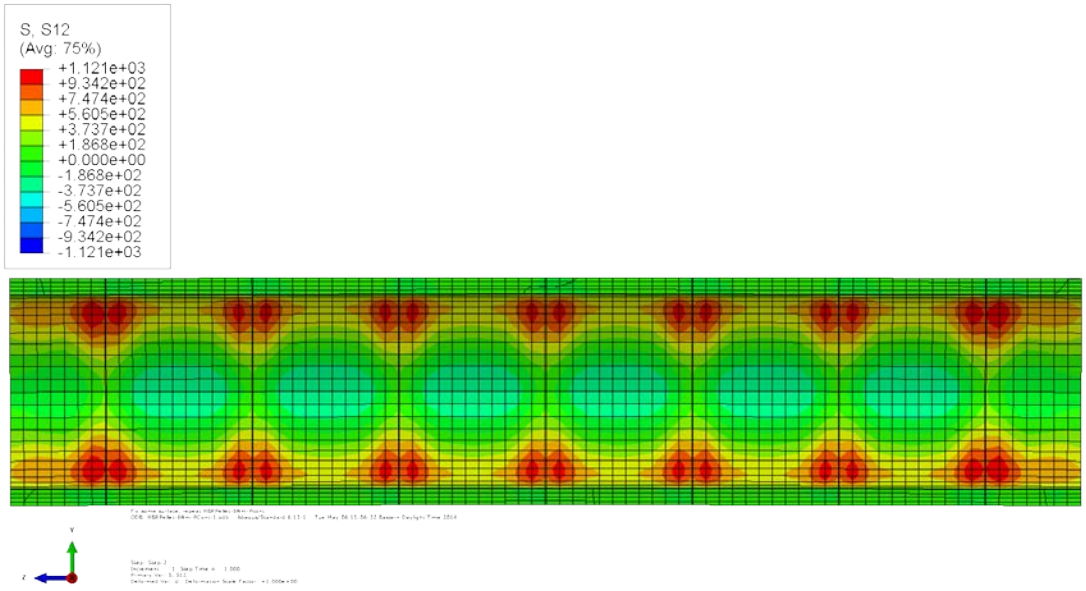

(a) Shear stress σ_{xy}

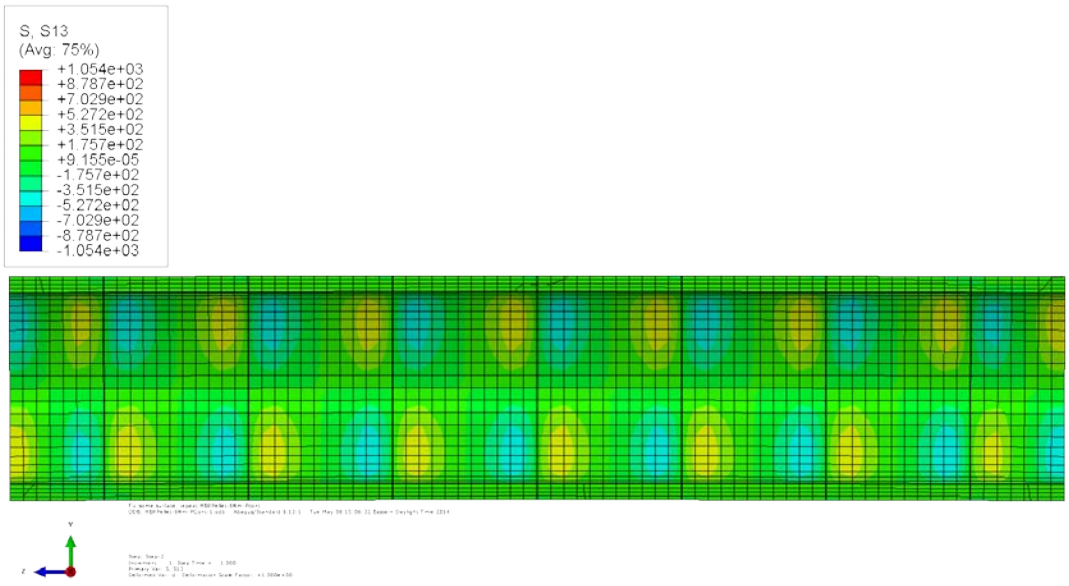

(b) Shear stress σ_{xz}

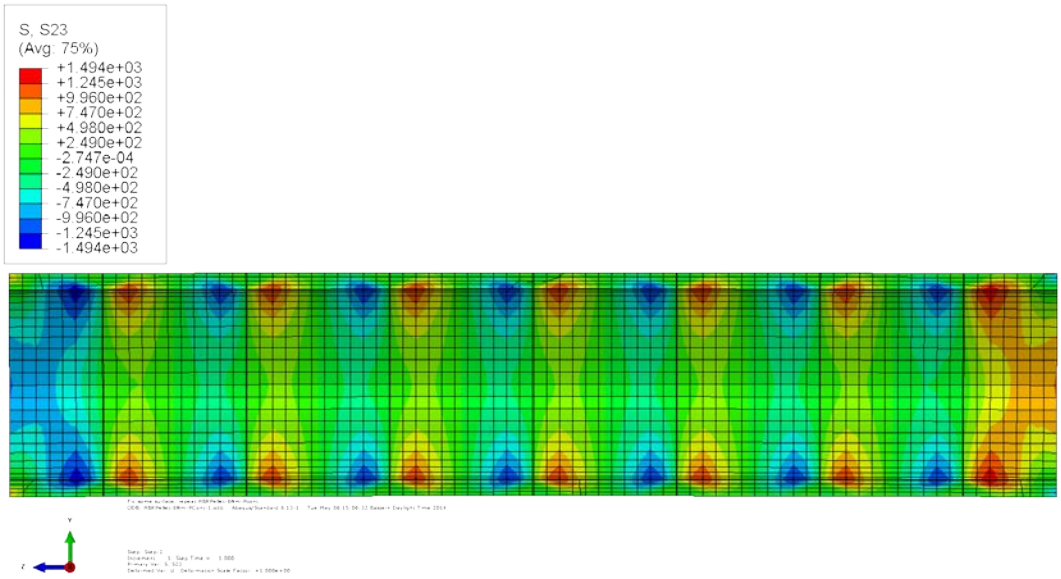

(c) Shear stress σ_{yz}

Figure 14. Shear stress distribution at the clad of the clad-epoxy-pellet section model of HBR pellets with debonded pellet-pellet interfaces with gaps and bonded pellet-clad interfaces using epoxy.

2.2.1.2 Interfacial Material with 10 × Young's Modulus

The second case study of simulated pellet-pellet interfacial debonding was defined as having gaps at the pellet-pellet interfaces and a thin layer of cohesive bonding material at the pellet-clad interfaces. The cohesive bonding material is also tied to the adjacent surfaces, resulting in perfect cohesive bonding. Similar to the second case of the perfect bond study, the Young's modulus of the cohesive bonding material at the pellet-clad interfaces was set to 10 times that of epoxy. Loading and boundary conditions were all the same as in the previous cases.

Figure 15 illustrates the simulation results for the pellet-pellet interfacial debonding condition, which shows a stress profile similar to that in Figure 13. However, stress concentrations are observed on both the pellets and the clad at pellet-pellet interfaces, as shown in Figure 15(b) in a detail view. The pellet-clad interaction tied by stiffer cohesive bonding causes stress concentrations on the pellets. The maximum stress on the Zr-4 clad occurs at the top and bottom portions of the pellet-pellet interface regions as a result of significant load shifting to the clad, whereas most of the clad has low stress because of the perfect pellet-clad bond. The HBR pellets and Zr-4 clad are all under yield stress. The cross section view of the resultant σ_{zz} shows that the maximum compressive stress fields reside in the cohesive bonding layer. The pellets have the same stress distribution depicted by the vertical dog-bone shape as in the previous case. The induced curvature of this pellet-pellet interface debonding in the stiffer cohesive bonding case is 0.118 m^{-1}, much small than that in the previous pellet-pellet interface debonding case. The big difference for this case compared with the debonded pellet-pellet interfaces with gaps is the stress concentration on the pellets as a result of stiffer cohesive bonding. Therefore, in this case, the HBR pellets would take more bending moment than those in the first simulation case.

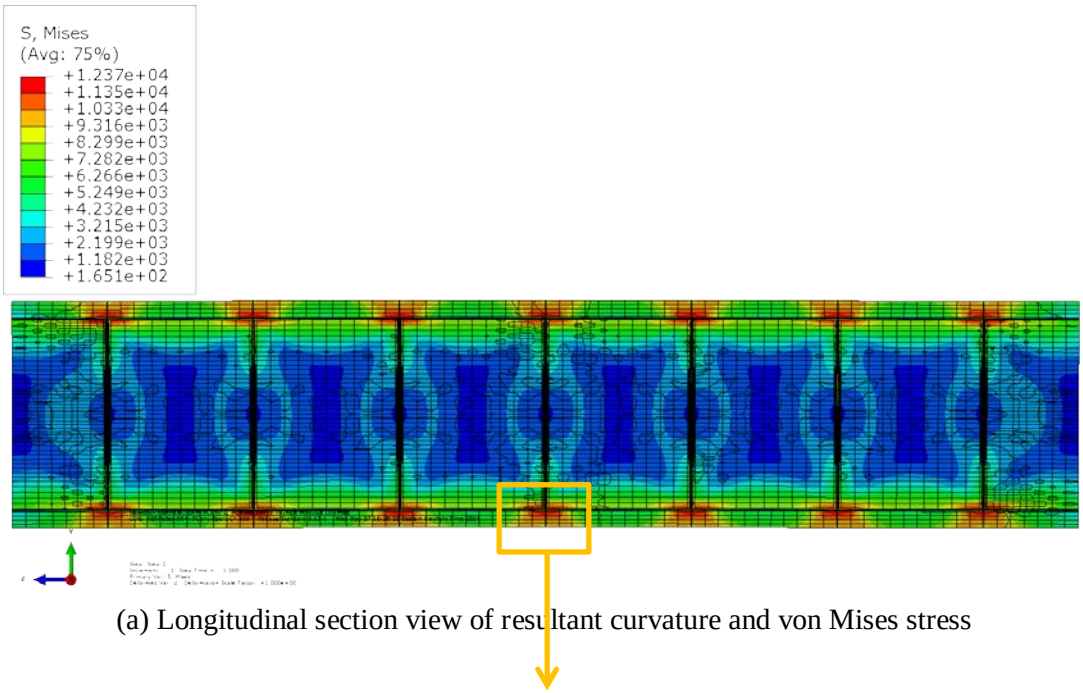

(a) Longitudinal section view of resultant curvature and von Mises stress

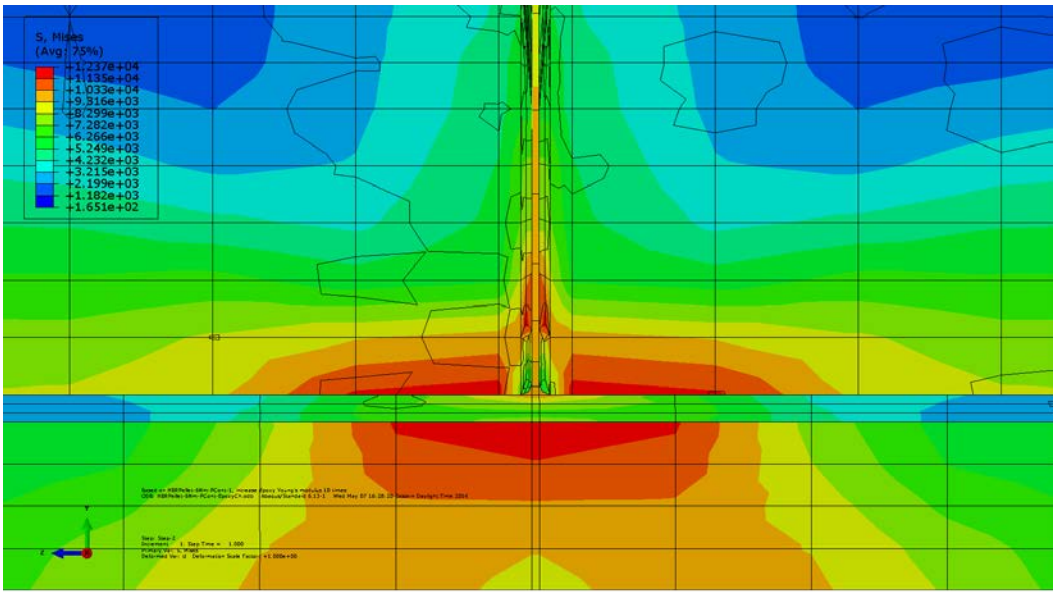

(b) Detail view

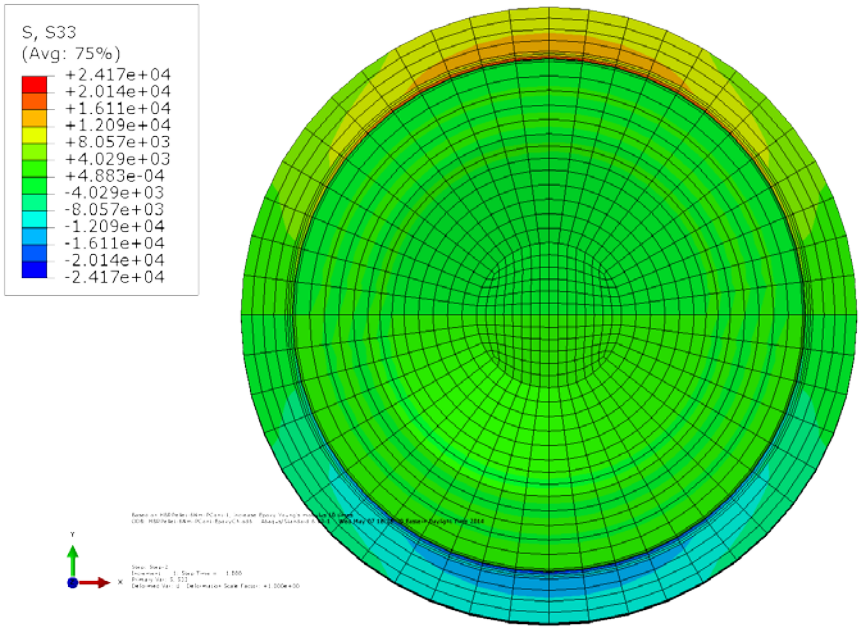

(c) Cross section view of σ_{zz} at a pellet-pellet interface

Figure 15. Normal stress distribution and curvature results for clad-epoxy-pellet section model of HBR pellets with debonded pellet-pellet interfaces with gaps, and bonded pellet-clad interfaces using a 10 × Young's modulus material.

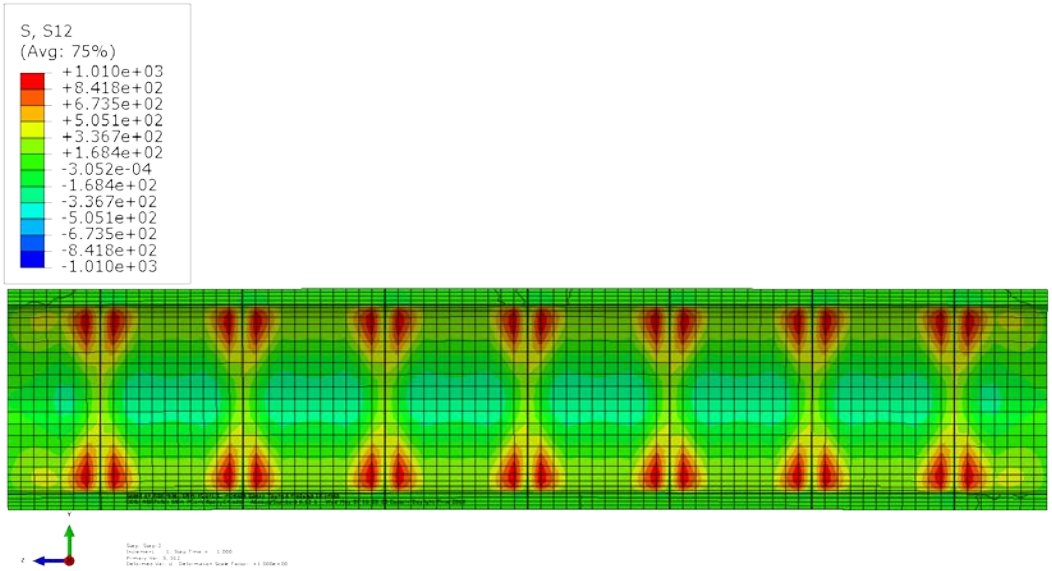

(a) Shear stress σ_{xy}

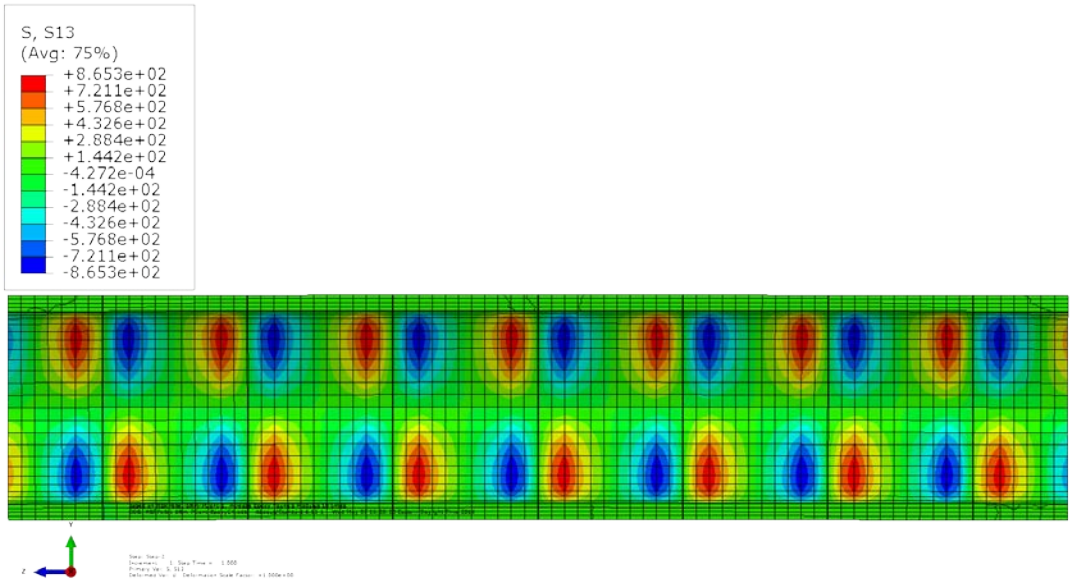

(b) Shear stress σ_{xz}

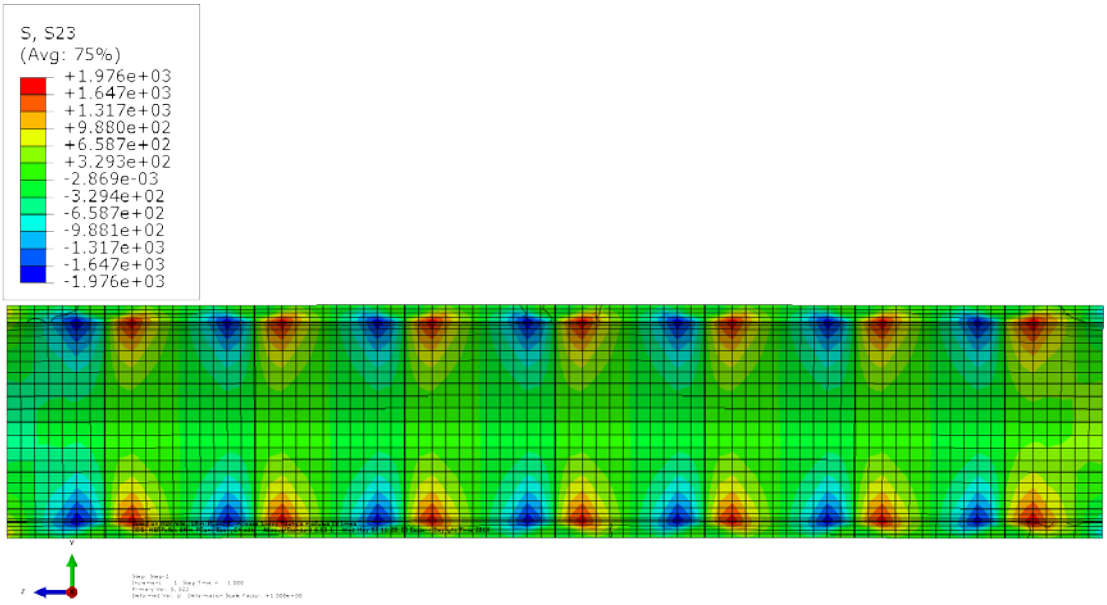

(c) Shear stress σ_{yz}

Figure 16. Shear stress distribution at the clad of clad-epoxy-pellet section model of HBR pellets with debonded pellet-pellet interfaces with gaps, and bonded pellet-clad interfaces using a 10 × Young's modulus material.

The results for shear stress distribution in Figure 16 show a similar pattern for the case in which epoxy is used as the cohesive bonding material. There are some changes in stress level, especially in the radial direction. For example, the maximum stress concentration in σ_{xy} is lower than the results in Figure 14, indicating that a stiffer interfacial material will increase the system stiffness and reduce the radial shear stress concentration under flexural deformation.

2.2.2 Debonded Pellet-Pellet Interfaces without Gaps

Figure 17 illustrates the simulations of debond pellet-pellet interface and bond pellet-clad interface. There are no gaps at the pellet-pellet interfaces before bending loading is applied. Similar to the previous cases, a thin layer is applied and tied to the surfaces at the pellet-clad interfaces to simulate good cohesive bonding or radial compressive residual stress. Except for elimination of the gaps at the pellet-pellet interfaces, the geometry, materials, and loading and boundary conditions are all the same as in the previous simulations.

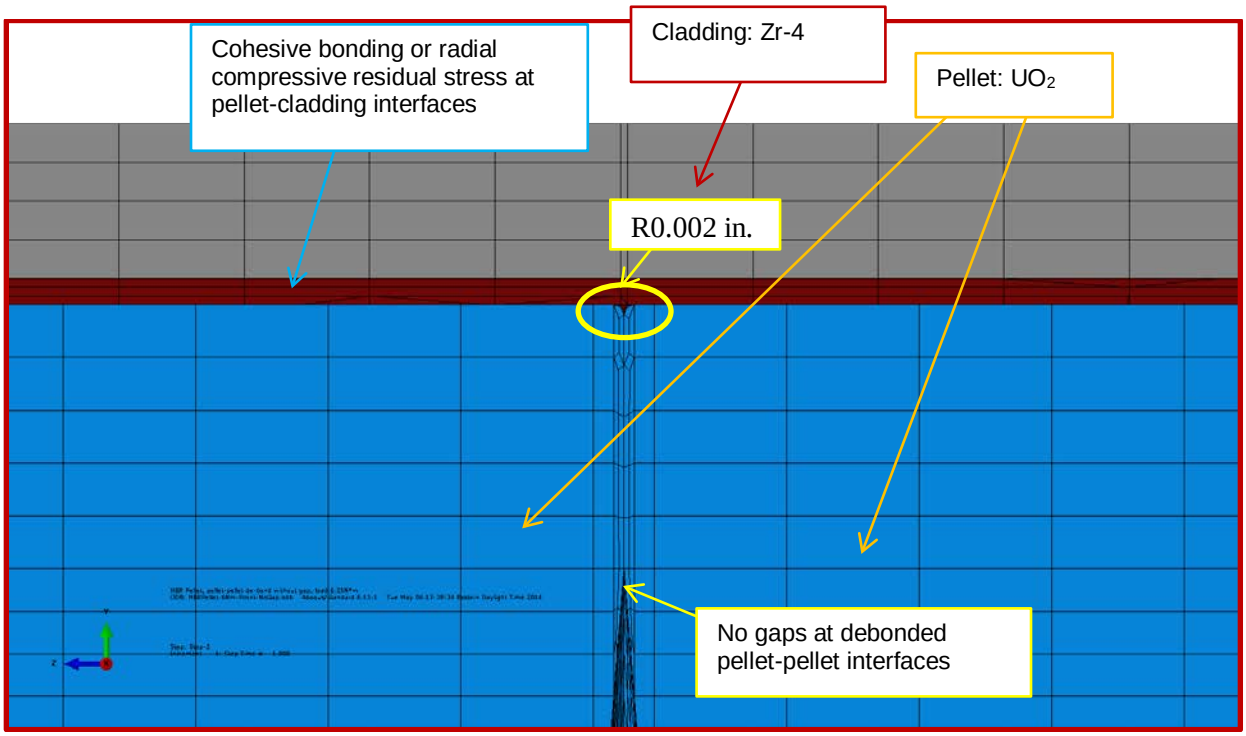

Figure 17. Detail from Figure 4 for the case of no gaps at debonded pellet-pellet interfaces.

2.2.2.1 Epoxy Used as Interfacial Material

For the third case in this section, the cohesive bonding material is an epoxy layer with the original Young's modulus. As illustrated in Figure 18, the normal stress distribution of this case appears to be different from that of debonded pellet-pellet interface case with empty gaps shown in in Figure 13. The maximum stress occurs at the top of the clad at pellet-pellet interface regions; however, at the compression side, interface stress concentrations occur at the pellets instead of at the clad. This is because there are no gaps at the pellet-pellet-clad interface region. Thus the contact pellets provide good internal support to the clad tubing structure. Furthermore, the pellets seem to carry a significant portion of the bending moment resistance via pellet-pellet interaction (pinching at pellet corners), which significantly mitigates the stress level of the clad at the bottom (compression) region. Because of the high yield strength of the pellet and clad materials, as well as the small bending load, the pellets and the clad are all under the linear elastic range at the maximum stress level. The pellet stress profiles do not show a clear dog-bone shape because of the asymmetric contact between the tension and compression sides at the debonded pellet-pellet interfaces. The resultant σ_{zz} profile without gaps at the pellet-pellet interface indicates that the pellets can carry more bending moment resistance than the pellets with gaps shown in Figure 13.

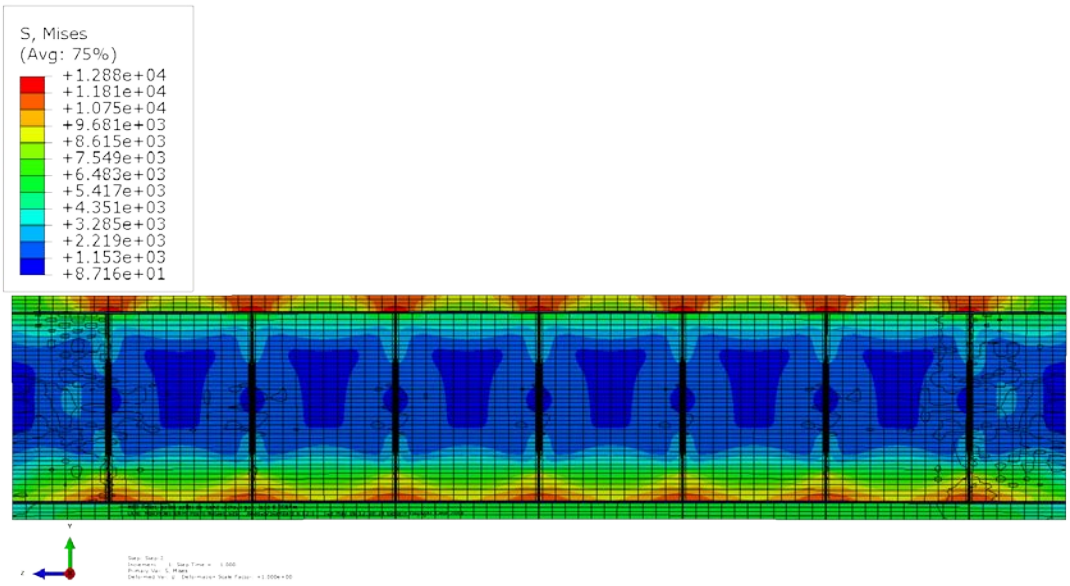

(a) Longitudinal section view of resultant curvature and von Mises stress

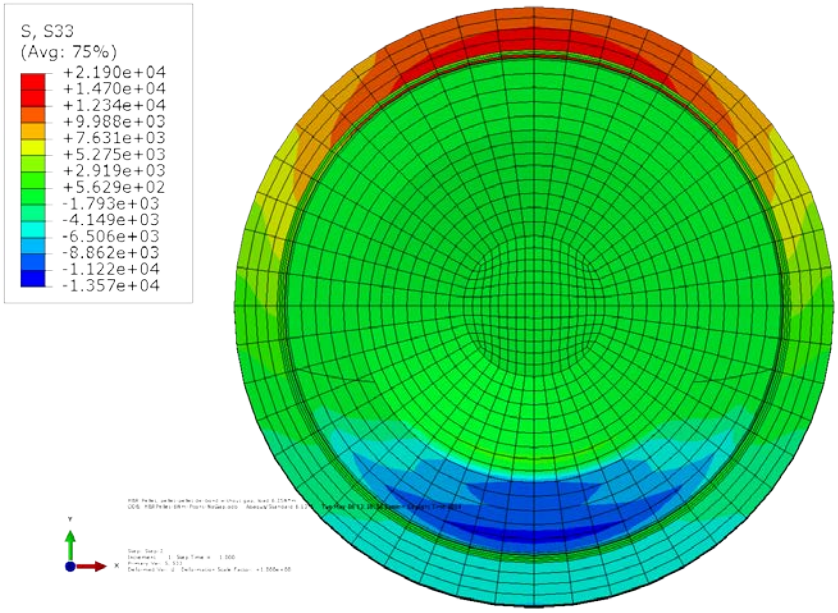

(b) Cross section view of σ_{zz} at a pellet-pellet interface

Figure 18. Normal stress distribution and curvature results for clad-epoxy-pellet section model of HBR pellets with debonded pellet-pellet interfaces without gaps, and bonded pellet-clad interfaces using epoxy.

Figure 19 shows the shear stress distribution at the clad for this case. The shear stress concentration occurs only at the top tension side, unlike in the case for pellet-pellet interface debonding with small gaps. The maximum stress concentration level is close to the results in Figure 14. At the bottom compression side, the shear stress level is low. The reason is the same as for the normal stress results: when the gaps are eliminated, pellet-to-pellet direct pinning helps lower the stress on the clad at the bottom region.

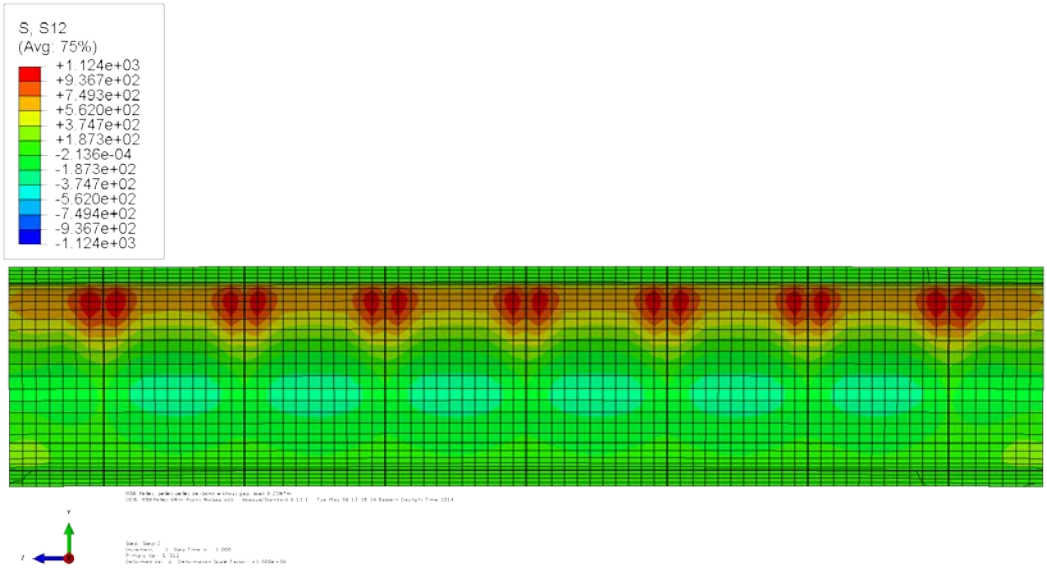

(a) Shear stress σ_{xy}

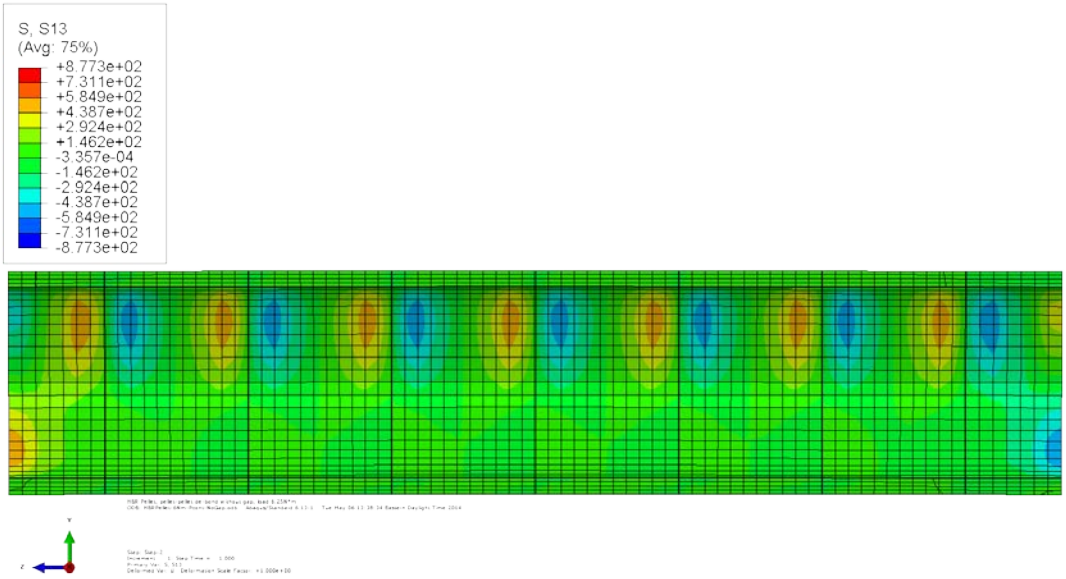

(b) Shear stress σ_{xz}

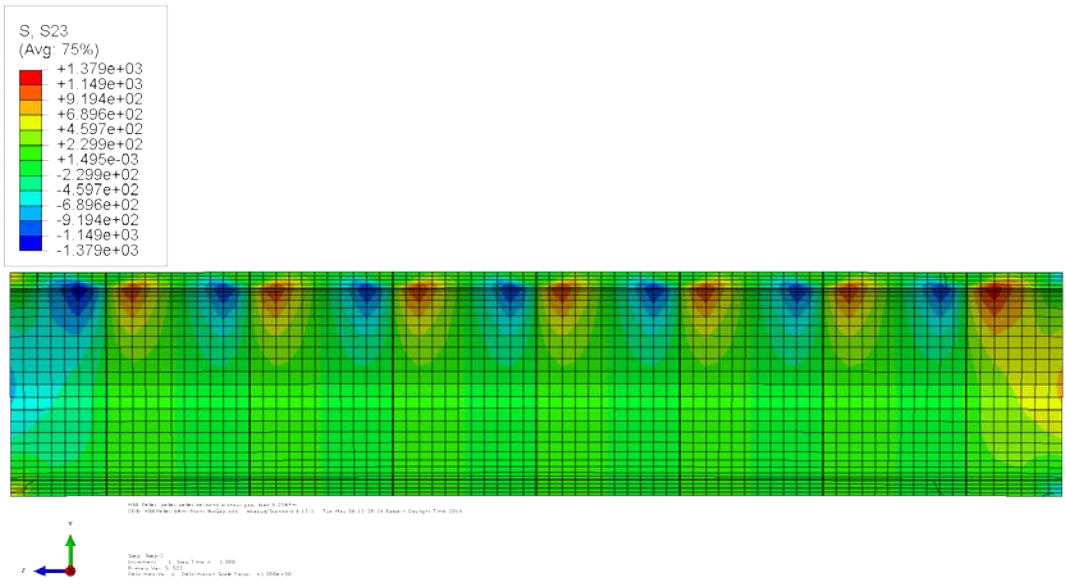

(c) Shear stress σ_{yz}

Figure 19. Shear stress distribution at the clad of the clad-epoxy-pellet section model of HBR pellets with debonded pellet-pellet interfaces without gaps, and bonded pellet-clad interfaces using epoxy.

2.2.2.2 Interfacial Material with 10 × Young's Modulus

The fourth case in this section is similar to the third case for debonded pellet-pellet interfaces without gaps between the interfaces. The difference is that the Young's modulus of the bonding material was set to 10 times that of epoxy, as in the second simulation case. Figure 20 shows the resulting normal stress distribution and curvature. The stress distribution generally is similar to that of the case illustrated in Figure 18. The maximum stress on the clad occurs at the top pellet-pellet interface regions; and at the compression side, the pellet pinching helps reduce the stress level at the bottom of the clad. However, stress concentrations occur both at the tops of the pellets (because of the stiffer cohesive bonding) and at the bottom pellet-pellet corners because of the direct contact between pellets. The maximum von Mises stress level is higher than that shown in Figure 18, but no material yields. The σ_{zz} results show a higher level stress concentration in the fuel rod system than that shown in Figure 18.

Figure 21 illustrates results for shear stress at the clad that are similar to the results in the third simulation case (Figure 19). There is no shear stress concentration at the bottom compression region, although the maximum shear stress levels are close to those in the second simulation case (Figure 16) because the same cohesive bonding material was used.

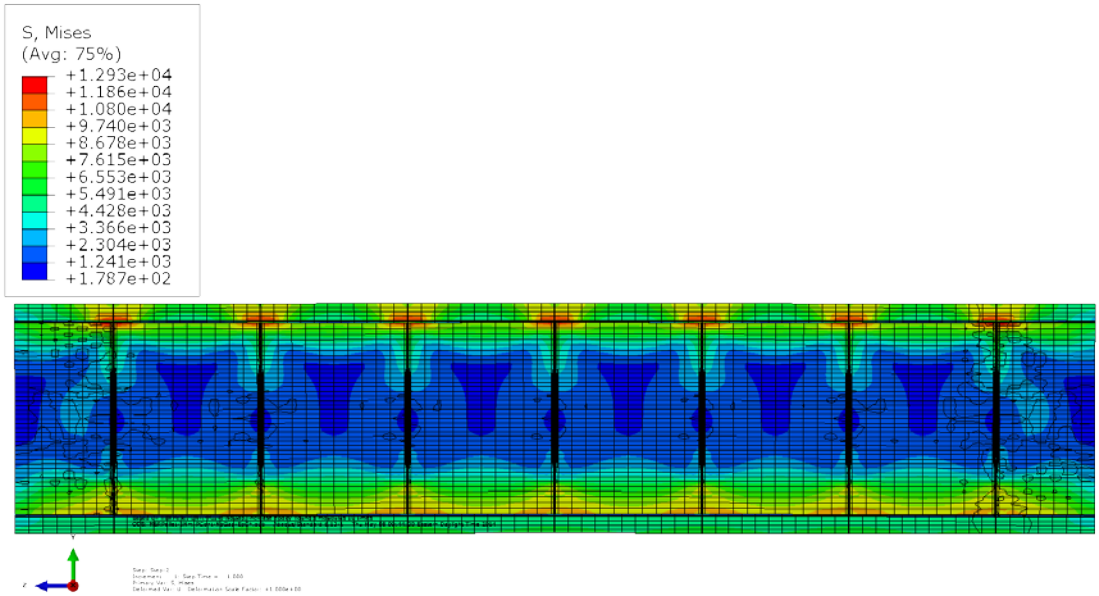

(a) Longitudinal section view of resultant curvature and von Mises stress

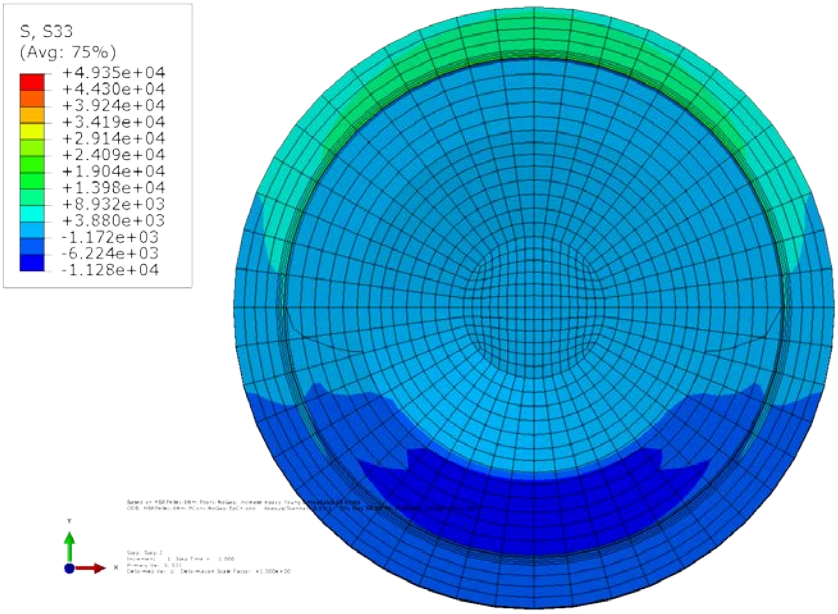

(b) Cross section view of resultant σ_{zz} at a pellet-pellet interface

Figure 20. Normal stress distribution and curvature results for clad-epoxy-pellet section model of HBR pellets with debonded pellet-pellet interfaces without gaps, and bonded pellet-clad interfaces using a 10 × Young's modulus material.

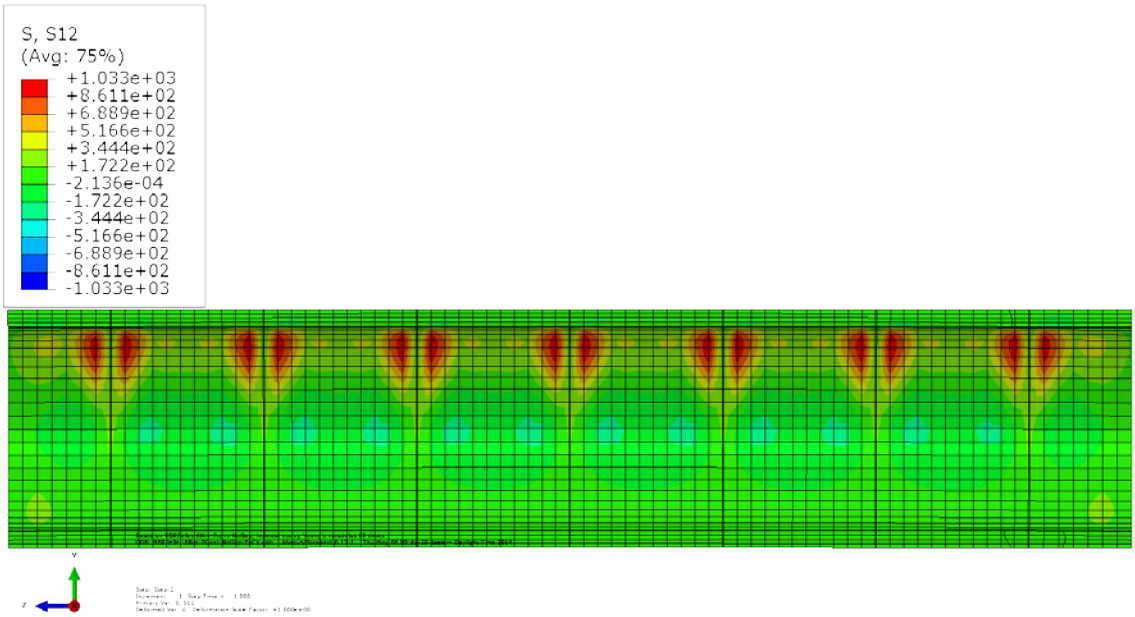

(a) Shear stress σ_{xy}

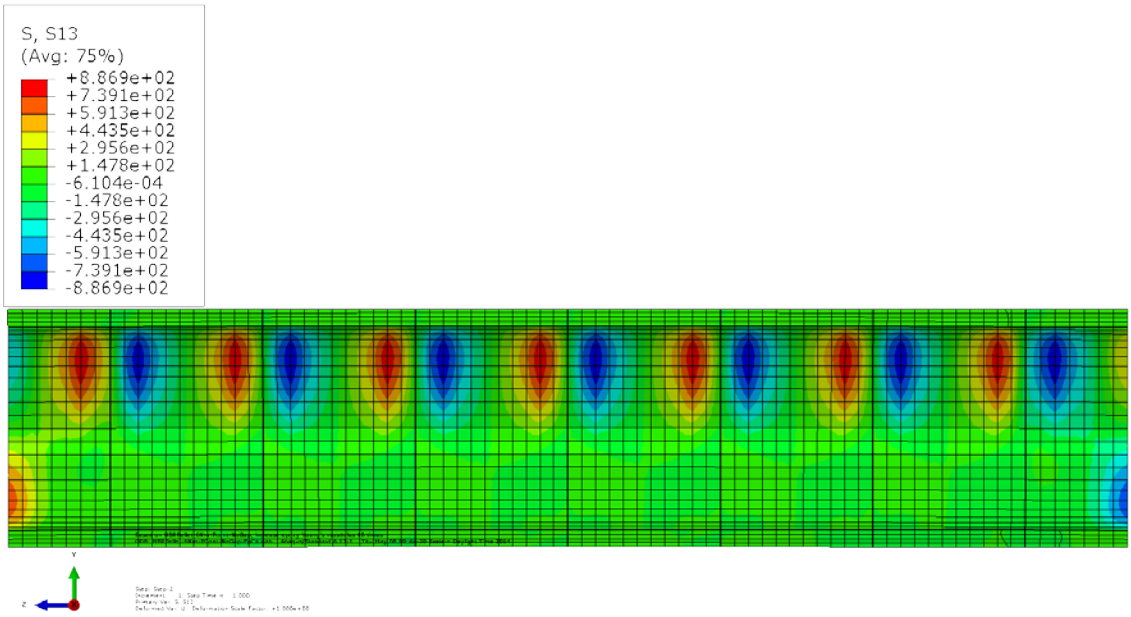

(b) Shear stress σ_{xz}

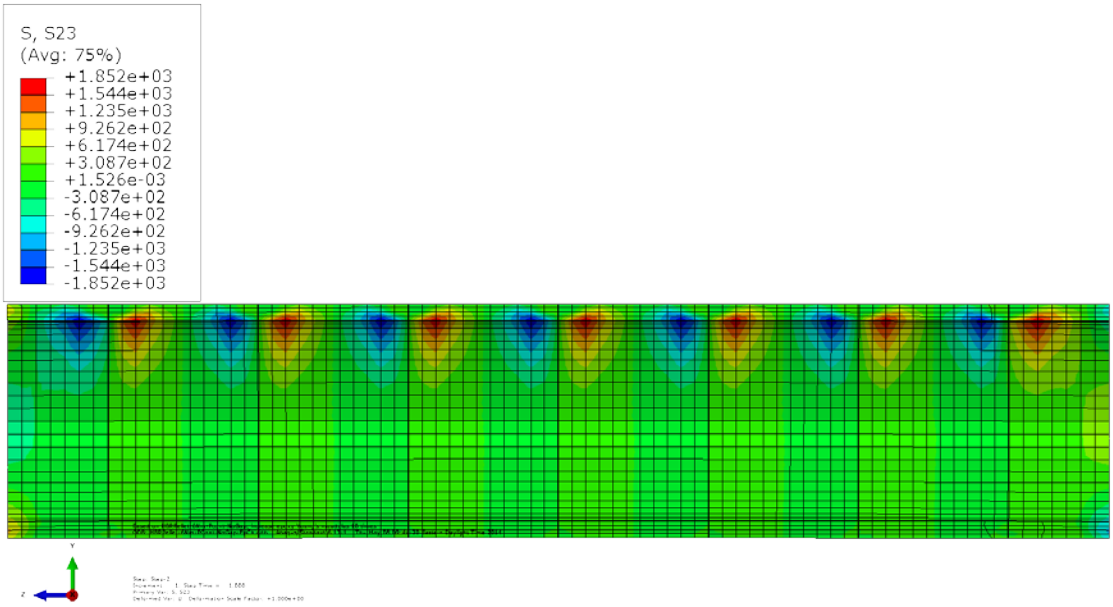

(c) Shear stress σ_{yz}

Figure 21. Shear stress distribution results at the clad of the clad-epoxy-pellet section model of HBR pellets with debonded pellet-pellet interfaces without gaps, and bonded pellet-clad interfaces using a 10 × Young's modulus material.

Table 3 summarizes the estimate curvature, flexural rigidity, and components load-carrying capacity from the four FEA simulation cases discussed in this section. The same bending load, 6.25 N·m, was used in all of the FEA simulations. The curvature and the flexural rigidity listed in Table 3 indicate that for interface bonding simulation, the immediate consequence of debonding at the pellet-pellet interface is a significant increase in curvature, which results in a significant reduction in the estimated flexural rigidity. This phenomenon is primarily due to a shift in load-carrying capacity from the pellets to the clad.

Table 3. Comparison of curvature, flexural rigidity, and bending moment for the bonded pellet-clad and debonded pellet-pellet cases

	Curvature κ(1/m)	Flexural rigidity *EI* (N·m^2)	Clad bending moment *M* (N·m)	Pellet bending moment *M* (N·m)
Pellet-pellet interface with gap debonding; pellet-clad interface bonded with epoxy	0.160	39	5.73	0.52
Pellet-pellet interface with gap debonding, pellet-clad interface bonded with 10 × Young's modulus material	0.118	53	4.90	1.35
Pellet-pellet interface without gap debonding, pellet-clad interface bonded with epoxy	0.119	53	3.99	2.26
Pellet-pellet interface without gap debonding, pellet-clad interface bonded with 10 × Young's modulus material	0.097	65	3.52	2.73

The induced curvature of 0.160 m^{-1} for debonded pellet-pellet interfaces with gaps and a pellet-clad interface bonded with epoxy is twice the curvature value of 0.082 m^{-1} for the case of perfect bonding with epoxy in the gaps. The estimated flexural rigidity of 39 $N \cdot m^2$ for the case of a debonded pellet-pellet interface is a reduction of about 49% compared with of 77 $N \cdot m^2$ for perfect interfacial bonding.

Table 3 shows that there is a significant difference between curvature results for epoxy bonding at the pellet-clad interface and the results for a 10 × Young's modulus bonding material. As the Young's modulus of the bonding material increases, the curvature decreases by 26% for a pellet-pellet interface with gaps and by 18% for a pellet-pellet interface without gaps. The flexural rigidity increases by the same percentages as the curvature decreases, indicating that the 10 × Young's modulus material increases the stiffness of the composite system, and gaps at the pellet-pellet interfaces play a critical role in estimating the flexural rigidity of the HBR fuel rod. The induced curvature of 0.160 m^{-1} for the debonded pellet-pellet interfaces with empty gaps and a pellet-clad interface bonded with epoxy is 1.3 times that of the debonded pellet-pellet interfaces without gaps. The result is a 26% reduction in flexural rigidity, from 53 $N \cdot m^2$ for the case with no gaps to 39 $N \cdot m^2$ for the case with empty gaps. The pellet-clad interface bonded with the 10 × Young's modulus material showed a similar impact when the gaps were eliminated. In Table 2, the perfectly bonded pellets carry more bending moment than the clad. In Table 3, the data clearly show a significant shift in bending moment resistance from the pellets to the clad as a result of debonding at pellet-pellet interfaces. For all four simulation cases discussed in this section, the clad takes more of the bending moment than the pellets. In the fuel rod with the stiffer cohesive bonding material, the clad carries less bending load than in the rod with epoxy as the bonding material. When the pellets directly contact one another without gaps, the bending moment on the clad drops by around 30% compared with the pellets with empty gaps.

These results indicate that the gap-induced stress concentration and large deformations of the clad at the pellet-pellet interface region can lead to a significant reduction in the bending stiffness, i.e., flexural rigidity (*EI*), of the fuel rod system. If there are no gaps at the pellet-pellet interfaces, the pellets can carry a significant portion of the bending moment resistance via direct pellet-pellet contact (interaction) to mitigate the stress concentration and potential yielding at the clad.

2.3 Debonded Pellet-Clad and Pellet-Pellet Interfaces

Under flexural deformation, high shear stress will arise at the pellet-clad interfaces to compensate for the material mismatch and the flexural shear stress in the SNF system. Thus under reversal bending loading during normal transportation, both cyclic normal stress and shear stress can further degrade the interface bonding at pellet-clad interfaces. In this section, debonded pellet-clad interfaces and debonded pellet-pellet interfaces are investigated using the clad-epoxy-pellet section model with eight HBR pellets.

2.3.1 Debonded Pellet-Clad Interfaces and Debonded Pellet-Pellet Interfaces with Empty Gaps

As illustrated in Figure 22, simulations of interfacial debonding at both pellet-clad and pellet-pellet interfaces initially focus on the case with empty gaps at debonded pellet-pellet interfaces and a thin layer at debonded pellet-clad interfaces. At pellet-clad interfaces, the outer pellet surfaces contact the inner surface of the thin layer, and the outer surface of the thin layer contacts the inner surface of the clad. Pellets have dips at both end surfaces with rounding of 0.002 in. A fuel rod consisting of Zr-4 clad and HBR pellet inserts is used to study the system response to the bending moment with debonded interfaces. Loading and boundary conditions are the same as that assumed in the previous cases, and the bending moment is assigned at 6.25 N·m.

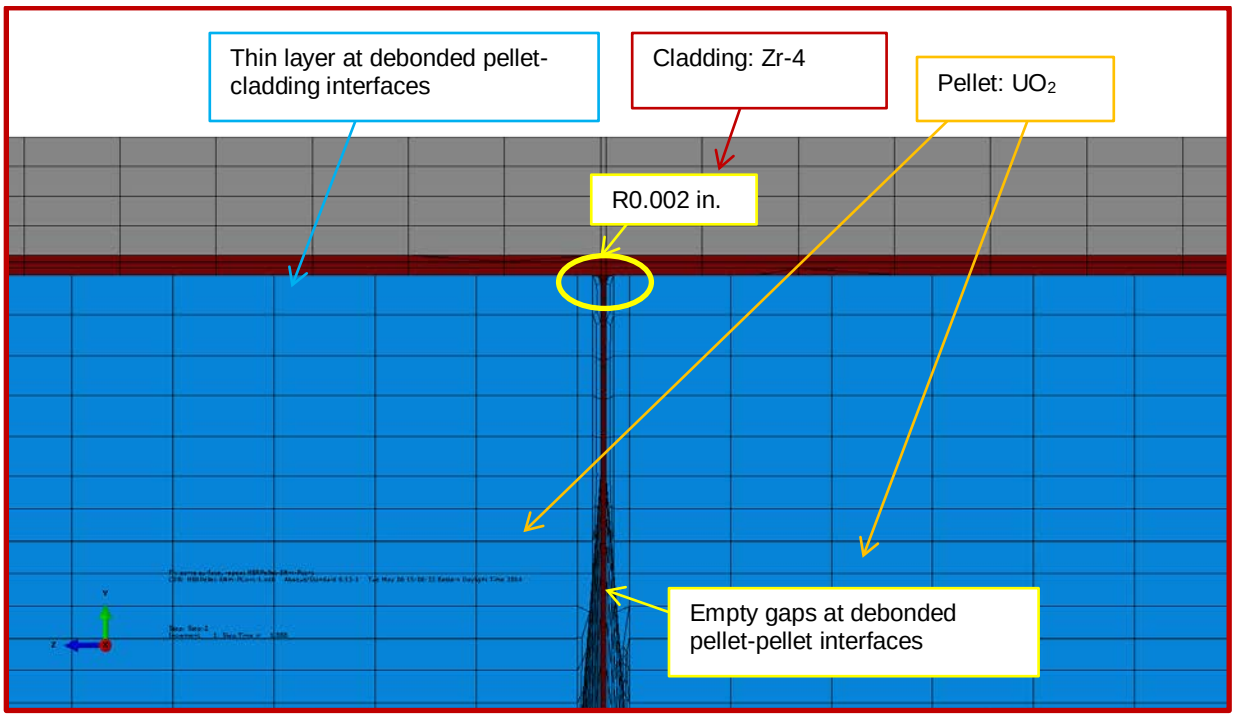

Figure 22. Detail area from Figure 4 for the cases of empty gaps at debonded pellet-pellet interfaces, and a thin layer filled at the debonded pellet-clad interfaces.

2.3.1.1 Epoxy Used as Interfacial Material

The first simulation began with a thin layer of epoxy. The resulting normal stress distribution shown in Figure 23 indicates that the clad reached maximum stress throughout the whole gauge section when interfacial debonding occurred at both pellet-clad and pellet-pellet interfaces. This result is in strong contrast to the results shown in Figure 13, in which the Zr-4 clad shows stress concentrations only locally at pellet-pellet interface regions. Because of the small bending load and the high material yield strength, the clad did not yield at the maximum stress. The pellets were all below the yielding stress, as well. The induced curvature of 0.218 m^{-1} is almost triple that of the perfect bond case. This suggests that, as a result of the interface debonding at both the pellet-clad and pellet-pellet interfaces, the pellets and the clad can contact (or pin) only at the pellet-pellet-clad interface region, and pellets cannot provide direct internal support to the clad. Therefore, the load-carrying capacity shifts significantly from the pellets to the clad at the entire gauge section. The results also indicate that the Zr-4 clad carries most of the bending moment resistance. The bending deformation in the debonded pellet-clad region is likely to result in further pinning action at pellet-clad interfaces, which may also result in accelerated aging of the clad tubing.

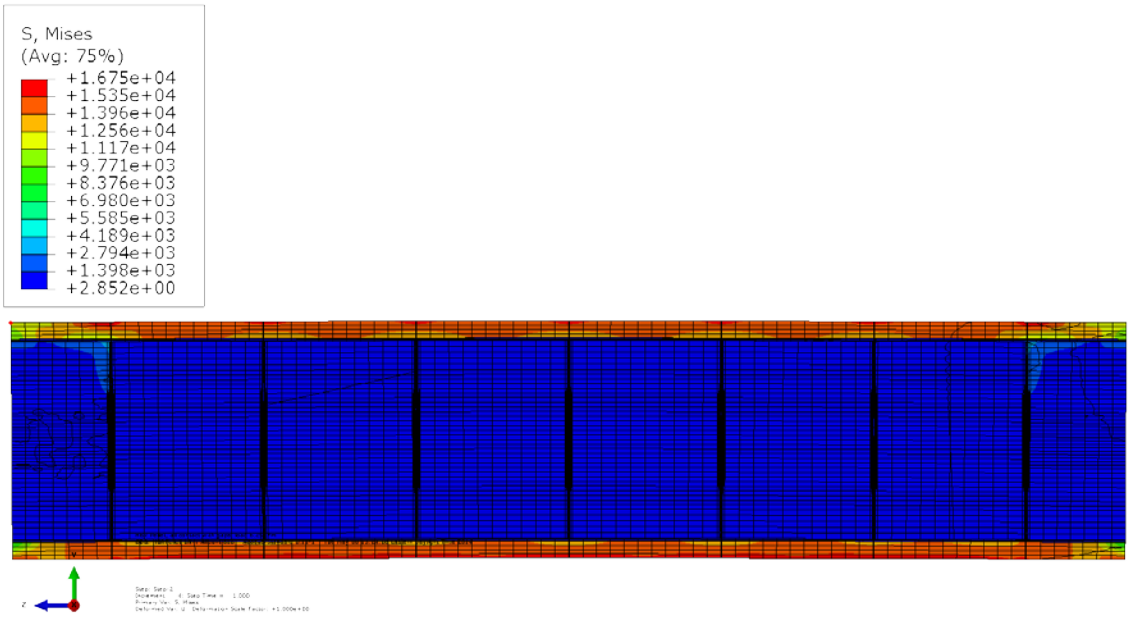

(a) Longitudinal section view of resultant curvature and von Mises stress

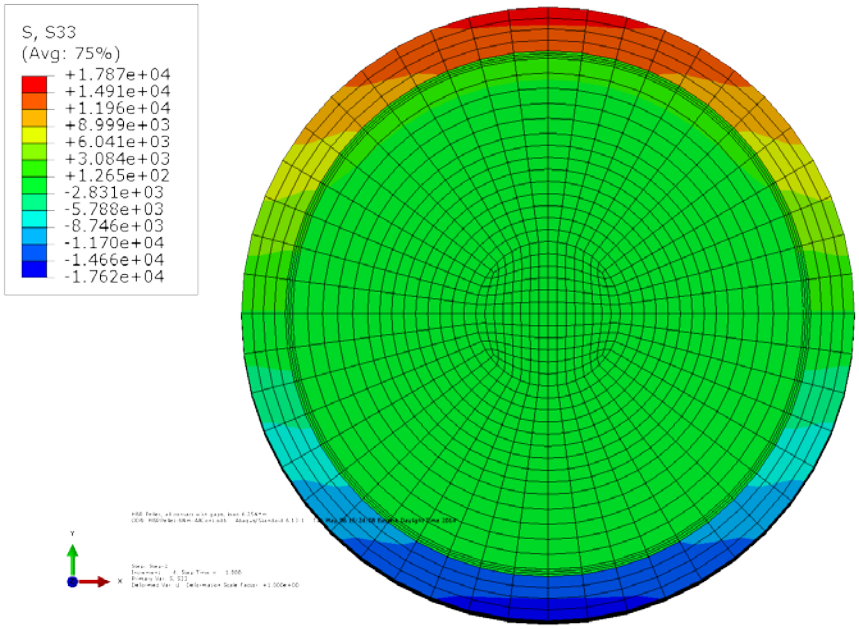

(b) Cross section view of σ_{zz} at a pellet-pellet interface

Figure 23. Normal stress distribution and curvature results for clad-epoxy-pellet section model of HBR pellets with empty gaps at debonded pellet-pellet interfaces, and an epoxy layer at debonded pellet-clad interfaces.

Figure 24 illustrates the shear stress results for this simulation case. The stress pattern appears to be similar to the perfect bond case. There are no shear stress surges inside the gauge section of the cladding as a result of further pellet-clad interface debonding. Because the pellets and the clad can make contact

only at the interfaces, the clad cannot directly transfer the shear stress within the gauge section. However, there are some stress concentrations at the boundary as a result of component contact.

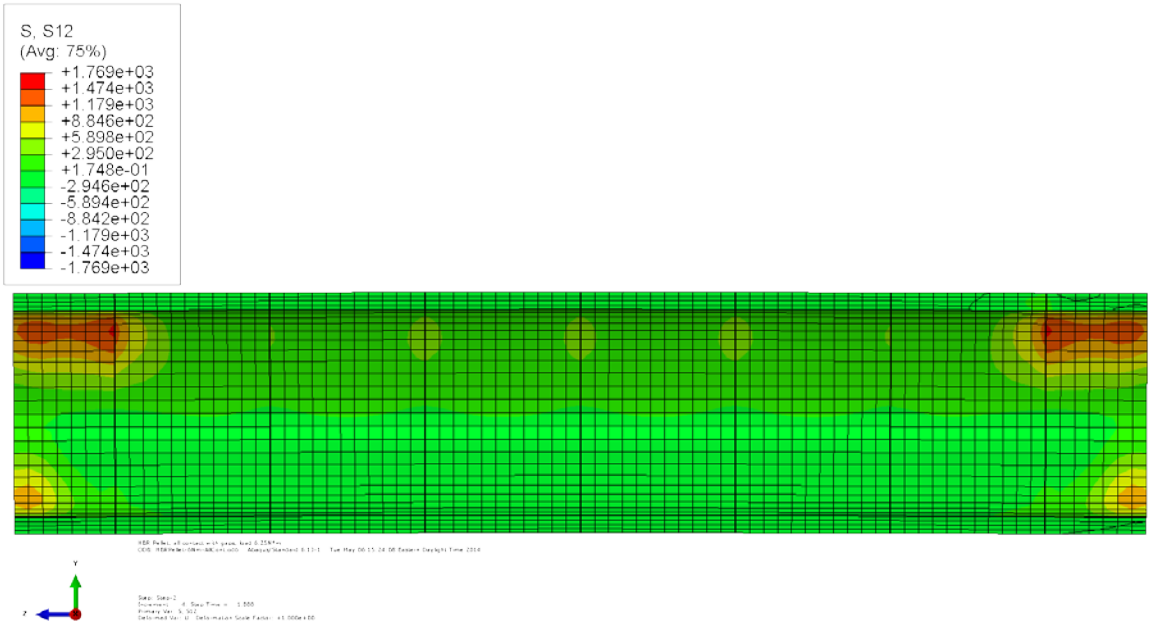

(a) Shear stress σ_{xy}

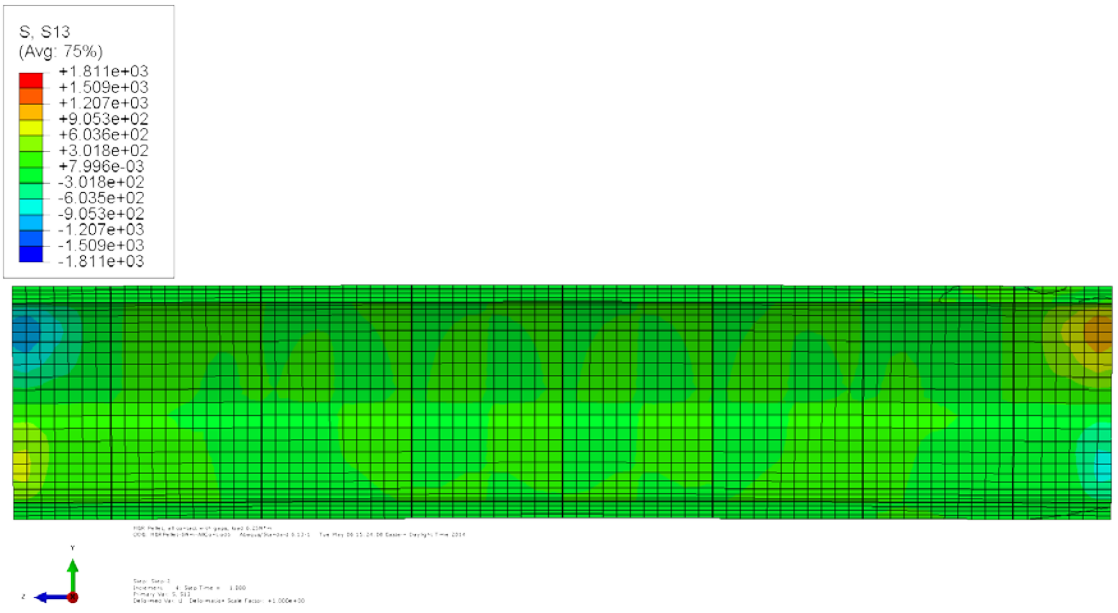

(b) Shear stress σ_{xz}

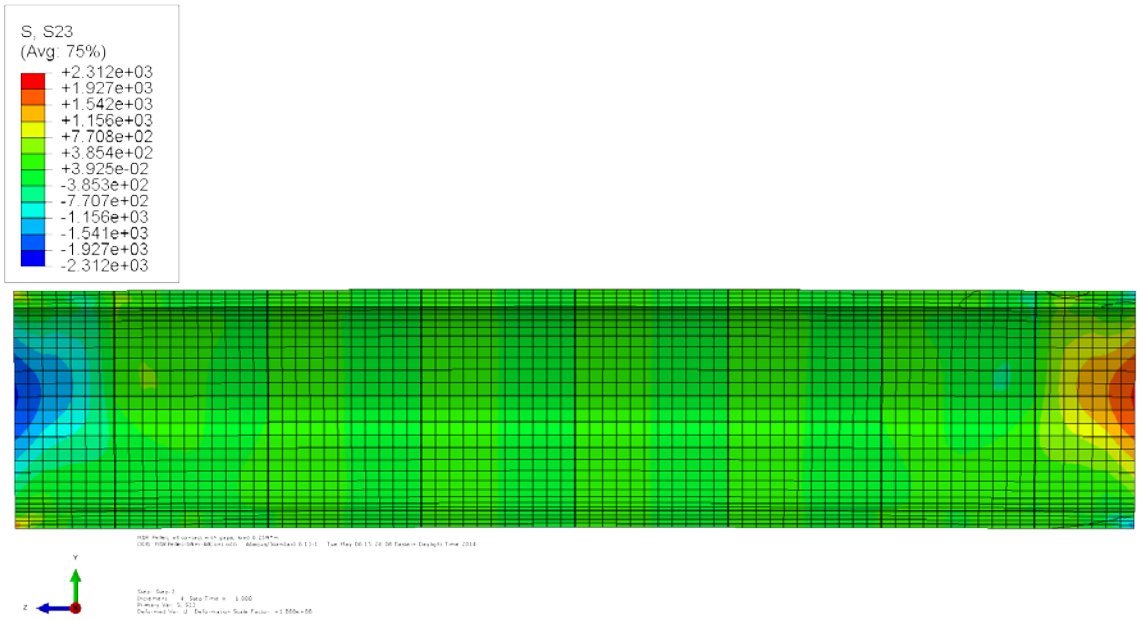

(c) Shear stress σ_{yz}

Figure 24. Shear stress distribution at the clad of the clad-epoxy-pellet section model of HBR pellets with empty gaps at debonded pellet-pellet interfaces, and an epoxy layer at debonded pellet-clad interfaces.

2.3.1.2 Interfacial Material with 10 × Young's Modulus

The second simulation case—interfacial debonding at both pellet-clad and pellet-pellet interfaces—used the same conditions as the first simulation except that the layer between the pellet and the clad had a Young's modulus 10 times that of epoxy.

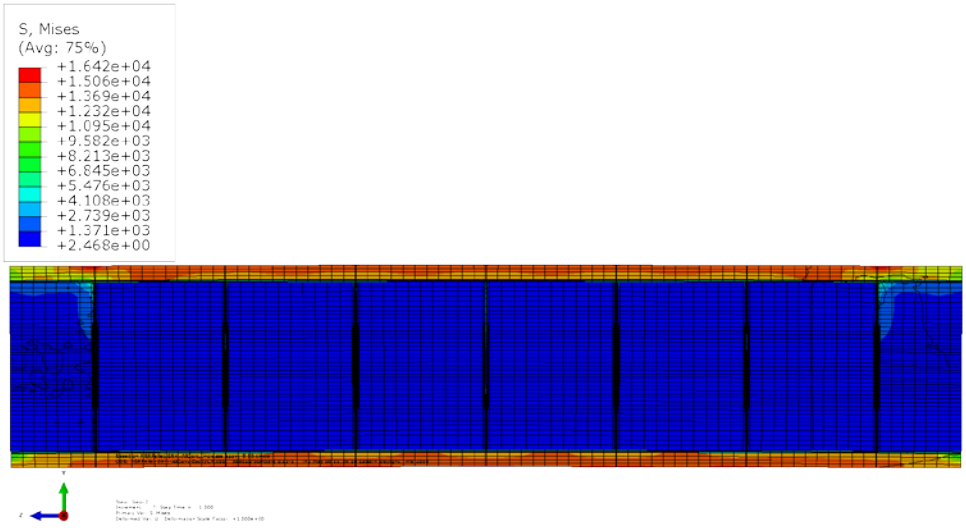

(a) Longitudinal section view of curvature and von Mises stress

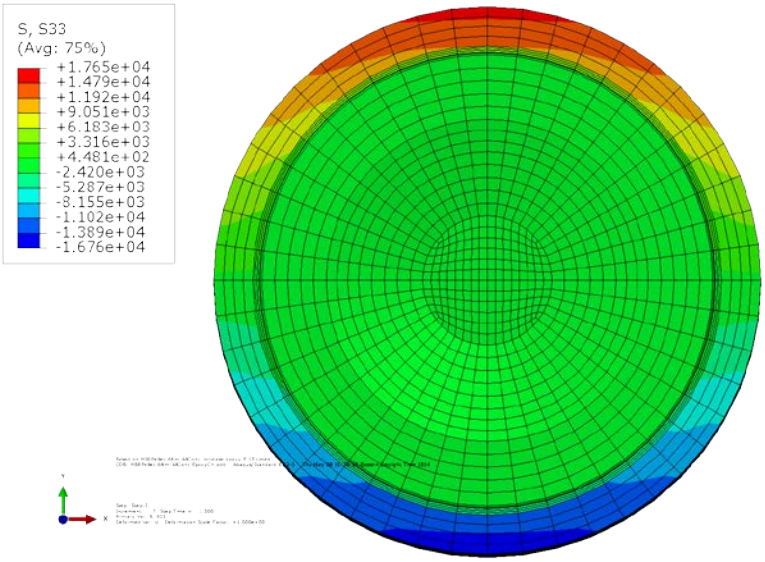

(b) Cross section view of σ_{zz} at a pellet-pellet interface

Figure 25. Normal stress distribution and curvature results for clad-epoxy-pellet section model of HBR pellets with empty gaps at debonded pellet-pellet interfaces, and a layer with a 10 × Young's modulus material at debonded pellet-clad interfaces.

Figure 25 shows normal stress distribution results very similar to those shown in Figure 23. The clad has reached maximum stress. The maximum stress level seen in the two figures is the same, which indicates that the property change in the interfacial material affects the bending response only slightly because of the interfacial debonding. Even though the stress concentration occurred over almost the entire gauge section, the maximum stress at the clad is still lower than the yielding strength. Therefore, the clad did not yield in this case.

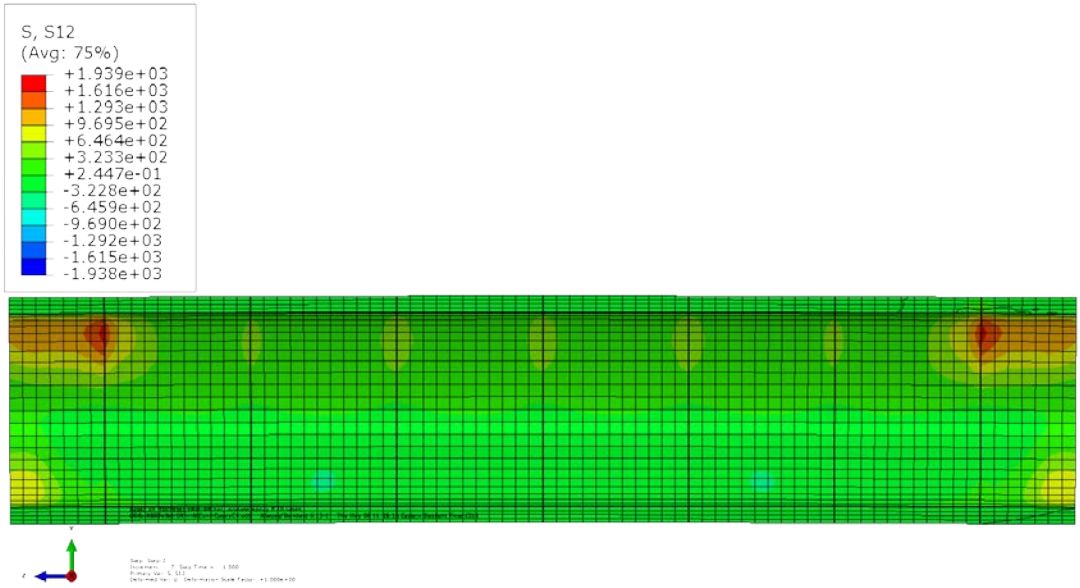

(a) Shear stress σ_{xy}

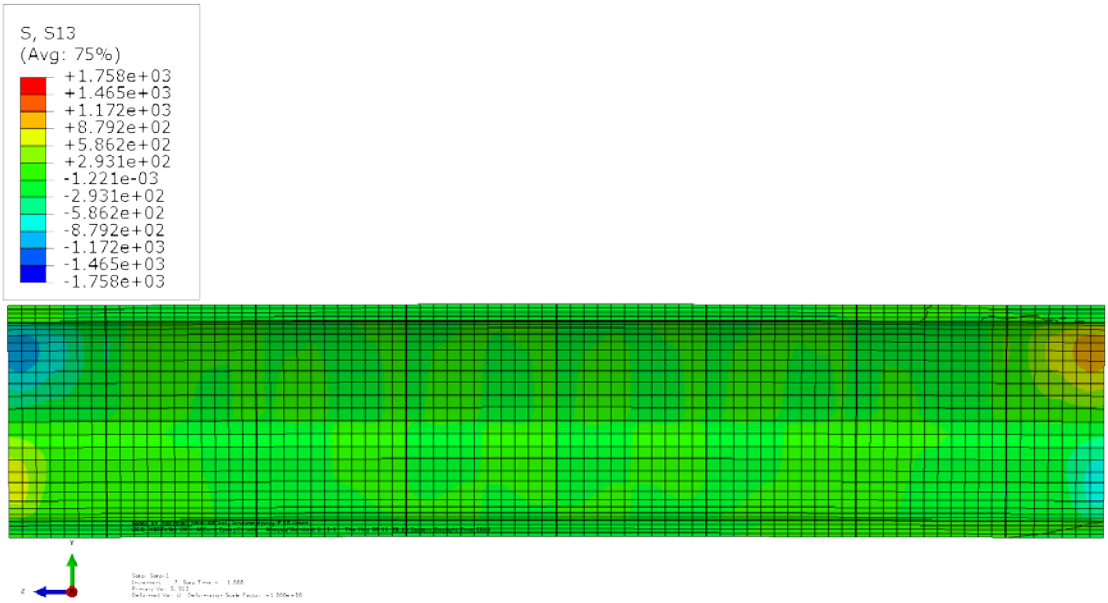

(b) Shear stress σ_{xz}

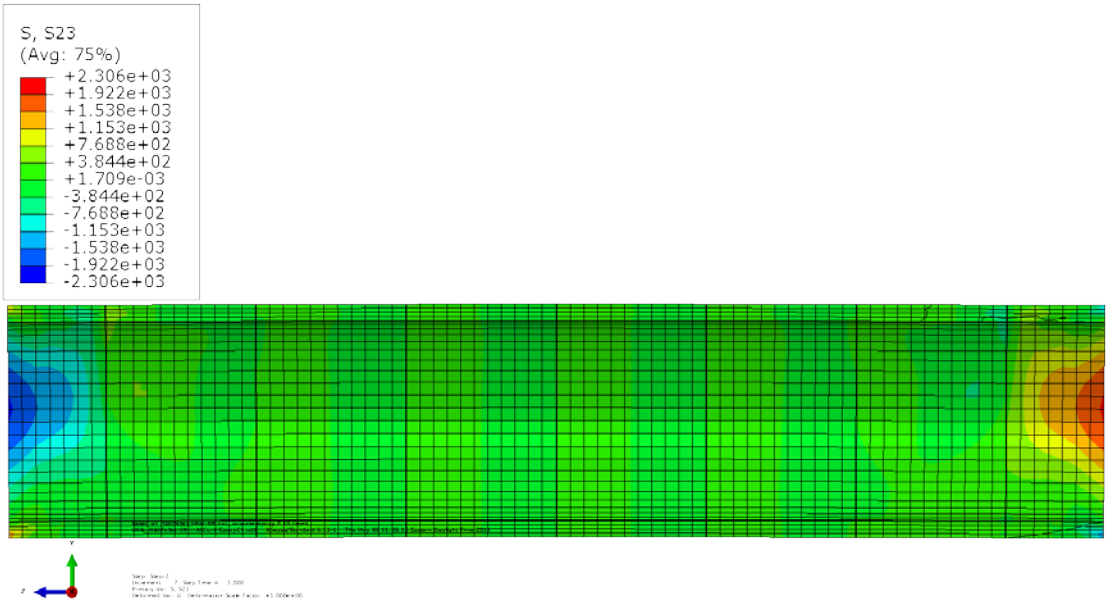

(c) Shear stress σ_{yz}

Figure 26. Shear stress distribution at the clad of clad-epoxy-pellet section model of HBR pellets with empty gaps at debonded pellet-pellet interfaces, and a layer of 10 × Young's modulus material at debonded pellet-clad interfaces.

The shear stress distributions in Figure 26 do not show a large change from the results of the first simulation case seen in Figure 24. There was no shear stress concentration inside the cladding. The stress levels are about the same as in Figure 24. That is because the pellets and the cladding contacted the bonding material as a result of the pellet-clad interfacial debonding. The interfacial material has a limited impact on the system's flexural response.

2.3.2 Debonded Pellet-Clad Interfaces and Debonded Pellet-Pellet Interfaces without Gaps

The simulation cases for debonded pellet-pellet interfaces without gaps are shown in Figure 27, where a thin layer is filled at debonded pellet-clad interfaces, and the pellets are all in direct contact with one another without gaps at the pellet-pellet interfaces. The loading and boundary conditions and the material properties are the same as in the previous cases. In this case, there are still eight HBR pellets with rounding of 0.002 in.

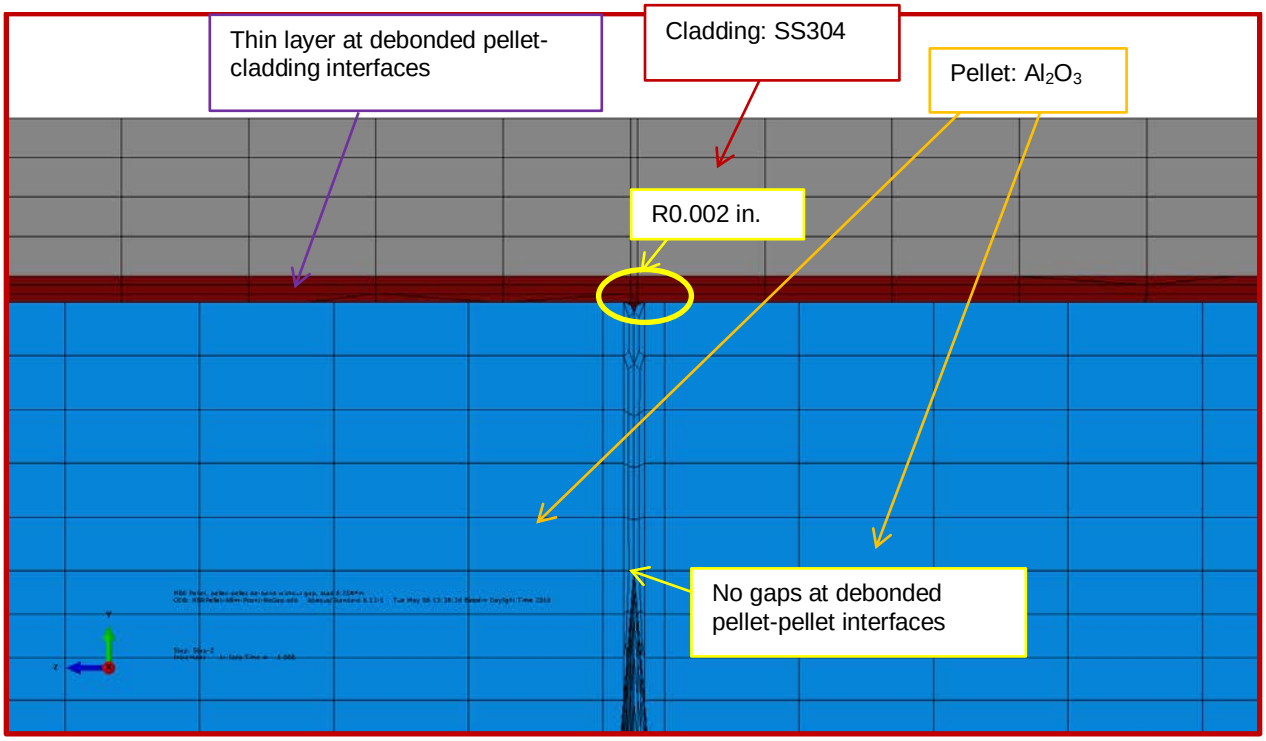

Figure 27. Detail area from Figure 4 for the case with no gaps at debonded pellet-pellet interfaces and a thin layer at debonded pellet-clad interfaces.

2.3.2.1 Epoxy Used as Interfacial Material

The third simulation case in this section used epoxy as the interfacial material filling the debonded pellet-clad interfaces and no gaps at debonded pellet-pellet interfaces. Figure 28 illustrates the HBR rod responses to the bending moment in this simulation. The longitudinal section view shows a stress concentration at the top (tension) region of the Zr-4 clad throughout the gauge section, but the rod did not yield. In the bottom (compression) region, the stress level is low at the clad. The maximum stress still occurred at the compression side of the pellet region where the pellets were pinned to one another. Figure 28 shows interfacial results similar to those observed in Figure 18 for the bonded pellet-clad interfaces and debonded pellet-pellet interfaces without gaps. The pellets carry a large portion of the bending moment resistance via the pinching pellet corners, and they reduce the stress intensity at the bottom (compression) portion of the clad. The major difference compared with the results shown in There is an extensive stress concentration observed at the top region of the clad throughout the entire gauge section which is in contrast to the localized area observed at the interface region as depicted in Figure 18.

The clad assumes most of the bending moment resistance because there is no direct mechanism for transferring the load from the pellet to the clad or vice versa due to the debonded pellet-clad interfaces.

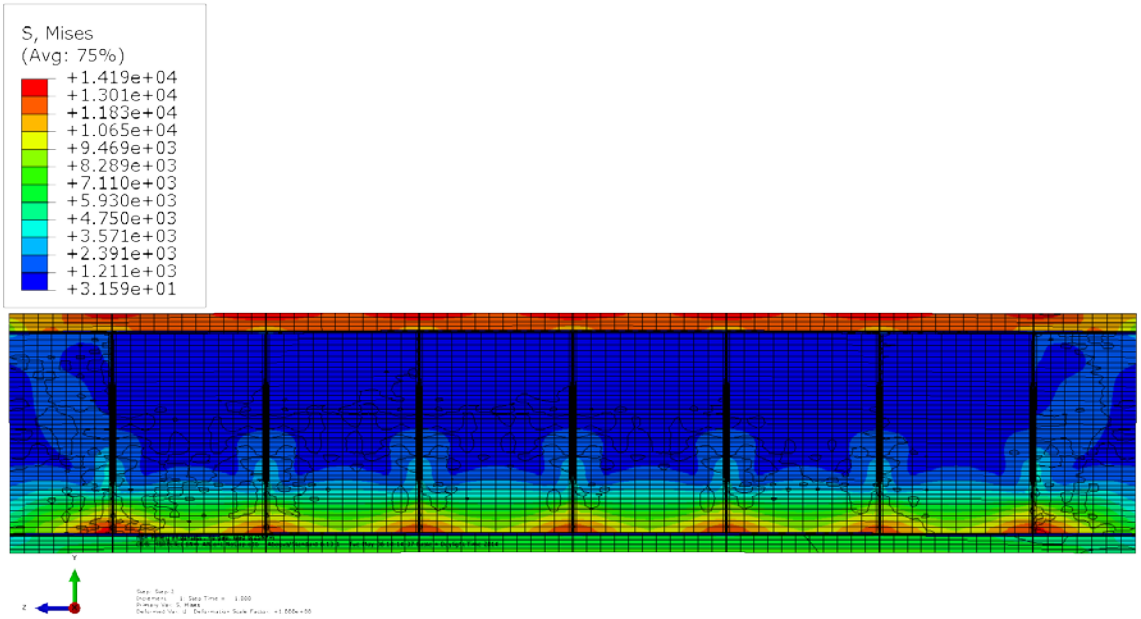

(a) Longitudinal section view of curvature and von Mises stress results

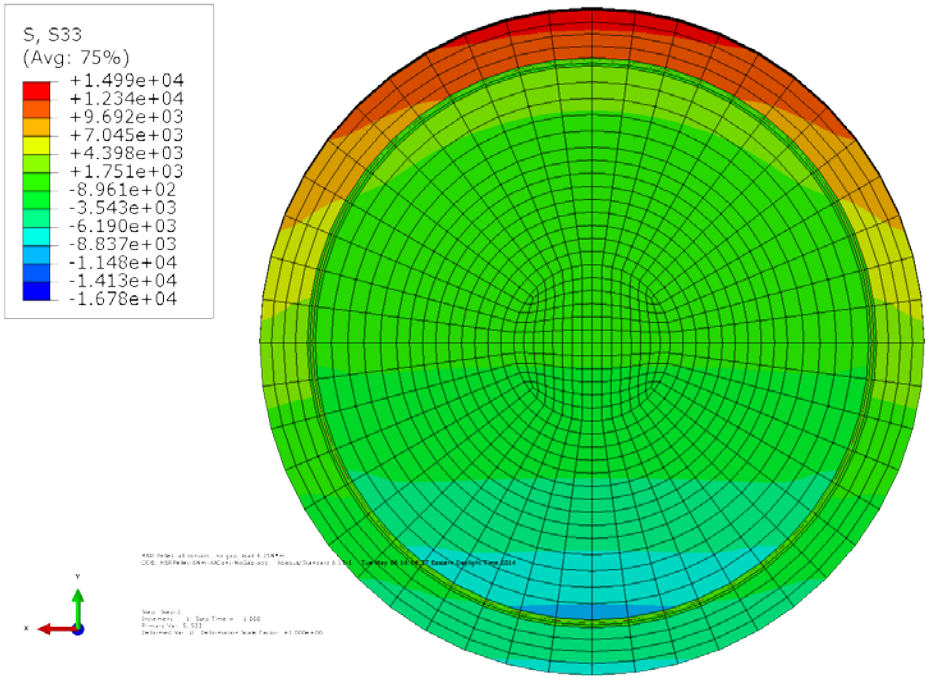

(b) Cross section view of the normal stress, σ_{zz}, results at a pellet-pellet interface

Figure 28. Normal stress distribution and curvature results for the clad-epoxy-pellet section model of HBR pellets without gaps at debonded pellet-pellet interfaces, and with an epoxy layer at debonded pellet-clad interfaces.

In Figure 29 (a), the shear stress in radial direction σ_{xy} shows different stress levels at the top tension side and bottom compression side at the clad. Similar to the normal stress distribution, the shear stress at the bottom side of the clad is significantly lowered by pellet-pellet direct pinching at the compression side. The shear stresses σ_{xz} and σ_{yz} show no stress concentration inside the clad, which appears to be a stress pattern similar to that for interface debonding with gaps. However, the maximum stress levels are lower than that for those cases. The pellets assume a large portion of the bending load when the gaps are eliminated.

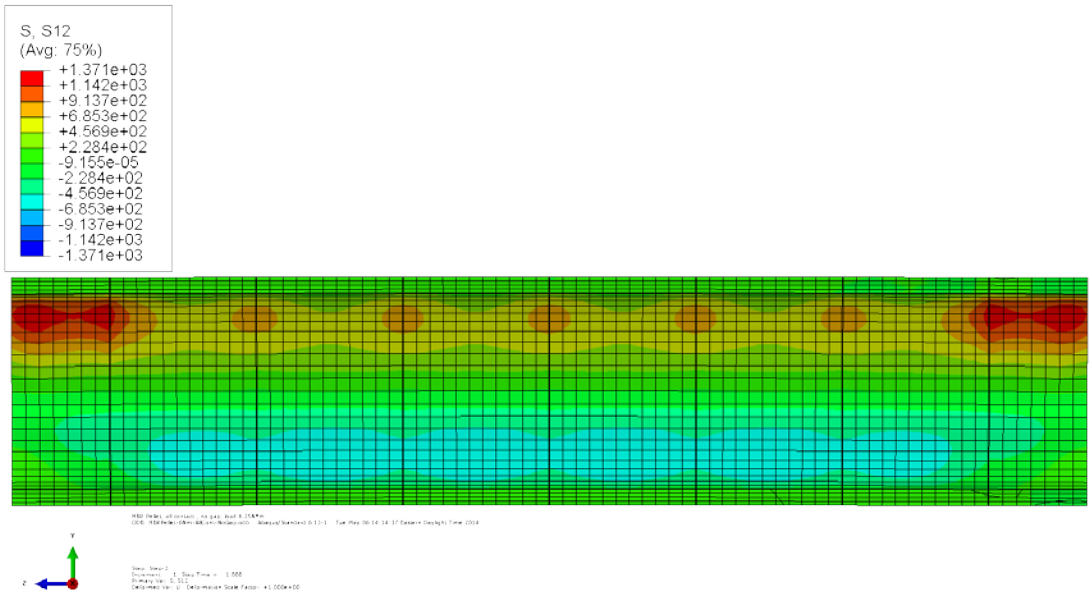

(a) Shear stress σ_{xy}

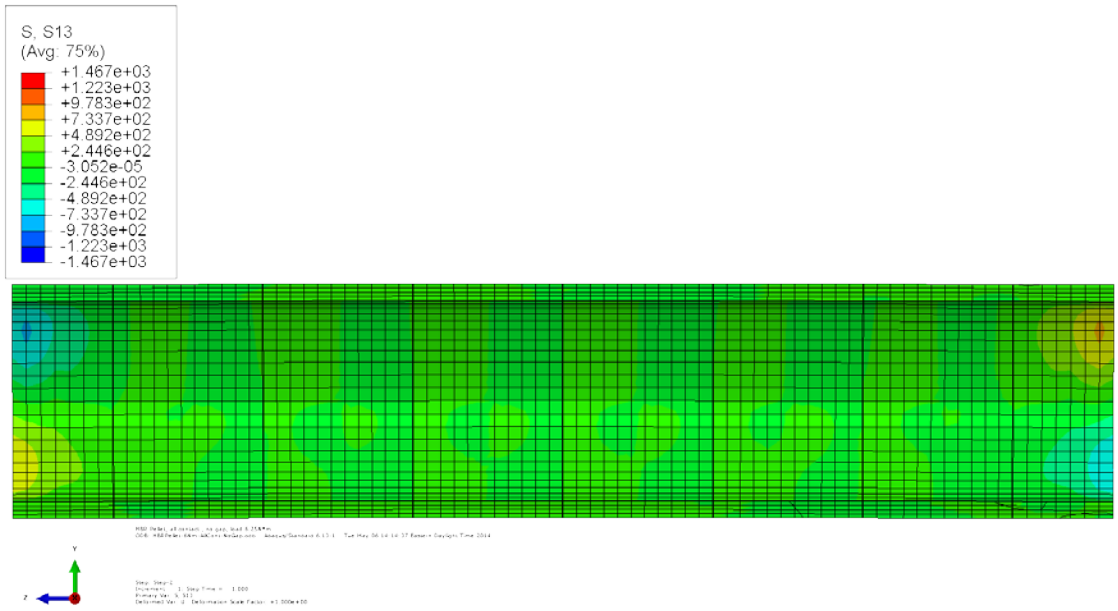

(b) Shear stress σ_{xz}

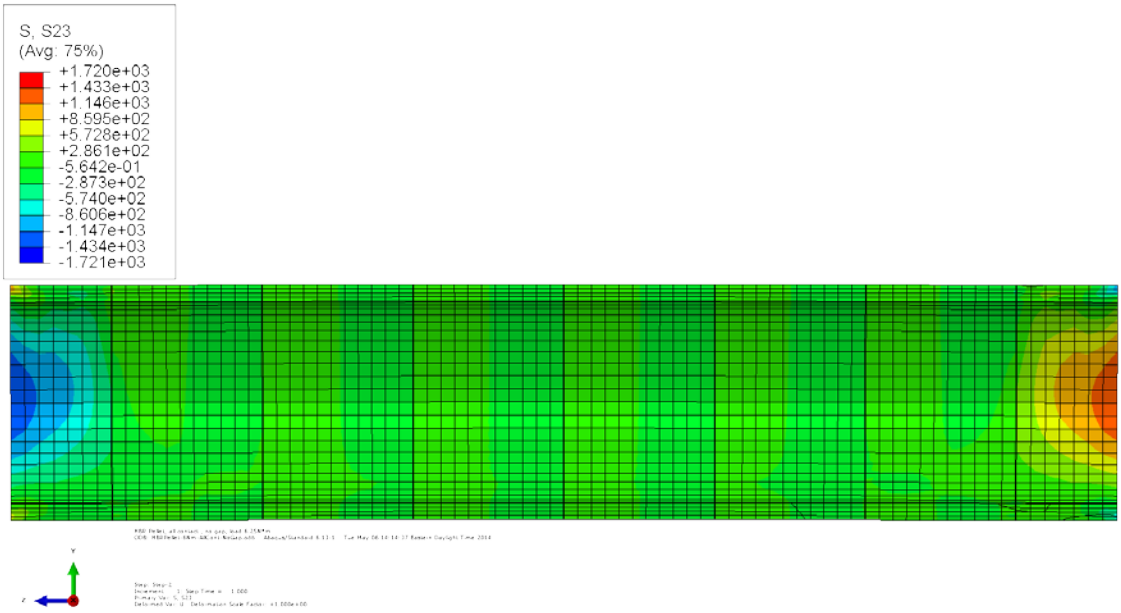

(c) Shear stress σ_{yz}

Figure 29. Shear stress distribution and curvature results for the clad-epoxy-pellet section model of HBR pellets without gaps at debonded pellet-pellet interfaces, and with an epoxy layer at debonded pellet-clad interfaces.

2.3.2.2 Interfacial Material at 10 × Young's Modulus

The fourth simulation is similar to the third one (shown in Figure 27), except the thin layer at the pellet-clad interface used an interfacial material with a Young's modulus 10 times that of epoxy. Based on the normal stress results shown Figure 30, the change in properties in the interface material had little impact on the bending response due to interfacial debonding. The results are close to those seen in Figure 28. There is no significant difference between the shear stress results shown in Figure 31 and those shown in Figure 29.

The evaluated curvature and flexural rigidity results for the cases of debonding at pellet-clad and pellet-pellet interfaces are listed in Table 4. Generally, all interfacial debonding resulted in larger induced curvatures and smaller estimated flexural rigidities. Compared with the perfect bond case results in Table 2 for the all interfacial debonding cases with gaps, flexural rigidity was reduced by up to 66%. Compared with the results for debonded pellet-pellet interfaces listed in Table 3, flexural rigidity dropped (1) by 26–43% compared with the cases of pellets with gaps, depending on the interfacial material, and (2) by 19–31% compared with pellets without gaps. These results further validate the earlier hypothesis that interfacial bonding efficiency can significantly affect the flexural rigidity of the surrogate composite rod. However, the impact of the property change in the interfacial material is small enough to be ignored in these four cases because the interface layer cannot provide direct internal support to resist the bending moment due to interfacial debonding.

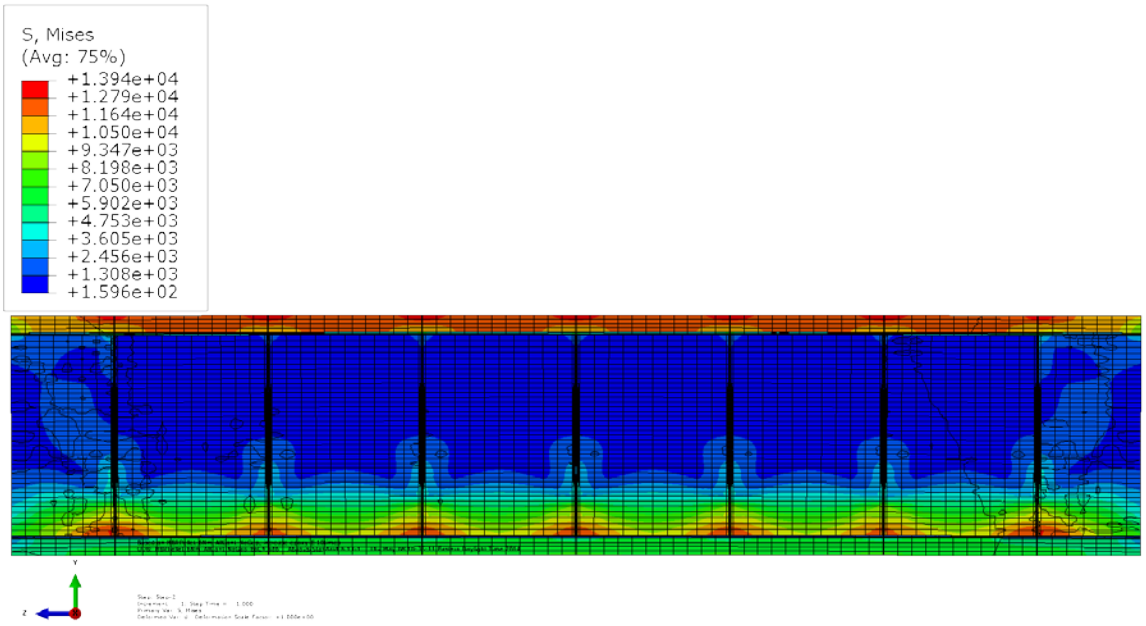

(a) Longitudinal section view of curvature and von Mises stress results

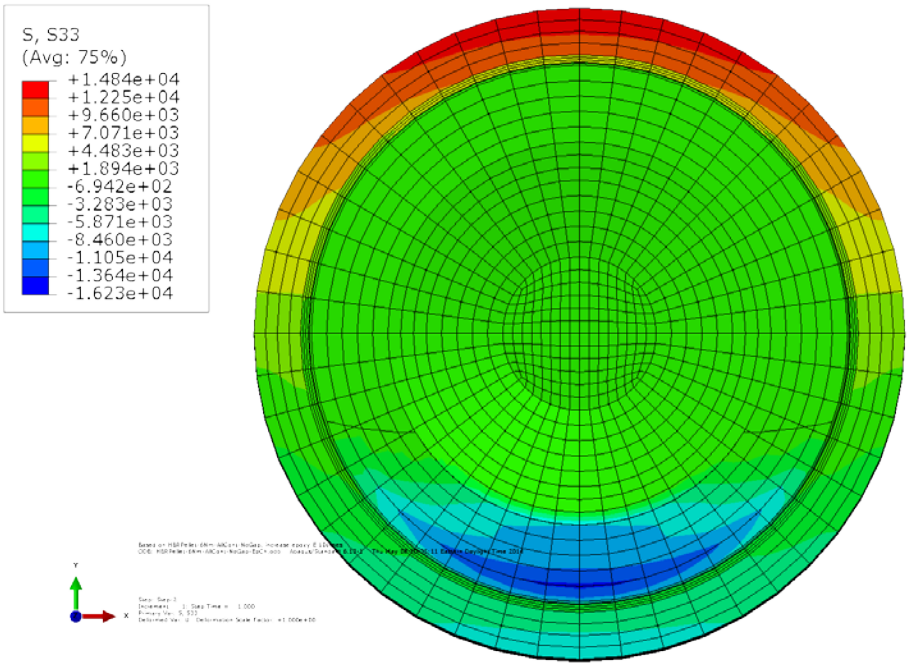

(b) Cross section view of normal stress, $\sigma_{zz,}$ results at a pellet-pellet interface

Figure 30. Normal stress distribution and curvature results for the clad-epoxy-pellet section model of HBR pellets without gaps at debonded pellet-pellet interfaces, and with a layer of 10 × Young's modulus material at debonded pellet-clad interfaces.

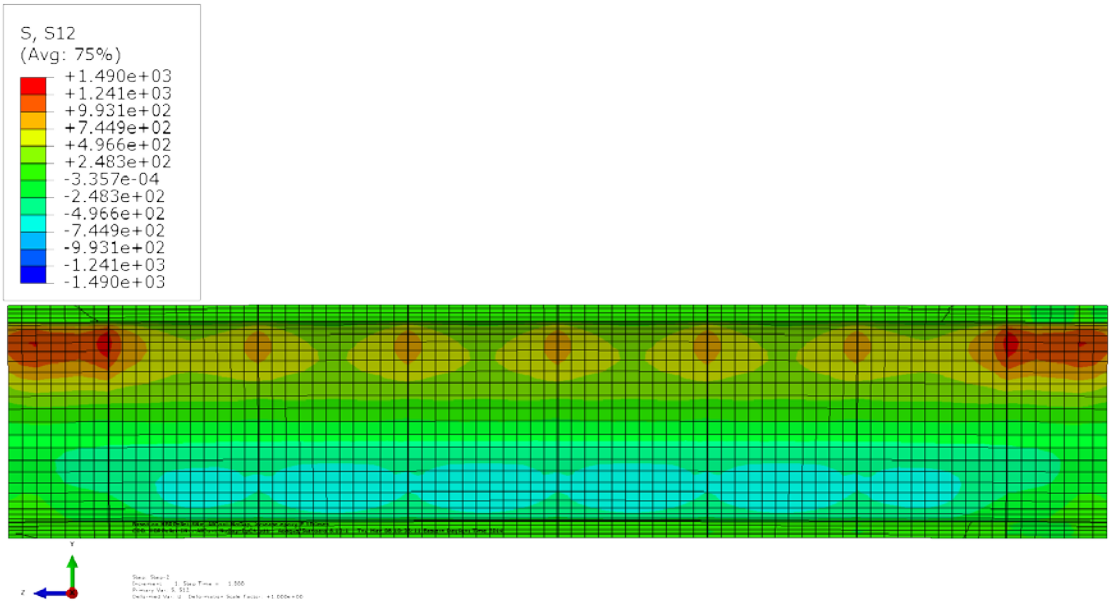

(a) Shear stress σ_{xy}

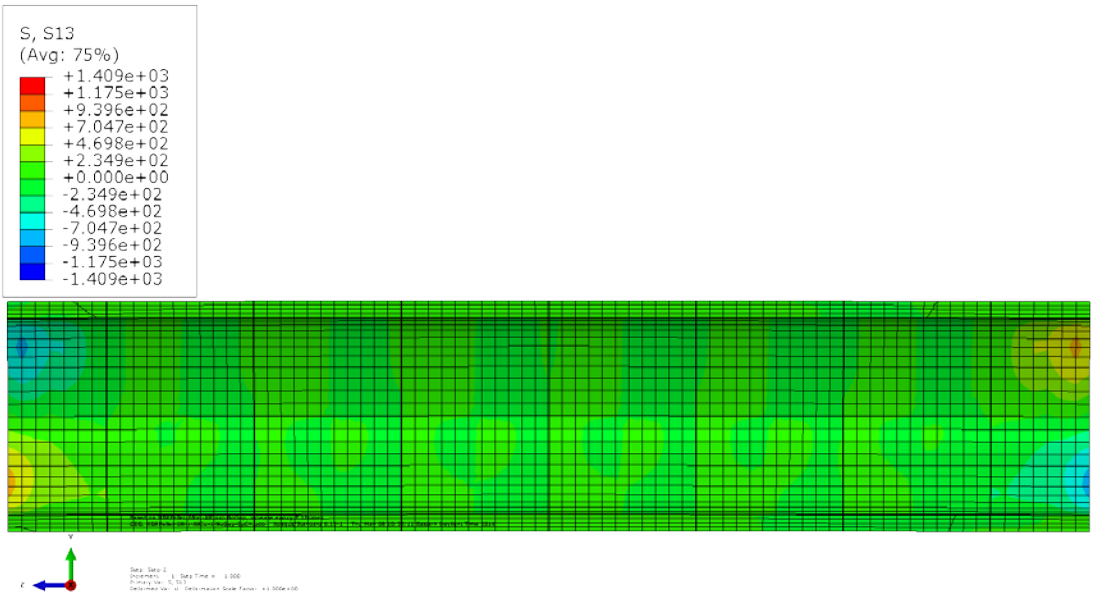

(b) Shear stress σ_{xz}

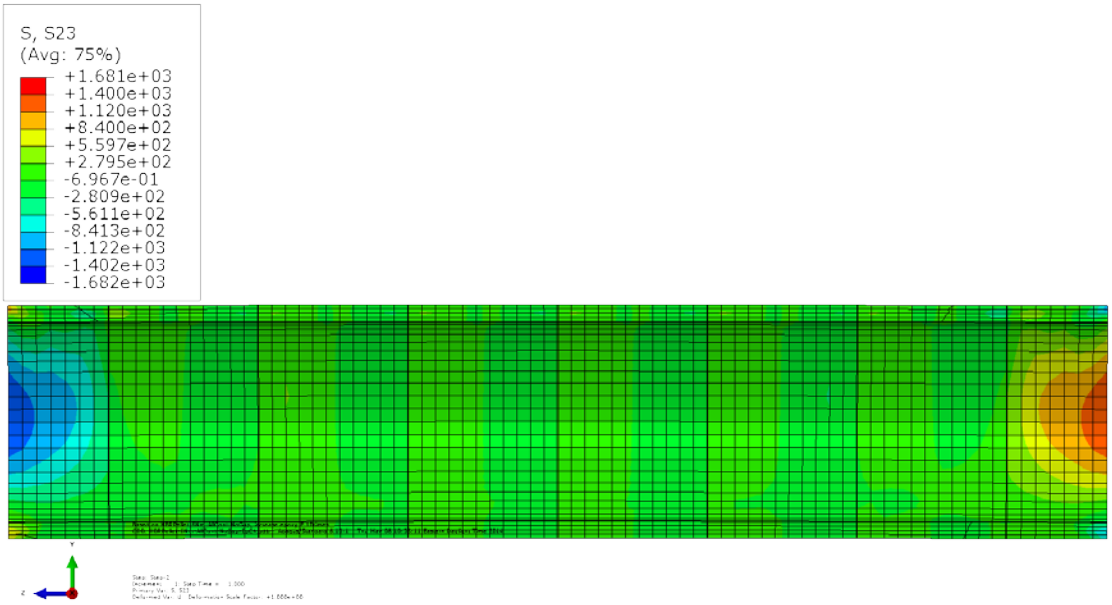

(c) Shear stress σ_{yz}

Figure 31. Normal stress distribution and curvature of clad-epoxy-pellet section model of HBR pellets without gaps at debonded pellet-pellet interfaces, and with a layer of 10 × Young's modulus material at debonded pellet-clad interfaces.

Table 4. The curvature, flexural rigidity and bending moment comparison for debonded pellet-clad and pellet-pellet interfaces

	Curvature κ(1/m)	Flexural rigidity EI (N·m^2)	Clad bending moment M (N·m)	Pellet bending moment M (N·m)
Pellet-pellet interface with gap debonded; pellet-clad interface debonded with epoxy	0.218	29	6.23	0.02
Pellet-pellet interface with gap debonded; pellet-clad interface debonded with 10 × Young's modulus material	0.202	30	5.96	0.29
Pellet-pellet interface without gap debonded; pellet-clad interface debonded with epoxy	0.146	43	4.15	2.10
Pellet-pellet interface without gap debonded; pellet-clad interface debonded with 10 × Young's modulus material	0.140	45	3.98	2.27

The gaps play an important role in flexural rigidity estimation. In Table 4, the flexural rigidity of the case without gaps at pellet-pellet interfaces is 1.5 times of that of the case with gaps. In Table 3, the ratio of the flexural rigidity is 1.2 for the same comparison. The reason for the large increase in flexural rigidity is the direct pellet contact at the pellet-pellet interfaces at the compression side. The direct pellet-pellet contact

interaction also provides a significant increase in bending moment resistance; it results in a much smaller curvature deformation, as shown in Table 4.

Table 4 shows that the bending moment significantly shifts from pellet to clad with all interface debonding, especially when there are gaps at pellet-pellet interfaces. When the pellets are in direct contact with one another, the pellets retake a large amount of the bending moment, which helps reduce the bending load on the clad.

2.4 Clad Curvature Estimation

The fuel rod bending curvature is derived from the clad deflection data. In CIRFT, there are three linear variable differential transformers (LVDTs) at two inch gauge sections of the fuel rod to measure three points of deflections on the clad outside wall (Figure 32).

The curvature κ can be defined by the radius of circle R. Three deflection data points at the clad outside wall can be used to determine the radius of circle R in Figure 33, as follows:

$$\begin{cases}(U_{1y}-y)^2+(U_{1z}-z)^2=(U_{2y}-y)^2+(U_{2z}-z)^2=R^2\\(U_{1y}-y)^2+(U_{1z}-z)^2=(U_{3y}-y)^2+(U_{3z}-z)^2=R^2\end{cases} \quad (2)$$

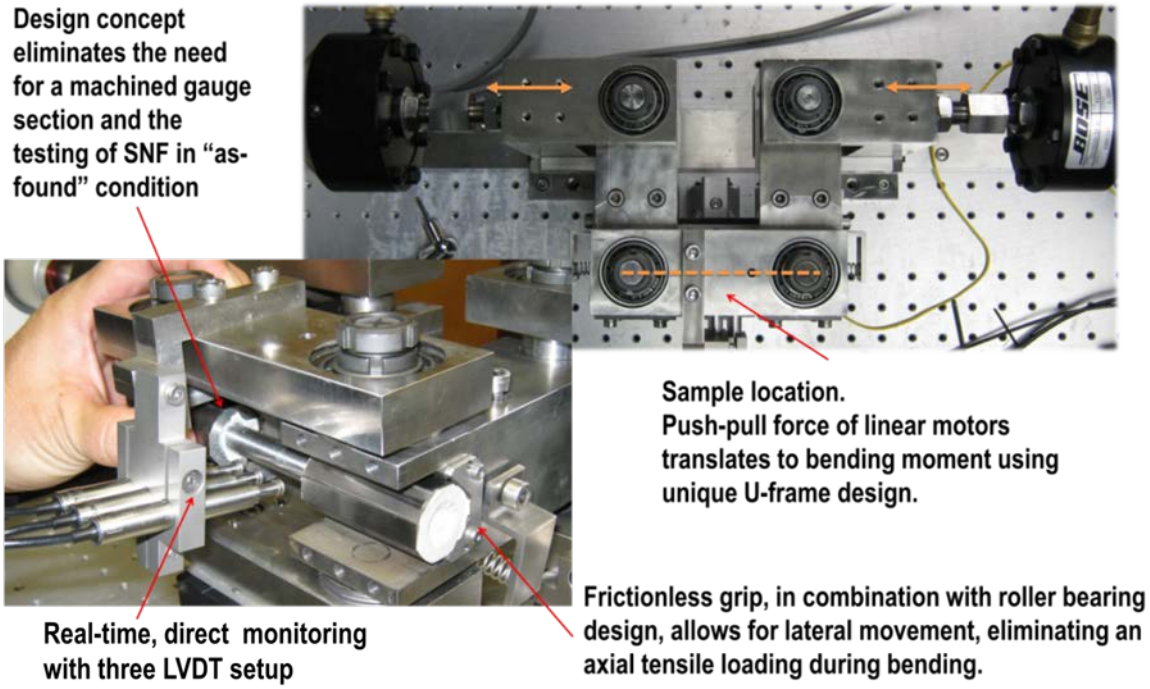

Figure 32. CIRFT system with horizontal U-frame test setup integrated to Bose dual LM2 TB.

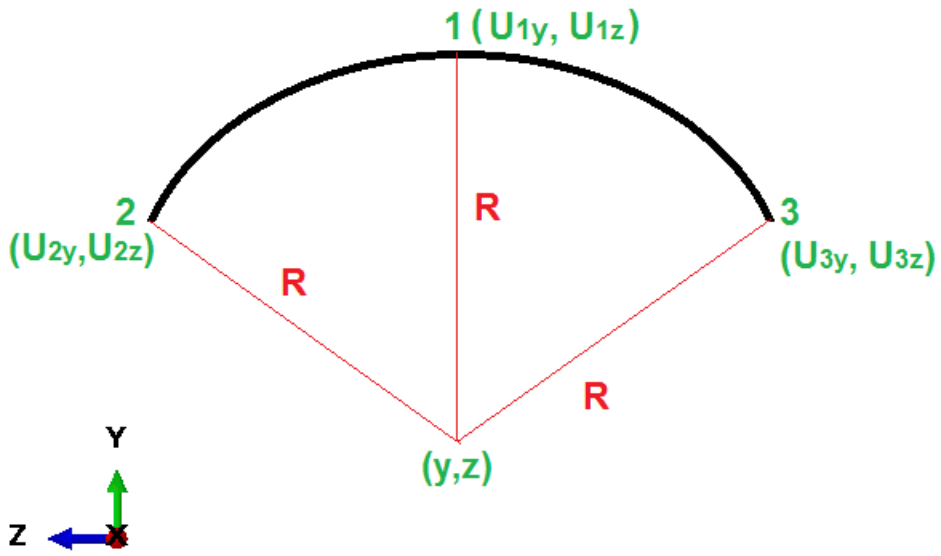

Figure 33. Sketch for curvature calculation.

Solving Eq. (2), the center coordinate of curvature (y, z) can be obtained as

$$\begin{cases} y = \frac{B2*C1-B1*C2}{B2*A1-B1*A2} \\ z = \frac{A2*C1-A1*C2}{A2*B1-A1*B2} \end{cases} \quad (3)$$

$$Where \begin{cases} A1 = 2*U_{2y} - 2*U_{1y} \\ A1 = 2*U_{3y} - 2*U_{1y} \\ B1 = 2*U_{2z} - 2*U_{1z} \\ B2 = 2*U_{3z} - 2*U_{1z} \\ C1 = U_{2y}^2 + U_{2z}^2 - U_{1y}^2 - U_{1z}^2 \\ C2 = U_{3y}^2 + U_{3z}^2 - U_{1y}^2 - U_{1z}^2 \end{cases}$$

So the radius of circle R is

$$R = \sqrt{(U_{1y} - y)^2 + (U_{1z} - z)^2} = \sqrt{(U_{2y} - y)^2 + (U_{2z} - z)^2} = \sqrt{(U_{1y} - y)^2 + (U_{2z} - z)^2} \quad (4)$$

The curvature κ can be determined as

$$\kappa = \frac{1}{R} \quad (5)$$

The following sections discuss the investigation of the curvature estimation using the clad deflection data. The global two inch gauge section and the localized area where the testing probe cannot focus are analyzed to determine how they are different.

2.4.1 Epoxy Used as Interfacial Material

In this section, the cases of (1) pellet-pellet interfacial debonding without gaps and (2) pellet-clad interfaces with good bonding are used as examples to study curvature estimation. In the first study category, the interface material at the pellet-clad interfaces uses epoxy. As seen in Figure 34, the normal stress σ_{zz} result for this simulation is distributed nonuniformly in the two inch gauge section. As discussed in the previous section, at pellet-pellet interface debonded regions, the clad takes most of the bending moment, which results in stress concentration. The maximum stress in these regions is 14.7 ksi. At the middle of the pellet-clad bond region, the clad has relatively less stress, with an average level of 9.1 ksi. There is significant deviation in stress distribution.

Therefore, two sets of deflection data were chosen to estimate curvature: one from the two inch gauge section, referred to as "global data," and the other from a finite localized area, referred to as "local data." The first two sets of induced deflection data were selected from the tension side of the clad under bending deformation in Figure 34. One set of the deformed coordinates (U_{1y}, U_{1z}), (U_{2y}, U_{2z}) and (U_{3y}, U_{3z}) from three points at the outside wall of the clad in the global two inch section range were output to calculate the curvature by following Eqs. (2)(5). The estimated curvature and resultant flexural rigidity are listed in Table 5 for comparison. The other set of data for curvature estimation were selected from the localized area, the detail area shown in Figure 34. This localized area is at the pellet-pellet interface debonded region. The three points are located at a finite distance, where the LVDT cannot be focused in the testing. These three deformed coordinates were output to estimate curvature and flexural rigidity.

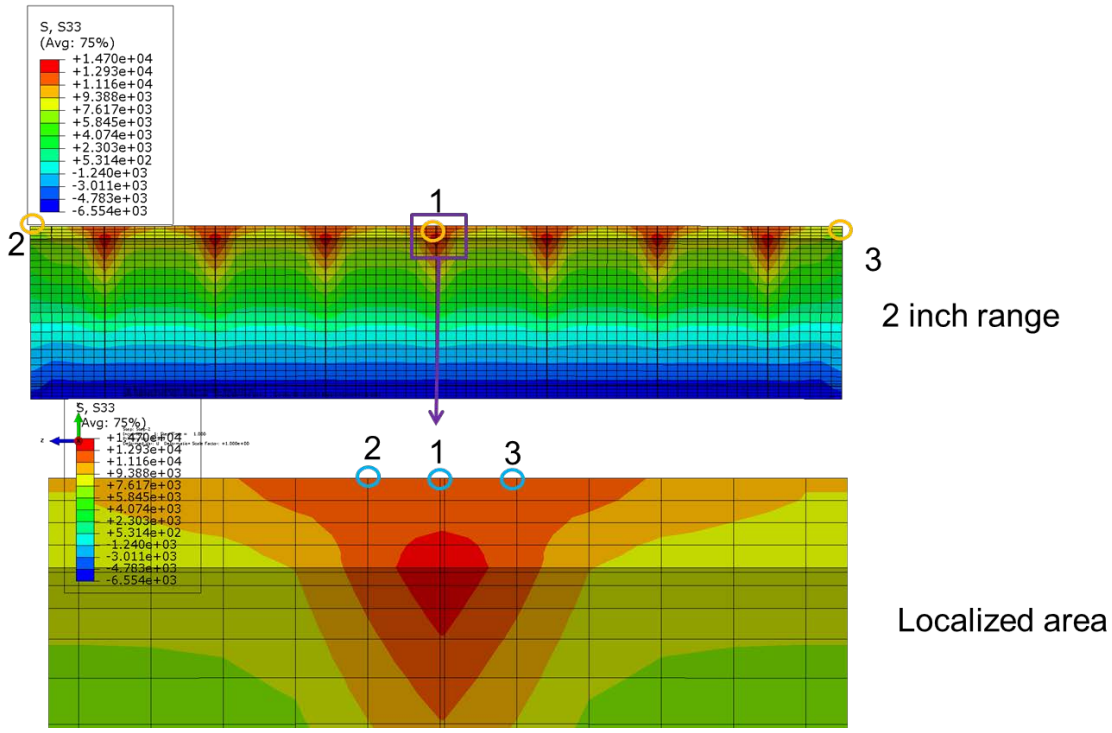

Figure 34. Curvature estimations from the deflection data at the tension side of the clad for case using epoxy as the interfacial material.

The summarized results in Table 5 show a large difference in curvature estimation and associated flexural rigidity when the three deflection data points are chosen from the relatively global and local areas. The data from the two inch range results in a curvature only ⅓ of that in the localized area at the pellet-pellet interface debonded region. The result is due to a lack of pellet support at the debonded interfaces. Therefore, the flexural rigidity estimated from local tensile clad deflection data is ~3 times that estimated

from the global data. When the study cannot be completed by testing because of instrumentation limitations, it is important to depend on the FEA simulation to investigate fuel rod behavior in detail, as shown in this example.

Table 5. Estimated curvature and flexural rigidity comparison from the tension side of the clad for case using epoxy as the interfacial material

	Curvature κ (1/m)	Flexural rigidity *EI* (N·m^2)
Two inch range	0.118	52.825
Localized area	0.388	16.113

The previous discussion established that for debonded pellet-pellet interfaces and bonded pellet-clad interfaces, pellet-pellet direct pinning at the compression side helps significantly lower the stress at the compression side of the clad. Following the same approach, two sets of deflection data were drawn from the compression side of the clad to estimate curvature in the two inch range, as well as from the localized area, as shown in Figure 35.

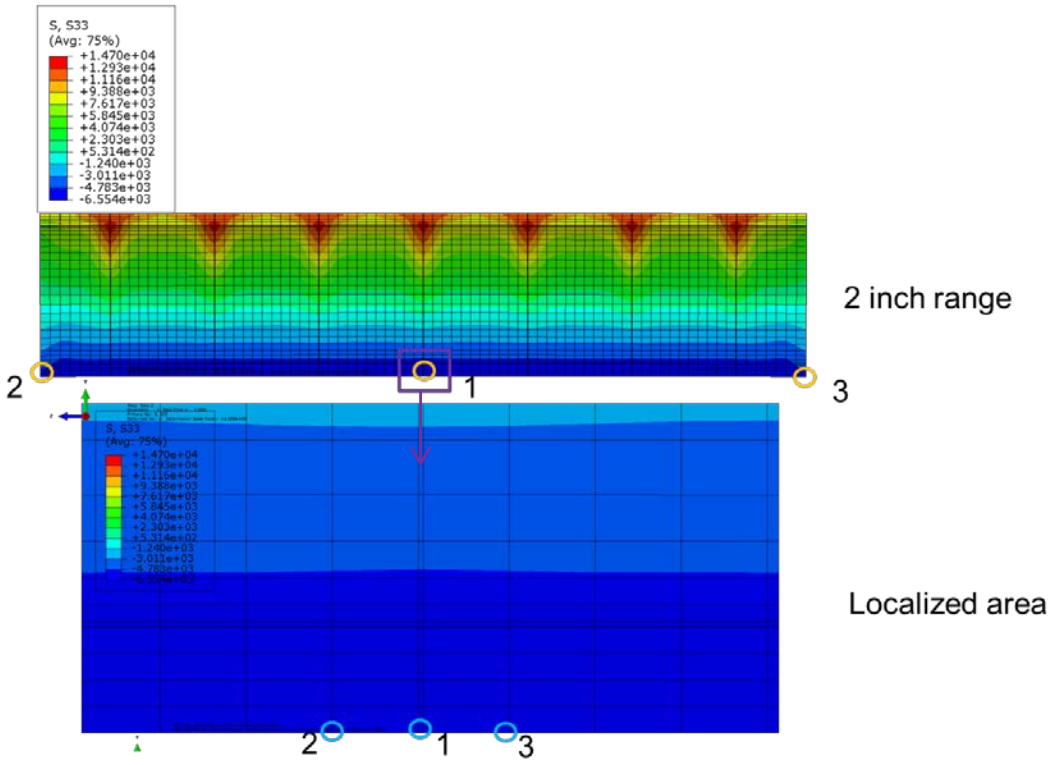

Figure 35. Curvature estimations from the deflection data at the compression side of the clad for the case using epoxy as the interface material.

The estimated curvature and flexural rigidity estimated from the deflection data at the compression side of the clad are compared in Table 6. The curvature estimated locally is still 39% higher than the curvature estimated globally, which results in a 39% reduction in flexural rigidity. Compared with the estimation at

the tension side in Table 5, the curvature and flexural rigidity estimated from deflection data in the global two inch gauge section range are the same. That is because globally, the nonuniform stress distribution averages out, although the curvature estimated in the localized area from the compression side is only half that estimated from the tension side. With pellet-pellet debonding at the clad compressive stress region, pellet-pellet pining still provides support for resisting flexural deformation. Therefore, locally the flexural rigidity on the compression side is double that on the tension side.

Table 6. Estimated curvature and flexural rigidity comparison from the compression side of the clad for the case using epoxy as the interface material

	Curvature κ (1/m)	Flexural rigidity *EI* (N·m^2)
2 inch range	0.119	52.482
Localized area	0.195	32.077

2.4.2 Interfacial Material with a 10 × Young's Modulus

The second study is also based on debonded pellet-pellet interfaces and well-bonded pellet-clad interfaces, but the interfacial layer is simulated as a 10 × Young's modulus material to evaluate how a change in the properties of the interfacial material would impact the estimation of curvature and flexural rigidity.

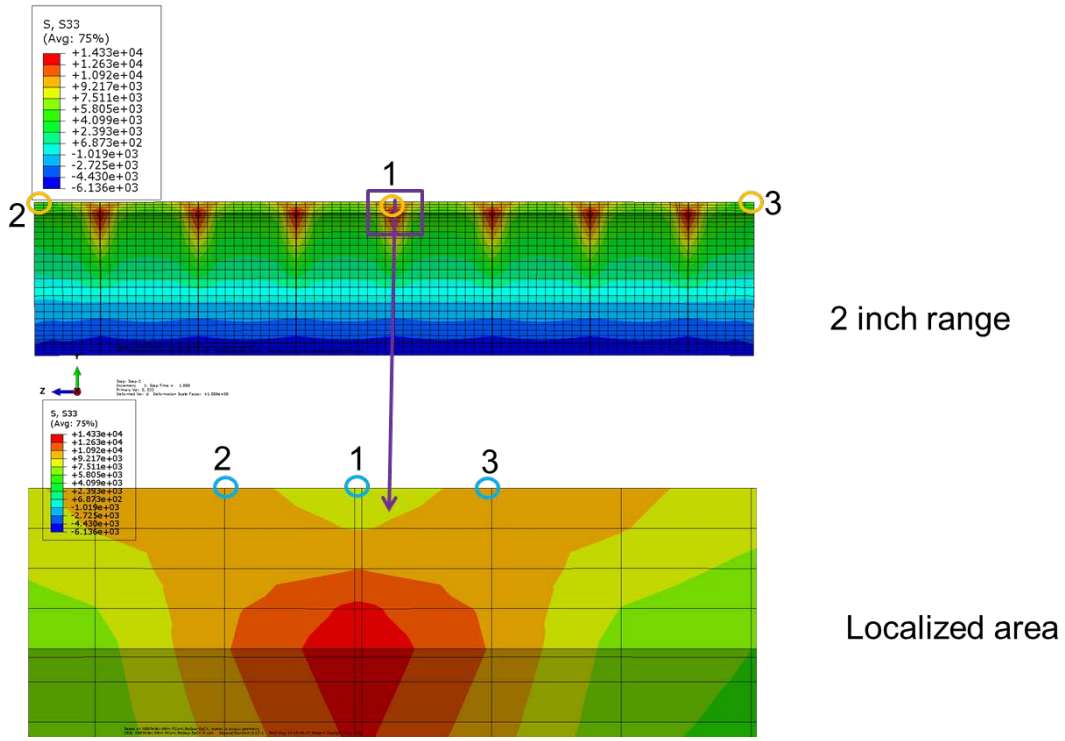

Figure 36. Curvature estimations from the deflection data at the tension side of the clad for the case using the 10 × Young's modulus material.

The same procedure was followed that is outlined in Section 2.4.1. The first clad curvature estimation data were from the tension side (Figure 36). The stress distribution was still nonuniform. Table 7 shows the globally and locally estimated curvature and flexural rigidity as the interface material becomes stiffer. As a result of a lack of pellet support at the debonded interface, the local tensile clad curvature is ~4 times that of the global curvature. There is a larger difference between the results estimated from global and local deflection data. In the localized area, the curvature and flexural rigidity are close to the estimations in Table 5 for the case using epoxy as the interface material. The larger difference results mainly from the estimations in the global two inch range. There is a 20% increase in flexural rigidity because of the 10 × increase in the Young's modulus of the interfacial material. This result indicates that the interfacial material will have more impact in estimations of curvature and flexural rigidity globally than locally at the tension side of the clad.

Table 7. Estimated curvature and flexural rigidity comparison from the tension side of the clad for the interface material with a 10 × Young's modulus

	Curvature κ (1/m)	Flexural rigidity *EI* (N·m^2)
Two inch range	0.096	65.373
Localized area	0.369	16.949

The deflection data for the interface material with a 10 × Young's modulus are also drawn from the compression side of the clad (see Figure 37). The estimated curvature and flexural rigidity are compared in Table 8.

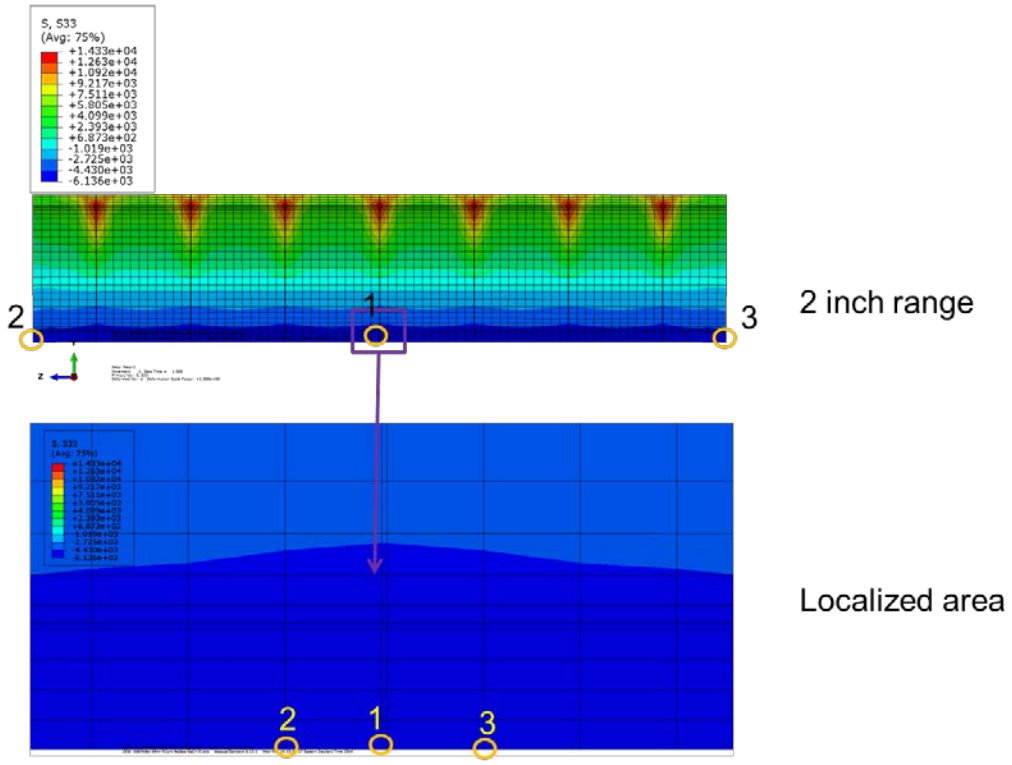

Figure 37. Curvature estimations from the deflection data at the compression side of the clad for the 10 × Young's modulus material.

Table 8. Estimated curvature and flexural rigidity comparison from the compression side of the clad for the interface material with a 10 × Young's modulus

	Curvature κ (1/m)	Flexural rigidity *EI* (N·m^2)
Two inch range	0.097	64.687
Localized area	0.130	48.098

2.5 Clad Stress Investigation and Comparison

Since the stress distribution on the clad is nonuniform, clad stress was investigated in further detail to obtain a better understanding of the clad stress profile. In this study, epoxy was simulated as the interface material.

2.5.1 Clad Stress Estimation from Conventional Approach Based on Curvature and Flexural Strain

In Section 2.4, the clad curvature was estimated from clad deflection data. The clad stress can be further estimated using a conventional approach based on curvature and flexural strain and then compared with the stress profile obtained from FEA. Figure 38 illustrates the flexural strain evaluation of a uniform rod. After flexural deformation, the length of the neutral surface remained the same. At the other sections, the flexural strain can be evaluated as follows:

$$\varepsilon=\kappa*y \tag{6}$$

Where
κ = curvature
y = distance from section surface to the rod neutral axis

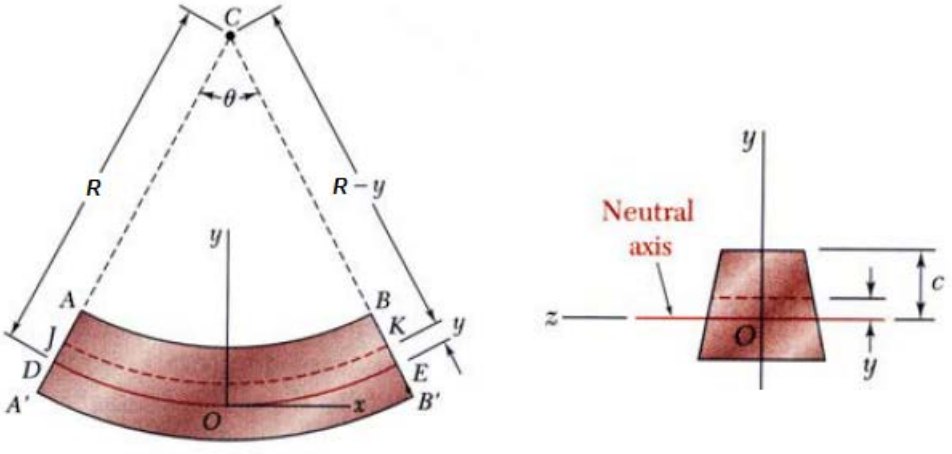

Figure 38. Flexural strain evaluation of a uniform rod.

For a single uniform rod, the neutral axis can be determined by section geometry and cannot change because it is based on geometric properties. However, for a composite fuel rod, the neutral axis will change because of the interface bonding condition and the shift in load-carrying capacity between the fuel pellets and the clad under flexural deformation, as shown in Figure 39 and Figure 40. In Figure 39, for the

perfect interface bonding, the fuel pellets and the clad tie together to resist the bending moment, and the system responds symmetrically. Therefore, the neutral axis of the composite rod resides at the geometric center line. For the pellet-pellet interface that is debonding, as shown in Figure 40, the normal stress results show an apparent shift of the composite system neutral axis from the geometric center line. Based on the bending moment balance calculation, the composite system neutral axis shift Δ can be determined as follows:

$$F_{tension}=\Sigma A_i*\sigma_{zz} \quad (7)$$

$$y_0=\Sigma A_i*\sigma_{zz}\ *y_i / F_{tension} \quad (8)$$

$$D=M / F_{tension} \quad (9)$$

$$\Delta=y_0-D/2 \quad (10)$$

where

σ_{zz} = Resultant normal stress, S33 in Figure 40

A = Element area

y_i = Distance of individual force calculated from normal stress to geometry center

M = Bending load 6.25N*m

y_0 = Distance from tension force center to geometric center

D = Bending moment arm length

Δ = Composite system neutral axis shift

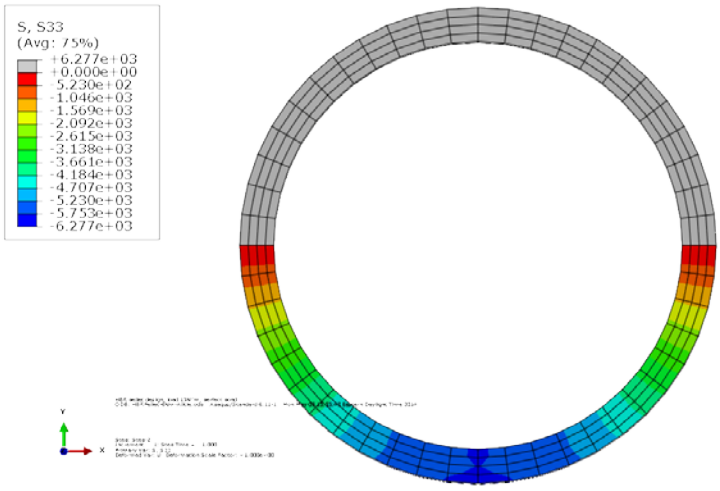

Figure 39. Clad neutral axis at geometric center line for perfect interface bonding.

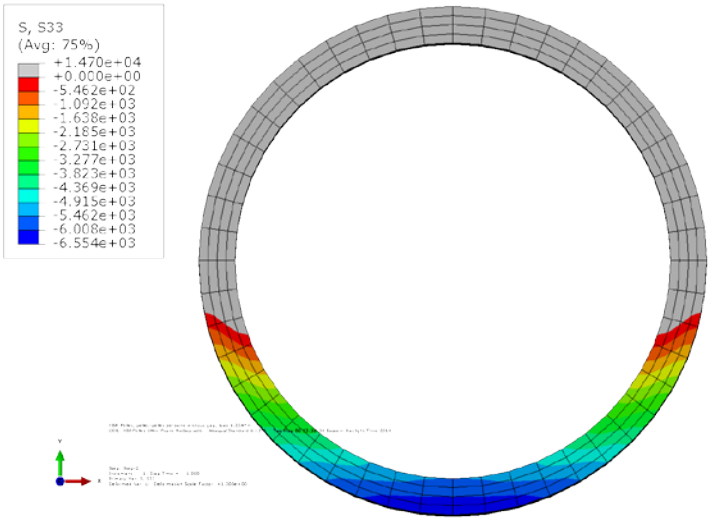

Figure 40. Clad neutral axis shifts from geometric center line for pellet-pellet interface debond and pellet-clad interface bond case.

Therefore, in the pellet-pellet debonding and pellet-clad bonded case, the fuel rod system neutral axis shifts down 0.039 inch from the geometric center based on the calculation. Applying Eq. (6), the flexural strain of the clad's outer surface can be estimated from the curvature data discussed in Section 2.4. For the perfect interface bonding, the distance from the clad's outer surface to the composite neutral axis *y* is the clad radius, because the neutral axis lies at the geometric center line. For the pellet-pellet interface debonding case, *y* is the clad radius adjusted by the neutral axis shift of 0.039 inch. The normal stress of the clad can be further estimated from the strain and Young's modulus, as follows:

$$\sigma_{zz}=\varepsilon*E \tag{11}$$

The Young's modulus of the Zr-4 clad material is shown in Table 1. Table 9 summarizes the estimated curvature, strain, and stress for the two cases discussed in this section. The estimated stress lies right between the FEA stress result at the pellet-pellet interface and the stress not at the pellet-pellet interface. So the stress estimation–based induced curvature and estimated flexural strain shows fairly reasonable results. It can be considered as the average value of the nonuniform stress distribution.

Table 9. Estimated normal stress compared with FEA stress profile

	EI ($N\cdot m^2$)	**κ (1/m)**	**Estimated ε (m)**	**Estimated σ_{zz} (psi)**	**FEA at pellet-pellet interface σ_{zz} (psi)**	**FEA not at pellet-pellet interface σ_{zz} (psi)**
Perfect bond	77	0.082	0.443E–3	5.842E+03	5.848E+3	5.686E+3
Pellet-pellet debond; pellet-clad bond	53	0.118	0.754E–3	9.950E+03	1.154E+4 (interior max stress 1.47E+4)	9.371E+3

2.5.2 Clad Stress Comparison between Different Interface Bonding Conditions

The FEA nonuniform normal stress and shear stress results for different interface bonding conditions with epoxy as the interface material are summarized in Table 10–Table 13 and are compared case by case at the tension side and the compression side of the clad. Table 10 shows the clad's normal stress at the tension side. Because of nonuniform stress distribution, the normal stress at the pellet-pellet interface region and the stress for locations other than the pellet-pellet interface region are compared for several interface bonding conditions: perfect bonding, only pellet-pellet interface debonding, both pellet-pellet and pellet-clad interface debonding, and pellet-pellet interface with and without gaps.

Generally, at the tension side, the axial stress σ_{zz} is much higher than the lateral stress σ_{xx} and σ_{yy} as a result of bending. For the perfect bonding case, σ_{zz} is slightly different at the pellet-pellet interface region and for locations not at the pellet-pellet interface regions. With pellet-pellet interface debonding, the σ_{zz} is almost double that in the perfect bond case because of the significant bending moment shift from pellet to clad at the pellet-pellet interface region. At the pellet-pellet interface region, stress concentrations are higher than those not at the pellet-pellet interface region. Without gaps at the pellet-pellet interfaces, the levels of σ_{zz} are reduced because the pellets take a big portion of the bending load via pinning. With further debonding at the pellet-clad interfaces, the resulting axial stress σ_{zz} appears more uniform at the pellet-pellet interfaces and for regions other than the pellet-pellet interfaces. However, the lateral stress σ_{xx} and σ_{yy} vary at different locations of the clad. The levels of σ_{xx} and σ_{yy} at the pellet-pellet interface region are all higher than those not at the pellet-pellet interface region.

Table 10. Clad normal stress comparison at tension side for different interface bonding conditions

Tension side	At pellet-pellet interface region			Not at pellet-pellet interface region		
	σ_{xx} (psi)	σ_{yy} (psi)	σ_{zz} (psi)	σ_{xx} (psi)	σ_{yy} (psi)	σ_{zz} (psi)
Perfectly bonded	239.0	66.8	5.76E3	260.4	–5.2	5.37E3
Debonded pellet–pellet interfaces with gaps	2.05E3	381.1	1.33E4	1.18E3	10.2	9.63E3
Debonded pellet–pellet and pellet–clad interfaces with gaps	749.1	–190.9	1.46E4	46.8	2.5	1.46E4
Debonded pellet–pellet interfaces without gaps	1.96E3	435.0	1.25E4	1.37E3	–8.36	9.08E3
Debonded pellet–pellet and pellet–clad interfaces without gaps	1.60E3	–247.1	1.32E4	581.5	–18.4	1.32E4

At the compression side, as shown in Table 11, the normal stress results are similar to those at the tension side, except that the stresses are mostly for compression instead of tension. Especially for the perfectly bonded and debonded pellet-pellet interfaces with gaps, because of the symmetrical stress distribution, the stress levels are the same. The big stress level difference is evident in cases without gaps at the pellet-

pellet interfaces. Because pellet pinching occurs at the compression side, the stress levels of σ_{zz} at the compression side are less than half those for the cases with gaps.

Table 11. Clad normal stress comparison at compression side for different interface bonding conditions

Compression side	At pellet-pellet interface region			Not at pellet-pellet interface region		
	σ_{xx} (psi)	σ_{yy} (psi)	σ_{zz} (psi)	σ_{xx} (psi)	σ_{yy} (psi)	σ_{zz} (psi)
Perfectly bonded	–239.0	–66.8	–5.76E3	–260.4	5.2	–5.37E3
Debonded pellet–pellet interfaces with gaps	–2.05E3	–381.1	–1.33E4	–1.18E3	–10.2	–9.63E3
Debonded pellet–pellet and pellet–clad interfaces with gaps	51.8	1.4	–1.47E4	561.7	–90.9	–1.47E4
Debonded pellet–pellet interfaces without gaps	–171.0	14.1	–6.0E3	–9.58	–9.97	–5.8E3
Debonded pellet–pellet and pellet–clad interfaces without gaps	747.5	–24.3	–6.22E3	1.15E3	–96.2	–6.24E3

Similar to the normal stress, the shear stress results at the tension side and at the compression side are compared in Table 12 and Table 13. In general, σ_{yz} dominates σ_{xy} and σ_{xz} by several orders of magnitude. The σ_{xy} and σ_{xz} are small enough to be ignored, so σ_{yz} was the focus for the comparison. At the tension side, for perfect bonding, the clad transfers less shear stress than for the other bonding conditions. As a result of the symmetrical stress distribution for perfectly bonded and debonded pellet-pellet interfaces with gaps, the shear stress σ_{yz} results at the tension side are the same as those at the compression side. At the compression side, the σ_{yz} for the case without gaps at the pellet-pellet interfaces is much smaller than that at the tension side. The reason might be the same as that discussed for the normal stress comparison: pinching by pellets.

Table 12. Clad shear stress comparison at tension side for different interface bonding conditions.

Shear stress from clad Node No. 810 at pellet-pellet interface region, tension side	σ_{xy} (psi)	σ_{xz} (psi)	σ_{yz} (psi)
Perfectly bonded	–1.08E-03	2.40E-04	–22.01
Debonded pellet–pellet interfaces with gaps	–2.72E-04	2.96E-05	–95.13
Debonded pellet–pellet and pellet–clad interfaces with gaps	–2.10E-05	–2.43E-03	57.78
Debonded pellet–pellet interfaces without gaps	5.15E-05	–3.46E-04	–121.56
Debonded pellet–pellet and pellet–clad interfaces without gaps	2.19E-05	–9.44E-05	59.67

Table 13. Clad shear stress comparison at compression side for different interface bonding conditions

Shear stress from clad node no. 816 at pellet-pellet interface region, compression side	σ_{xy} (psi)	σ_{xz} (psi)	σ_{yz} (psi)
Perfectly bonded	–3.91E-04	3.31E-04	–22.01
Debonded pellet–pellet interfaces with gaps	–3.63E-05	–3.25E-05	–95.13
Debonded pellet–pellet and pellet–clad interfaces with gaps	–1.27E-05	–2.21E-03	2.73
Debonded pellet–pellet interfaces without gaps	8.43E-04	–3.00E-04	5.04
Debonded pellet–pellet and pellet–clad interfaces without gaps	–1.34E-04	2.37E-04	13.25

3. CONCLUSION

Based on FEA simulation results and further verification from high burnup HBR rod bending test results, the localized system (stress-curvature) biases and uncertainties associated with CIRFT global response on the SNF rod system performance can be quantified and summarized as discussed below.

First, with good interface bonding and without fuel pellet and clad fracturing, the pellets in the HBR rod will carry more bending moment resistance than the clad under normal transportation vibration. The maximum stress resides in the pellets, and the stresses at the clad and pellet are both below the yield condition; therefore, the system is in a linear elastic state under the target bending loads. When the Young's modulus of the interface material is increased to 10 times that of epoxy, the fuel rod system stiffness increases. There is no shear stress surge inside the Zr-4 cladding.

Upon fuel pellet failure, including debonding at the pellet-pellet interfaces, the load carrying capacity shifts from the fuel pellets to the clad. The clad starts to carry most of the bending moment at the pellet-pellet interface region, resulting in localized stress concentrations in the clad. However, under the target bending moment, the clad does not yield. With good cohesion bonding at the pellet-clad interfaces, the pellets can continue to support the clad and carry a sufficient portion of the bending moment resistance; therefore, most of the clad at the gauge section remains in the linear elastic range. A shear stress surge occurs inside the cladding at the pellet-pellet interface regions. The flexural rigidity increases at $10 \times$ Young's modulus material, indicating that the stiffness of the HBR rod system increases.

When further debonding occurs at the pellet-clad interfaces, the embedded pellets can no longer provide effective structural support to the clad and assist load transfer within the HBR rod system. Thus most of the load-carrying capacity shifts to the clad throughout the entire gauge section. The shift leads to maximum stress concentrations in the clad in the entire gauge section instead of at localized pellet-pellet interface regions. For this case, the impact of the property change in the interface material is very limited. The clad does not yield because of the high material yield strength and the low bending load. There is no resulting shear stress concentration inside the clad for interface debonding.

When the pellets contact and pinch one another, they seem to take over a significant portion of the bending load resistance, especially where there are no gaps at the pellet-pellet interfaces. This pellet pinning action clearly mitigates and avoids stress concentration and potential yielding at the compression side of the clad.

All of the simulation cases are summarized in Table 14. The main parameter flexural rigidity *EI* is compared case by case. As the Young's modulus of the interface material increases to 10 times that of epoxy, the fuel rod system becomes stiffer. The flexural rigidity increases by up to 26% for the pellet-pellet interface debonding with gaps. When all the interfaces are debonding, the interface material has very limited impact on the flexural rigidity, an impact that is small enough to be ignored. The immediate consequence of interface debonding is a shift in the load-carrying capacity from the fuel to the clad, as well as a reduction in flexural rigidity. For example, the flexural rigidity is 77 $N \cdot m^2$ when the pellets are perfectly bonded with epoxy. In the case with gaps at the pellet-pellet interfaces, when there is debonding at the pellet-pellet interfaces alone, the flexural rigidity drops by 49% to 39 $N \cdot m^2$. In the case without gaps, it drops by 31%, to 53 $N \cdot m^2$. Further debonding at the pellet-clad interfaces causes the flexural rigidity to drop further, by 26% and 19%, respectively, for the cases with gaps and without gaps. Overall, for cases with gaps and without gaps, flexural rigidity drops by about 62% and 44%, respectively, between the perfect bond and the debond cases at all interfaces. The changes in flexural rigidity are similar for different bonding conditions for the two types of interfacial material.

Flexural rigidity is reduced more by debonding at pellet-pellet interfaces than by debonding at pellet-clad interfaces. Table 5 shows a flexural rigidity that is about 30% higher for the fuel rod without gaps, indicating a significant increase in system stiffness over the case with gaps. Therefore, the gaps at the interfaces of the fuel rod system have a significant impact on system reliability, especially at pellet-pellet interfaces. The flexural rigidity and bending moment resistance capacity of the fuel rod are highly dependent on interface bonding efficiency at pellet-clad and pellet-pellet interfaces. This discovery was validated by ORNL reversal bending fatigue test results performed on the fuel rod with HBR pellet inserts.

The estimates for curvature and the associated flexural rigidity vary widely between three deflection data points chosen from a relatively global area and a local area. Because of a lack of pellet support at the debonded interface, the local tensile clad curvature is ~3 to 4 times that of the global curvature at the tension side of the clad. At the compression side of the clad, the curvature and flexural rigidity estimated from the deflection data in the global two inch gauge section range are the same. However, the curvature estimated in a localized area from the compression side is ~ ⅓ to ½ that estimated from the tension side. With pellet-pellet debonding at the clad's compressive stress region, pellet-pellet pinning continues to provide good support to resist flexural deformation. Locally, the flexural rigidity estimated from the local compression side is double or triple that estimated from the local tension side.

Table 14. The flexural rigidity comparison between the different bonding and debonding cases

Interface bonding conditions	Flexural rigidity *EI* ($N \cdot m^2$)	Increase from epoxy to stiffer interface material (%)	Reduction from perfect bond (%)	Reduction from only pellet-pellet debond to further pellet-clad debond (%)	Increase from with gaps to without gaps (%)
Perfect bond with epoxy	77				
Perfect bond with 10 × Young's modulus material	87	11			
Pellet-pellet interface with gap debond, pellet-clad interface bonded with epoxy	39		49		
Pellet-pellet interface with gap debond, pellet-clad interface bonded with 10 × Young's modulus material	53	26	39		
Pellet-pellet interface without gap debond, pellet-clad interface bonded with epoxy	53		31		26
Pellet-pellet interface without gap debond, pellet-clad interface bonded with 10 × Young's modulus material	65	18	25		18
Pellet-pellet interface with gap debond, pellet-clad interface debonded with epoxy	29		62	26	
Pellet-pellet interface with gap debond, pellet-clad interface debonded with 10 × Young's modulus material	30	3	66	43	
Pellet-pellet interface without gap debond, pellet-clad interface debonded with epoxy	43		44	19	33
Pellet-pellet interface without gap debond, pellet-clad interface debonded with 10 × Young's modulus material	45	4	48	31	33

The clad stress investigation reveals that the fuel rod system neutral axis shifts with interfacial debonding. The stress estimation based on induced curvature and flexural strain adjusted by the neutral axis shifting shows fairly reasonable results. The comparison between clad stress at the pellet-pellet interface region and away from the interface region shows a nonuniform stress distribution. The normal change in clad stress for different interface bonding conditions, especially a change in axial stress σ_{zz}, reveals a similar trend in the change in curvature. σ_{yz} dominates in the shear stress results. For the case without gaps at pellet-pellet interfaces, the σ_{yz} at the compression side is much smaller than that at the tension side as a result of pellet-pellet pinching.

4. REFERENCES

1. US Department of Energy, Used Fuel Disposition Campaign, *Used Nuclear Fuel Loading and Structural Performance Under Normal Conditions of Transport—Modeling, Simulation and Experimental Integration RD&D Plan*, FCRD-UFD-2013-000135, April 1, 2013.
2. B. Bevard, R. Howard, J.-A.J. Wang, Y. Yan, H. Wang, and H. Jiang, *FY 2014 Status Report: Vibration Testing of High Burnup Clad Fuel*, ORNL/LTR-2014/105, Oak Ridge National Laboratory, Oak Ridge, Tennessee, 2014.
3. J.-A.J. Wang, H. Jiang, and H. Wang, *Using Surrogate Rods to Investigate the Impact of Interface Bonding Efficiency on Spent Nuclear Fuel Vibration Integrity*, ORNL/LTR-2014/257, Oak Ridge National Laboratory, Oak Ridge, Tennessee, 2014.
4. H. Jiang, J. J. A. Wang, and H. Wang, "Potential Impact of Interfacial Bonding Efficiency on Used Nuclear Fuel Vibration Integrity during Normal Transportation," *Proceedings of the ASME 2014 Pressure Vessels and Piping Conference*, PVP2014-29117, Anaheim, California, July 2014.
5. J.-A.J. Wang, H. Wang, Y. Yan, R. Howard, and B. Bevard, *High Burn-up Spent Fuel Vibration Integrity Study Progress Letter Report (Out-of-Cell Fatigue Testing Development—Task 2.1)*, ORNL/TM-2010/288, Oak Ridge National Laboratory, Oak Ridge, Tennessee, 2011.
6. J.-A.J. Wang, H. Wang, T. Tan, H. Jiang, T. Cox, and Y. Yan, *Progress Letter Report on U-frame Test Setup and Bending Fatigue Test for Vibration Integrity Study (Out-of-Cell Fatigue Testing Development—Task 2.2)*, ORNL/TM-2011/531, Oak Ridge National Laboratory, Oak Ridge, Tennessee, 2012.
7. H. Wang, J.-A.J. Wang, T. Tan, H. Jiang, T. Cox, R. Howard, B. Bevard, and M. Flanagan,
8. "Development of U-Frame Bending System for Studying the Vibration Integrity of Spent Nuclear Fuel," *Journal of Nuclear Material* 440, 201–13, 2013.